NTNU

Norwegian University of
Science and Technology

THz time domain spectroscopy of materials in reflection and transmission

Kjell Martin Mølster

Master of Science in Electronics
Submission date: July 2017
Supervisor: Ulf Lennart Østerberg, IES

Norwegian University of Science and Technology
Department of Electronic Systems

My humble efforts are dedicated to,
the grandfather I met
Nils Vidar Rafael Björklund (1933-2011)
and didn't meet
Kjell Mølster (1938-1979).

Sammendrag

Denne oppgaven beskriver en rekke forbedringer til et tidsbasert terahertz spektroskopisystem. Systemet bruker plasma til å generere terahertz-bølger og elektrooptisk sampling i fritt rom til å detektere bølgene.

I oppgaven presenterer vi målinger av flere ulike materialer og sammenligner dem med eksisterende forskning, slik at vi utvedtydelig redegjør for nødvendigheten av generelle eksperimentelle betraktninger som f.eks luftfuktighet, små justeringer av optiske elementer, strålestørrelse, oppførsel rundt fokus og polering av prøver. Disse betraktningene er kritisk for nøyaktigheten av målingene av den komplekse refraksjonsindeksen $\hat{n} = n + i\kappa$. I tillegg demonstrerer vi at deteksjon ved bruk av elektrooptiske krystaller vesentlig begrenser potiensielle målinger.

Summary

This thesis presents and describes various improvements to a Terahertz time domain spectroscopy setup using plasma filament for generation and free space electro optic sampling for detection.

By performing measurements on several materials, and comparing them to the literature, we explicitly demonstrate that general experimental considerations, e.g. humidity, small misalignments, beam spot, behavior around the focal plane, and polishing of samples are detrimental for accurate measurements of the complex refractive index $\hat{n} = n + i\kappa$. We also demonstrate that an EO-crystal detection scheme substantially limits the measurements.

Preface

This master thesis was performed in the Ultrafast Optics laboratory at NTNU in the spring of 2017. I am very grateful for the time I got to spend in the lab. For the first time in several years at NTNU, it felt like somewhere I belonged. I owe a great deal to the people that have helped me through my thesis work.

First and foremost, a big and special thanks go to my supervisor, Prof.Ulf Lennart Österberg. I am grateful that he have used countless hours helping me with writing and discussing experimental results. His knowledge and enthusiasm for science have helped me at innumerous occasions. I find that he has been a true source of inspiration the last year, I have learned a great deal of things from him.

I would also like to thank Trygve Sørgård, for helping me with my thesis work writing and encouraging me in my moments of doubt. Working together in the laboratory has been a pleasure and very helpful. His cooperation have helped me to understand and solve many problems throughout the thesis work.

Also, I would like to thank; Prof.Ursula Gibson for letting me work in her lab and for lending me samples. Moreover, for sharing her vast knowledge by answering me several questions and teaching me about the CMKIII deposition system and the borrowed samples. Erik Lysne for being a source of inspiration. I will miss the discussions we have had over the last year. Reza Zamiri which guided me through the lab environment, and for helping me in the starting phase of the thesis work. Tore Landsem and Tore Berg at Teleteknisk Verksted for their extraordinary craftsmanship, startling problem-solving and brilliant eye for details.

A warm and grateful thanks to my beloved family, girlfriend, and cat that all have supported me through my thesis work.

Table of Contents

Sammendrag i

Summary i

Preface ii

Table of Contents v

List of Tables viii

List of Figures xiv

Abbreviations xv

Symbols xvii

1 Introduction 1

2 Theory 5
2.1 Basics of Electromagnetics 5
2.1.1 Polarization of materials 6
2.1.2 The wave equation 8
2.2 Ultrashort Chirped Pulses 10
2.3 Second harmonic generation (SHG) 12
2.4 Pockel's Effect in $\bar{4}3m$ Crystals 13
2.5 Generation of THz pulses 16
2.5.1 Photoconductive antenna 16
2.5.2 Optical recitification 17
2.5.3 Generation of THz in Air 18
2.6 Detection of THz by Free-space electro optic sampling (FSEOS) 19

3 Terahertz Time-Domain Spectroscopy **21**
3.1 Measurement principle . . . 22
3.2 Calculations of optical parameters . . . 22
3.2.1 Optically thick samples with small absorption . . . 23
3.2.2 Samples with Absorption . . . 26
3.2.3 Optically Thin samples (Fabry Perot) . . . 26
3.2.4 Reflection at 45-degrees s-polarized . . . 27

4 Experimental Methods **29**
4.1 Experimental Setup . . . 29
4.2 Resolution and Bandwidth . . . 36
4.3 Noise, Dynamic range and Signal-to-Noise Ratio . . . 38
4.4 Lock-in Amplifier . . . 39
4.5 Improvement to the experimental setup . . . 40
4.5.1 Practical Science . . . 40
4.5.2 Unexpected problems . . . 47
4.5.3 FSEOS - Fabry Perot effect . . . 58

5 Results **65**
5.1 Silicon . . . 66
5.1.1 HRFZ Silicon 4.46mm . . . 66
5.1.2 Silicon Polish . . . 69
5.1.3 Heavy doped n-type Si . . . 72
5.1.4 Fused Silica $1030.8\mu m$ (Fused Quartz) . . . 75
5.2 Germanium $1mm$ . . . 78
5.3 GaP $5mm$ . . . 80
5.4 KTP $KTiOPO_4$ $500\mu m$ . . . 83
5.5 Reflection Measurement . . . 87

6 Discussion **89**
6.1 Sources of error . . . 89
6.1.1 Thickness/Caliper . . . 89
6.1.2 Humiditiy . . . 93
6.1.3 Geometrical beam considerations . . . 93
6.1.4 Polishing . . . 95
6.1.5 Dispersive Samples . . . 95
6.1.6 Other sources . . . 96
6.2 Status of the setup . . . 98

7 Conclusion and Further Works **99**

Bibliography **101**

Appendices **107**

A Calculating optical parameters for reflection at 45-degree incidence for s-polarized waves **109**

B Calculations of optical parameters for transmission with complex fresnels coefficents **111**

C Numerical extraction of optical parameters **113**

D Material properties **115**
D.1 Germanium 115
D.2 Fused Silica 117
D.3 Silicon 118
D.4 GaP 119
D.5 $KTiOPO_4$ (KTP) 121

E Unwrapping and Extrapolation of phase and the impact on n and κ **123**

F Additional Theory **125**
F.1 Polarization of Electric fields 125
F.1.1 Jones Calculus 126
F.2 Fresnels equation and Fabry-Perot Etalon 126
F.2.1 Fabry-Perot Etalon 128
F.3 Gaussian Beam propagation 129

List of Tables

4.1 Configurations of the two flip mirrors, "On" refers to when the flip mirror is in raised position i.e. when it is reflecting the beam. Figure 4.1 shows flip mirror 1 in green and flip mirror 2 in purple. 29

4.2 Optical path length (OPL) from first beam splitter until hitting the electro-optic crystal for pump and probe beam. Measurements done while the translation stage was in equilibrium. 32

4.3 The size of the pinhole and the measured peak amplitude. The measurements were conducted with a relative humidity around 30% and sub-optimal alignment of the whole setup. 42

4.4 The size of the pinhole and the measured peak amplitude. The measurements were conducted with a relative humidity around 36% and sub-optimal alignment of the whole setup. 42

4.5 Recorded peak values for different angles of the EO-crystal. Recorded from the lock-in amplifier while positioned on the peak value. 44

4.6 The three recorded peak-to-peak values for, from the left, no polarizer, perpendicular oriented polarizer and horizontal oriented polarizer. 46

4.7 The time of each scan to the left, number of scans conducted with its respective time constant, calculated dynamic range and the relative humidity of the measurement. 48

4.8 Dynamic range and Room humidity at the top. The parameter X at the bottom calculated from equation (4.15) 49

4.9 The measured position of the retroreflector motor inside Solstice compressor stage for two measurements measurements conducted. The "R" and "L" is the total steps away or towards the grating inside the compressor stage, respectively 50

4.10 Information for thermal evaporation deposition of Cr on GaP. 59

4.11 Table showing in percentage the relative peak amplitude of the first Fabry-Perot reflection to the main pulse 60

5.1 The measured absorption at integer points of frequency. The ratio between the measured absorption coefficient and the frequency squared. 77

List of Figures

1.1 The THz band, the size of the THz band is exaggerated to emphasize which bands it lies in between, i.e. Far Infrared waves and microwaves. 1

2.1 Brief visualization of the generation of an ultra short laser pulse with active mode-locking. Exchanging the modulator with for example a saturable absorber will yield a passive mode-locking scheme. 10

2.2 A chirped pulse where the instantaneous frequency increase with time, from [52] 11

2.3 The index ellipsoid for an isotropic $n_x = n_y = n_x$, an uniaxial $n_x = n_y \neq n_z$ and a biaxial $n_x \neq n_y \neq n_z$ crystal . The principal axis are shown as z',y' and x'. Figure from [41]. 14

2.4 A DC-biased PC antenna. The semiconductor substrate is shown in yellow, metallic electrodes are connected to the DC bias, an optical pulse (red) is incident on the area between these electrodes and a THz pulse (blue) is generated. The length between the electrodes are given as W. 17

2.5 (a) Picture showing the experimental setup for generation of THz, utilizing a BBO crystal and a Lens. (b) Type-1 BBO crystal generation of second harmonic wave. Note that only a fraction of the fundamental wave have the same polarization as the SH-wave. Picture from [46] 19

2.6 Scheme for FSEOS, an optic sampling pulse and a pump THz pulse propagates collineraly towards an electro-optic medium, the outgoing pulse from the EO medium propagates through a compensator, typically a $\frac{\lambda}{4}$ waveplate. The wollaston prism (polarizing beam spltter) creates a decomposition of the pulse in y and x directions. These pulses are fed to two photo-diodes which are cross connected to an anode and cathode, resulting in balanced detection $I = I_y - I_x$. Figure is from [4] 20

3.1 A THz pulse is generated by a generation pulse (pump), propagated trough a sample, detected at the THz detector with a sampling pulse (probe). Reference measurements and sample measurements are explained in the next paragraphs. Figure from [55] 21
3.2 A typical TTDS time trace for sample and reference in transmission, with their corresponding Fourier-Transform. These are signals simulated with MATLAB. 23
3.3 The top shows the amplitude of the transfer function, while the bottom show the unwrapped phase. Unwrapping is used as a means of removing unwanted discontinuities when the phase jumps one cycle, i.e. when the phase reach $\pm 2\pi$. 24
3.4 The Absorption coefficient and refractive index of the simulated sample in Figure 3.2. Calculated using equations (3.4) and (3.5). From the calculated refractive index, we can see that the simulated sample is a Lorentz medium, with the Lorentzian fixed around 2 THz. 25
3.5 (LEFT) Fabry perot time trace from $300\mu m$ GaP (The EO-detection crystal) (RIGHT) The absolute value of the Discrete Fourier Transform of the pulse on the left. 27

4.1 Schematic of the experimental setup. 31
4.2 Picture of the finished setup in transmission mode. Red line is 795 nm laser light, blue is the second harmonic wave generated inside the BBO-crystal. The yellow transparent and blurred light is the THz radiation. The small white shape is the plasma. Note that the red and blue light is reflected onto the beam dump. 32
4.3 A raw data plot in transmission mode in air. The Y-axis shows the electric field strength, the x-axis is the delay line placement in mm with 0 as the middle of the translation stage. The negative X direction on the translation stage, corresponds to a smaller OPL for the IR-probe. 34
4.4 A typical time domain trace attained from the Setup with explanatory arrows. The black bordered arrows show multiple reflections inside the GaP crystal, and the black background arrows show multiple reflections inside the spectral splitter. The Gap crystal show multiple reflections from the reflections inside the spectral splitter, creating pulse trains. The reducing number of GaP reflections are a result of weaker signals as they are reflected back and forth inside the spectral splitter. 35
4.5 Two spectra from the Solstice laser amplification system, measured with a spectrometer and normalized to its peak power. (LEFT) MaiTai (RIGHT) Solstice 36
4.6 Typical spectrum of a THz-pulse in Air 37
4.7 Image taken from the web camera while aiming the pinholes towards the THz radiation. The red circle shows the pinhole closest to the camera, the yellow shows the second pinhole, and the green is the small pinhole seen in Figure 4.8. 40
4.8 (LEFT) The crosshair. (RIGHT) The calibration pinhole introduced on the other side of the sample holder. 41

4.9 (LEFT) The time domain trace of radiation that is partly hitting the sample. (RIGHT) The same trace after the pinhole size and sample position have been adjusted. The bigger peak value is mostly due to re-positioning of pinhole and sample, it is a proof of bad alignment on the left picture. . . . 42
4.10 (TOP) Rotation of the GaP (EO-crystal) used in this setup. The blue and red arrows are to clarify the rotation. (BOTTOM) Graph corresponding to equation (4.13) from [54]. 45
4.11 The two spectra recorded, one with (red) and one without(blue) polarizer. The scans were conducted on 50 mV sensitivity on the Lock-in, $100ms$ time constant over 5 runs. 47
4.12 Conceptual illustration of pulse stretching using (See [53]). The scheme for pulse compression is comparable. Pulse chirp relates to the distance between the mirror and grating. The distance for a longer wavelength is shorter than for the smaller wavelength, producing the chirp. Figure from [53]. 50
4.13 Time traces from the scans conducted between each increment, (TOP) May 29th (BOTTOM) April 7th. The upwards going y-axis shows the electric field amplitude, the horizontal axis on the right shows run number and the horizontal axis on the left is time in picosecond. 51
4.14 Scans from May 29th.The figures show the spectral amplitude seen from above. (TOP) Heat map of the spectral amplitude, w.r.t the colorbar to the right. (BOTTOM) Contour plot of the heat map on the top, w.r.t the colorbar on the top right. As we can see from both figures, the spectral bandwidth is greatest for values 0 to $4R$ and at 16L. 52
4.15 Scans from April 7th.The figures show the spectral amplitude seen from above. (TOP) Heat map of the spectral amplitude, w.r.t the colorbar to the right. (BOTTOM) Contour plot of the heat map on the top, w.r.t the colorbar on the top right. Similar behaviour to Figure 4.14, where the spectral bandwidth is greatest for values 0 to $4R$ and at 16L. 53
4.16 (LEFT) A typical spectrum for air with a dynamic range around 2000 calculated w.r.t the time trace. (RIGHT) Similar spectrum that includes correlated noise with a dynamic range above 10000. Light-Phonon interactions and phase mismatch between the THz-Pump and IR-probe are believed to be the reason for the ringing behavior. 55
4.17 Spectra from multiple runs with different sensitivity. The experiments took over 10 hours, to achieve the remarkable dynamic range. Consequently, imposing fluctuations in humidity. The relative humidity (RH) is the lowest humidity throughout the scan, the maximum for each scan is 5% RH. (TOP) Silicon $500\mu m$ (BOTTOM) Air 56
4.18 Detection response of the GaP crystal based on numerical analysis. The disparity between the figures is due to the different modeling. On the other hand, the ringing features are prominent for both models. (LEFT) Semi-logarithmic plot of the frequency response of GaP at various thicknesses. Figure from[8] (RIGHT) Normalized frequency response of GaP at several thicknesses. Figure from [73]. 57

4.19 The THz spectrum from a generation in photo-generated plasma. ABCD is used as the detection scheme, making it possible to detect ultra-broadband THz pulses. The laser specs are; pulse width of 100-fs, 1 KHz repetition rate and $3.2W$ average power, very similar to the laser in this thesis. Figure from [76] 57
4.20 CMK III thermal evaporator deposition system. The bell jar (vacuum chamber) can be lifted up to install deposition source and specimen. (LEFT) CMK III (RIGHT) Explanatory schematic of CMK III. 59
4.21 Comparison between THz signals measured with GaP with and without Cr MARC. Both of the curves are offset for clarity.(LEFT) Time trace with the frequency dependence of Cr MARC film. (RIGHT) Frequency domain data where arrows indicate water absorption lines. From [35] 60
4.22 Three time-windows and their corresponding spectrum to the left. (TOP) The longer time window, including main pulse, both artifacts and multiple FP-reflections from the GaP. (MID) Time window including main pulse the artifacts (BOTTOM) Time window only including the time window. We see from all the figures that removing the artifacts and FP-reflections gives a cleaner and less distorted spectrum. Note that the spectra bandwidth is limited to 19 THz because of the incremental step length of the measurements 62
4.23 The calculated refractive index (LEFT) and absorption coefficient (RIGHT) of the signals in Fig. 4.22. The top, middle, and bottom correspond to the top, middle and bottom signals in Fig. (4.22). We observe that the values are essentially the same for the refractive index and absorption coefficient for the three calculated cases but with less noise due to artifact and Fabry Perot reflections in the GaP. 63
4.24 (TOP) Time trace of a unpadded and padded signal. (BOTTOM) Absorption coefficient for the same sample, calculated with or without zero-padding. 64

5.1 (LEFT) The time trace of the two measurements (RIGHT) The corresponding spectra for the figure to the left. 66
5.2 Absorption coefficient in blue and the maximum measurable absorption in red. 67
5.3 (TOP) Absorption coefficient of Silicon (BOTTOM) Refractive index of Silicon 68
5.4 The two (LEFT) Semi-polished and (RIGHT) Optically polished Silicon samples. 69
5.5 The measured n and α for optically polished HRFZ Silicon in black and semi-polished HRFZ Silicon in blue. 70
5.6 Measured absorption at relative humidity 7% for sample measurement and 3% for reference 71
5.7 Time trace and spectra of the heavy doped n-type Silicon measurement . . 73
5.8 The calculated absorption coefficient and the corresponding maximum measurable absorption for optically polished n-type Silicon. 74

5.9 Reference in red and $1030.8\mu m$ fused Silica in black (TOP) The spectra from the two pulses. (BOTTOM) The time trace for sample and reference are separated by 3.33 ps, vertically offset for clarity. 75
5.10 (TOP) The calculated absorption coefficient and the maximum measurable absorption based on [28] for fused Silica. (BOTTOM) The calculated refractive index for fused Silica. 76
5.11 The calculated absorption coefficient of Fused Silica. 77
5.12 (LEFT) Time trace of the two THz pulses that are compared, black is $1000\mu m$ optical grad Germanium window and red is Air. The time delay between reference and air is 10.053 ps.Vertically offset for clarity. (RIGHT) The corresponding spectra for the pulses in the top. 78
5.13 (TOP) Absorption coefficient in blue and the maximum measurable absorption in red (BOTTOM) The calculated refractive index for the measurement. 79
5.14 Reference in red and 5mm [110]-cut GaP in black (TOP) The spectra from the two pulses. The ringing behavior after 6-7 THz is due to a correlated noise source. (BOTTOM) Reference and Sample pulse from air and 5mm thick [110]-cut GaP, respectively. The time trace for sample and reference are separated by 40.74 ps, vertically offset for clarity. 81
5.15 Calculated n and α from equation (3.6). The measurements are believable from 0.5 to 4 THz (TOP) Absorption coefficient in blue, and the maximal measurable absorption for this particular experiment in red. (BOTTOM) Refractive index between 0.5 THz to 7.2 THz. 82
5.16 Spectra and time trace for reference (Air) in red and 0.5mm KTP propagating in z-direction with polarization along the x axis in black (TOP) The spectra from the two pulses. (BOTTOM) Reference and Sample pulse from air and, respectively. The time trace for sample and reference are separated by 4.16 ps, vertically offset for clarity. 83
5.17 Calculated n and α for KTP in x-direction. (TOP) Absorption coefficient in blue, and the maximal measurable absorption for this particular experiment in red. (BOTTOM) Refractive index between 0.5 THz to 2.5 THz. 84
5.18 Broadening of the THz pulse due to assumable intense dispersion in THz regime. The reflection at 6 ps hits the detector before the decay from the main pulse is finished. Y-axis offset by -0.015. 85
5.19 (RIGHT) Caluculated absorption coefficient and maximum measurable absorption for KTP. (LEFT) Possible features 85
5.20 The new spectra and time trace when the Fabry-Perot reflections from the GaP are included. 86
5.21 Reflection measurement on a gold mirror. (TOP) Spectrum of the pulse (BOTTOM) Time trace 87

6.1 The absorption coefficient and refractive index calculated of the Germanium sample, for three different thicknesses, corresponding to the resolution of the caliper. 91

6.2 The absorption coefficient and refractive index calculated of the HRFZ Silicon sample, for three different thicknesses, corresponding to the resolution of the caliper. 92

D.1 Refractive index and absorption coefficient of Germanium from 0 to 2 THz, from [21] 115
D.2 Absorption coefficient of Czochralski grown Germanium from 0.6 to 5.4 THz at different temperatures from [51] 116
D.3 Refractive index and absorption coefficient of Fused Silica from 0 to 2 THz, from [21] 117
D.4 Refractive index and absorption coefficient of Silicon, from [14] 118
D.5 Phonon modes of GaP, from [56] 119
D.6 n (line trough circles) and α for GaP, from 0THz trough $5,5$THz. The refractive index is extrapolated from experimental data points. Figure from [48] 120
D.7 Phonon modes in KTP. From [37] 122

E.1 (TOP) Extrapolated phase and initial phase (MID) n for both cases (BOT) Absorption coefficient for both cases. 124

F.1 The reflection and transmission, seen from the plane of incidence, between an interface of two materials with refractive index n_1 and n_2, for a p-polarized wave (left) and a s-polarized wave (right). The yellow vectors represent the magnetic field $\vec{B}$ and the red vectors represent the Electric field $\vec{E}$. The black arrows are the propagation vector $\vec{k}$ 127
F.2 Fabry-Perot Etalon, Incident beam I is refracted and reflected at the first interface, then the refracted beam is again reflected and refracted at the other end of the medium. From Snell's law we see the angle of the incident wave θ_1 w.r.t. surface normal is the same as the angle of the transmitted wave. This cycle of reflection/refraction repeats itself as shown in the figure. 128
F.3 Gaussian beam with wave fronts in blue. The curvature $R(z)$ decrease closer to the focus, conversely it increases further away. The beam radius $w(z)$ is equal to $\sqrt{2}W_0$ at the Rayleigh length. The purple dotted line represent wave fronts which have an integer number wavelength between each wavefront (plane wave), the relative shift between the Gaussian wavefront and the purple wave fronts represent the Gouy Shift. 130

Abbreviations

BBO	=	β-Barium Borate
BS	=	Beam-splitter
c.c.	=	Complex conjugate
SHG	=	Second Harmonic Generation
TDS	=	Time-Domain Spectroscopy
THz	=	Terahertz
OPL	=	Optical Path Length
fs	=	Femtosecond
FSEOS	=	Free-space electro optic sampling
SNR	=	Signal-to-Noise Ratio
DR	=	Dynamic Range
AC	=	Alternating Current
GW	=	Gigawatt
PC	=	Photo conductive
FCA	=	Free carrier absorption

Symbols

$\vec{F}$	=	Force
q	=	Charge
$\vec{\nabla}$	=	Vector differential operator
$\vec{B}$	=	Magnetic flux density
$\vec{D}$	=	Displacement field strength
$\vec{P}$	=	Polarization density vector
$\vec{E}$	=	Electric field strength
$\vec{H}$	=	Magnetic field
$\vec{M}$	=	Magnetization
χ	=	Electric susceptibility
ϵ_0	=	Permittivity in free space
ϵ_r	=	Relative permittivity
μ_0	=	Permeability in free space
μ_r	=	Relative permeability
$\Re(X)$	=	Real part of X
Z	=	Set of integers
C	=	Set complex numbers
$\in$	=	Element in
$n(\omega)$	=	Complex index of refraction
$\hat{n}(\omega$	=	Refractive index
$\kappa(\omega)$	=	Extinction coefficent
$\alpha(\omega)$	=	Absorption coefficent
ω	=	Angular frequency
W_0	=	Beam waist
z_r	=	Rayleigh length
$w(z)$	=	Beam radius
k	=	Wave number
c	=	The speed of light in free space

Chapter 1

Introduction

T-rays, THz waves or Terahertz radiation are synonyms for electromagnetic radiation ranging from 0.1 to 10 THz. This frequency region lies between microwaves and infrared waves, as observed in Figure 1.1. The difficulties creating small and efficient sources have made the terahertz band one of the least explored regions of the electromagnetic spectrum. Various materials have unique spectral fingerprints in the THz regime. Also, many materials are transparent to THz radiation. Moreover, the low energy of 1-100 meV of THz photons makes it possible to measure low energy interactions in materials.

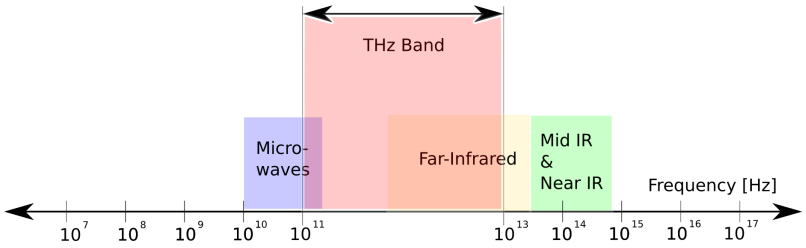

Figure 1.1: The THz band, the size of the THz band is exaggerated to emphasize which bands it lies in between, i.e. Far Infrared waves and microwaves.

The interesting properties of THz radiation have created research efforts in the fields of optoelectronics, medical diagnostics, security applications, industrial control processes and THz imaging techniques. [50]. In the latest March edition of OSA's Optics & Photonics News, Shams and Seeds discuss the possible integration of THz and wireless communication. We include highlights from the article in the next paragraph. Note that, a challenge for THz technology is the coupling between rotational transitions of water molecules, resulting in substantial absorption of THz in air.

The consumer market appetite for high definition interactive media through handheld

devices have continuously increased wireless data traffic. Cisco's visual networking index shows an increase in global monthly mobile data from 2.1 billion gigabytes in 2014 to 3.7 billion gigabytes in 2015. The continuous increase in data traffic presents fundamental challenges in wireless communication networks. The Shannon theorem states that for an average signal power the bandwidth of the channel limits the error free maximum data rate. The first solution is boosting the number of transmitted data bits per second using the same bandwidth. Demanding a higher signal-to-noise ratio, thus a higher transmitted power which is an issue for battery driven devices. The second solution is to use ultra-broad bandwidths above the 20GHz band, where there are potential in the uncharted THz region.

In this thesis, we study Terahertz Time-Domain spectroscopy (TTDS). TTDS was first introduced in 1989 by Van Exter, Fattinger, and Grischkowsky [66]. The principles of TTDS originate from microwave technology, and Fourier transform infrared spectroscopy [50]. A TTDS system measures both amplitude and phase of THz radiation, making it possible to characterize the complex refractive index of materials over a broad band of frequencies. The development of the regenerative amplified Ti:Sapphire laser [30] created a potential for new generation methods of THz. Typical generation schemes today are PCA, optical rectification, and generation by plasma. Commonly one use PCA or Pockel's effect for detection. By recording the temporal electric field of the generated THz pulse, one can extract the complex refractive index of material over a broad bandwidth.

Our TTDS setup uses plasma for generation and Pockel's effect for detection. We address problems related to the thickness of the EO-crystal. As well as studying how chirp, measurement time, polarization, noise and Fabry Perot reflections from elements in the setup are influencing the measured complex refractive index. By measuring a vast number of well-documented samples, we compare the extracted data to verify if the setup yields result comparable to the literature.

The thesis is constructed in the following way.

- Chapter 1 Introduction on THz properties, technology and relevance.
- Chapter 2 Theory on basic principles of electromagnetism and THz generation and detection.
- Chapter 3 Terahertz Time domain spectroscopy principles and calculations.
- Chapter 4 Introduction to the experimental setup, important experimental TTDS principles and improvements to the setup.
- Chapter 5 Results from measurements on Silicon,Fused Silica, Germanium, GaP and KTP.
- Chapter 6 Discussion based around the results from chapter 5.
- Chapter 7 Conclusive remarks about the setup, results and thesis.

Chapter 2

Theory

In the course of this chapter we introduce general principles of electromagnetism and THz theory, mostly based on [59] and [39]. Other sources are referenced.

2.1 Basics of Electromagnetics

As shown by Maxwell [42] and later rewritten by Olivier Heaviside, one can describe an electromagnetic field in differential form as

$$\vec{\nabla} \times \vec{H} = \vec{J} + \frac{d\vec{D}}{dt} \tag{2.1}$$

$$\vec{\nabla} \times \vec{E} = -\frac{d\vec{B}}{dt} \tag{2.2}$$

$$\vec{\nabla} \cdot \vec{D} = -\frac{\rho}{\epsilon_0} \tag{2.3}$$

$$\vec{\nabla} \cdot \vec{B} = 0 \tag{2.4}$$

where $\vec{E}$ and $\vec{B}$ is the electric field and magnetic flux density, ϵ_0 is the electric permittivity in vacuum, while $\vec{J}$ and $\frac{p}{\epsilon_0}$ are the current and free charges in a given medium, respectively. Maxwell's equations (2.1 - 2.4) together with the Lorentz force

$$\vec{F} = q(\vec{E} + \vec{v} \times \vec{B}), \tag{2.5}$$

compose the complete picture of classical electrodynamics. The electric displacement field $\vec{D}$ and the magnetic field $\vec{H}$ are related to to $\vec{E}$ and $\vec{B}$ by

$$\vec{D} = \epsilon_0 \vec{E} + \vec{P} = \epsilon_0(1 + \chi)\vec{E} = \epsilon\vec{E} \tag{2.6}$$

$$\vec{H} = \frac{1}{\mu_0}\vec{B} - \vec{M} = \frac{1}{\mu}\vec{B}, \tag{2.7}$$

where $\vec{P}$, $\vec{M}$, χ, ϵ and μ are the magnetization, polarization-density, the electric susceptibility, electric permittivity and permeability of a given medium, respectively. This thesis considers non-magnetic, i.e., $\vec{M} = 0$. We can relate the electric permittivity ϵ and the electric susceptibility χ to the relative permittivity ϵ_r by

$$\epsilon_r = \frac{\epsilon}{\epsilon_0} = 1 + \chi = n^2, \tag{2.8}$$

where n is the refractive index. The refractive index can be complex,

$$\hat{n}(\omega) = n(\omega) + i\kappa(\omega). \tag{2.9}$$

Where κ is the extinction coefficient. Since the extinction coefficient κ has no units, the norm is to use the absorption coefficient α which has units m^{-1}. The absorption coefficient relates the propagation distance of electromagnetic waves to loss due to absorption through different media,

$$\kappa(\omega) = \frac{\alpha(\omega)c}{2\omega}. \tag{2.10}$$

Wher c is the speed of light in vacuum. In a dielectric the relationship between the polarization density vector $\vec{P}$ and the applied electric field $\vec{E}$ is expressed as

$$\vec{P} = \epsilon_0 \chi \vec{E}. \tag{2.11}$$

An arbitrary medium may be a combination of nonlinear, dispersive, inhomogeneous and anisotropic. As a result of anisotropy χ is often written as a tensor. Each tensor element may be a function of frequency, electric field strength and so forth.

2.1.1 Polarization of materials

For an isotropic medium we may describe the polarization density $\mathcal{P}$ as a product of individual dipole moments p induced by the electric field $\mathcal{E}$.

$$\mathcal{P} = \mathbf{N}p. \tag{2.12}$$

Where $\mathbf{N}$ is the number of atoms. A nonlinearity may reside in either $\mathbf{N}$ or p. For electric fields that are small in comparison to interatomic electric fields, the relation between p and $\mathcal{E}$ is approximately linear. However, when the electric field strength become substantially compared to interatomic electric fields (around 10^5 to 10^8 V/m [59]) the relation becomes nonlinear. Conceptually this may be understood as a mass/spring system with linear/nonlinear spring constant (Lorentz Model in [59]). Another possibility is that the number of atoms $\mathbf{N}$ in a material that occupies energy levels involved in absorption/emission of electromagnetic waves are dependent on the intensity of the electromagnetic wave.

Normally, when its energy is small compared to the interatomic fields, the electric field sees a transparent material. This non-resonant atom-light interaction within the medium is expressed in terms of a linear susceptibility. As the amount of photons increase, i.e. light intensity increases, off-resonant effects can be seen. Stimulated scattering represent one

such phenomena. The nonlinear behaviour is expressed in terms of a nonlinear susceptibility. Quantum mechanical considerations are often unnecessary for practical purposes. Most nonlinear phenomena can be expressed by a Taylor expansion of the polarization density around the electric field $\mathcal{E}$.

$$\mathcal{P} = a_1\mathcal{E} + \frac{1}{2}a_2\mathcal{E}^2 + \frac{1}{6}a_3\mathcal{E}^3 + ... \tag{2.13}$$

The linear polarization density will dominate for small $\mathcal{E}$, i.e. $a_1 = \epsilon_0\chi$ where χ is the linear susceptibility. Writing the second and third order susceptibility based on the previous yields $\frac{1}{2}a_2 = \epsilon_0\chi^{(2)}$ and $\frac{1}{6}a_3 = \epsilon_0\chi^{(3)}$, respectively. An alternative expression of $\mathcal{P}$ is

$$\mathcal{P} = \epsilon_0(\chi\mathcal{E} + \chi^{(2)}\mathcal{E}^2 + \chi^{(3)}\mathcal{E}^3 + ...). \tag{2.14}$$

For an anisotropic nonlinear medium the polarization vector $\vec{P} = (\mathcal{P}_1, \mathcal{P}_2, \mathcal{P}_3)$ is also function of the electric field $\vec{E} = (\mathcal{E}_1, \mathcal{E}_2, \mathcal{E}_3)$, here the subscripts $1, 2, 3$ denotes the x, y and z components respectively. Comparable to equation (2.14), $(\mathcal{P}_1, \mathcal{P}_2, \mathcal{P}_3)$ is linear for small $(\mathcal{E}_1, \mathcal{E}_2, \mathcal{E}_3)$, but deviate slightly from linearity as $\vec{E}$ increase. Similar to the isotropic case, we can Taylor expand $\vec{P}$ w.r.t. the three components of $\vec{E}$

$$\mathcal{P}_i = \epsilon_0(\chi_{ij}\mathcal{E}_j + \chi^{(2)}_{ijk}\mathcal{E}_j\mathcal{E}_k + \chi^{(3)}_{ijkl}\mathcal{E}_j\mathcal{E}_k\mathcal{E}_l), \tag{2.15}$$

where we use Einsteins notation for tensors. Here χ_{ij},$\chi^{(2)}_{ijk}$ and $\chi^{(3)}_{ijkl}$ are elements of tensors that correspond to the scalar coefficients for χ,$\chi^{(2)}$ and $\chi^{(3)}$, respectively. From equation (2.15) we see that,

$$\chi^{(2)}_{ijk} \propto \frac{d^2\mathcal{P}_i}{d\mathcal{E}_j\mathcal{E}_k} \tag{2.16}$$

$$\chi^{(3)}_{ijkl} \propto \frac{d^3\mathcal{P}_i}{d\mathcal{E}_j\mathcal{E}_k\mathcal{E}_l}, \tag{2.17}$$

hence χ-tensor elements are invariant under coordinate permutations of j,k and l. In other words,

$$\chi^{(3)}_{ijkl} = \chi^{(3)}_{ikjl} = \chi^{(3)}_{ilkj} = \chi^{(3)}_{ijlk} \tag{2.18}$$

$$\chi^{(2)}_{ijk} = \chi^{(2)}_{ikj}. \tag{2.19}$$

For lossless,nondispersive media the χ-tensors are invariant for all the indexes i,j,k and l, this full-permutation symmetry does not hold for dispersive nonlinear media. For the second order term we can take advantage of the symmetry condition in equation (2.19), and we attain six independent combinations of j, k,namely $11, 22, 33, 23, 31, 12$. The usual formalism is to use one index for these, such that $\chi^{(2)}_{ijk} = \chi^{(2)}_{iJ}$. Put in other words $J \in [1, 2, 3, 4, 5, 6]$ is mapped to $jk \in [11, 22, 33, 23, 31, 12]$, respectively.

We can write the polarization density vector $\vec{P}$ in terms of different orders of nonlinearity,

$$\vec{P} = \vec{P^{(1)}} + \vec{P^{(2)}} + \vec{P^{(3)}} + ... \tag{2.20}$$

where

$$\vec{P^{(1)}} = \epsilon_0 \chi_{ij} \mathcal{E}_j \tag{2.21}$$

$$\vec{P^{(2)}} = \epsilon_0 \chi^{(2)}_{ijk} \mathcal{E}_j \mathcal{E}_k \tag{2.22}$$

$$\vec{P^{(3)}} = \epsilon_0 \chi^{(3)}_{ijkl} \mathcal{E}_j \mathcal{E}_k \mathcal{E}_l. \tag{2.23}$$

Here the superscript of $\vec{P^{(u))}}$ denotes the order of nonlinearity u. We can isolate the linear and nonlinear terms,

$$\vec{P} = \vec{P^{(1)}} + (\vec{P^{(2)}} + \vec{P^{(3)}} + ...) = \vec{P^{(1)}} + \vec{P^{(NL)}}, \tag{2.24}$$

where $\vec{P^{(NL)}}$ includes all the nonlinear terms of the polarization density vector. For different ordered media, we include different terms of this expanded polarization density vector. As an example, for a second order nonlinear medium where the higher order nonlinearities are negligible, we write the nonlinear term of the polarization density vector as

$$\vec{P^{(NL)}} = \vec{P^{(2)}} = \epsilon_0 \chi^{(2)}_{ijk} \mathcal{E}_j \mathcal{E}_k. \tag{2.25}$$

We can now rewrite equation (2.6) for the displacement field $\vec{D}$ in terms of the nonlinear polarization density vector in equation (2.24),

$$\vec{D} = \epsilon_0 \vec{E} + \vec{P^{(1)}} + \vec{P^{(NL)}} \tag{2.26}$$

$$\vec{D} = \epsilon_0 \vec{E} + \epsilon_0 \chi_{ij} \mathcal{E}_j + \vec{P^{(NL)}} \tag{2.27}$$

$$\vec{D} = \epsilon_0 (\vec{E} + \chi_{ij} \mathcal{E}_j) + \vec{P^{(NL)}} \tag{2.28}$$

$$\vec{D} = \epsilon_0 (\boldsymbol{I} + \boldsymbol{\chi}^{(1)}) \vec{E} + \vec{P^{(NL)}}. \tag{2.29}$$

Here $\boldsymbol{\chi}^{(1)}$ is the linear susceptibility tensor and $\boldsymbol{I}$ is the matrix of unity. For an isotropic material $\boldsymbol{I} + \boldsymbol{\chi}^{(1)}$ will become a scalar. Some use the notation $\boldsymbol{\epsilon}^{(1)}$ for $\boldsymbol{I} + \boldsymbol{\chi}^{(1)}$, which makes sense if we look at equation (2.8).

2.1.2 The wave equation

As discussed in section 2.1.1 and ultimately seen in equation (2.13), there is a nonlinear relationship between the polarization and applied electric field in a nonlinear medium. Operating the curl operator ($\times \vec{\nabla}$) on equation (2.2), we attain

$$\vec{\nabla} \times \vec{\nabla} \times \vec{E} + \mu_0 \frac{d^2 \vec{D}}{dt^2} = 0. \tag{2.30}$$

Using the vector calculus identity,

$$\vec{\nabla} \times \vec{\nabla} \times \vec{E} = \vec{\nabla}(\vec{\nabla} \cdot \vec{E}) - \vec{\nabla}^2 \vec{E} \tag{2.31}$$

we arrive at,

$$\vec{\nabla}(\vec{\nabla} \cdot \vec{E}) - \vec{\nabla}^2 \vec{E} + \mu_0 \frac{d^2 \vec{D}}{dt^2} = 0. \tag{2.32}$$

For a homogeneous medium, the term $\vec{\nabla} \cdot \vec{E}$ vanishes as $\vec{\nabla} \cdot \vec{D} = 0$. In the case of non-homogeneous media we apply SVEA (slowly varying envelope approximation) (see [9]), i.e. $\vec{\nabla} \cdot \vec{E}$ is negligible. Reducing equation (2.32) to

$$\vec{\nabla}^2 \vec{E} - \mu_0 \frac{d^2 \vec{D}}{dt^2} = 0, \tag{2.33}$$

$$\vec{\nabla}^2 \vec{E} - \mu_0 \epsilon_0 \frac{d^2 (\boldsymbol{I} + \boldsymbol{\chi}^{(1)}) \vec{E} + P^{(\vec{NL})}}{dt^2} = 0, \tag{2.34}$$

$$\vec{\nabla}^2 \vec{E} - \mu_0 \epsilon_0 \boldsymbol{\epsilon^{(1)}} \frac{d^2 \vec{E}}{dt^2} = \mu_0 \frac{d^2 P^{(\vec{NL})}}{dt^2}. \tag{2.35}$$

Equation (2.35) is an inhomogeneous wave equation, where the nonlinear response of the medium acts as a source term on the right side. By removing the source term we return to the wave equation for free waves propagating in a medium of linear refractive index $\boldsymbol{\epsilon^{(1)}} = n^2$.

More often than not the medium is dispersive and dissipative, such that the dielectric tensor $\boldsymbol{\epsilon^{(1)}}$ is frequency dependent (dispersive) and complex (absorptive). Representing the electric field, displacement field and the nonlinear polarization as a sum of their frequencies, we can account for each frequency component separately. Giving the permittivity tensor

$$\boldsymbol{\epsilon^{(1)}(\omega_n)}, \tag{2.36}$$

where ω_n refers to the n'th angular frequency component of the wave and where $\boldsymbol{\epsilon^{(1)}}(\omega_n)$ has elements which $\in \mathbb{C}$. The nonlinear polarization is important for both generation and detection of THz radiation, and will be discussed in section 2.5.

For the last part of this section we assume the medium to be linear and isotropic, reducing the wave equation to its simplest form.

$$\vec{\nabla} \vec{E} = \mu_0 \epsilon_0 \epsilon^{(1)} \frac{d^2 \vec{E}}{dt^2} = \frac{1}{v^2} \frac{d^2 \vec{E}}{dt^2}. \tag{2.37}$$

Here v is the phase velocity of the wave in the medium, described by

$$v = \frac{c}{n} = \frac{\epsilon_0 \mu_0}{n}. \tag{2.38}$$

A simple solution to equation (2.37) is a linearly polarized monochromatic wave propagating in z-direction with angular frequency ω,

$$E(z,t) = A e^{i(kz - \omega t)}. \tag{2.39}$$

Where $k = \frac{\omega n}{c}$ is known as the wave number and A is the envelope of the wave. Substituting the complex representation of the refractive index (equation (2.9)) into (2.39) yields,

$$E(z,t) = A e^{i(\omega(n(\omega)z/c - t)} e^{-\omega \kappa(\omega) z/c} \tag{2.40}$$

$$E(z,t) = A e^{i(\omega(n(\omega)z/c - t)} e^{-\alpha(\omega) z/2}. \tag{2.41}$$

Where we have used equation (2.10) to attain the latter equation.

2.2 Ultrashort Chirped Pulses

Ultrafast optics is a sub-field of optics which describes and investigates the generation and propagation of electromagnetic pulses in the nano to atto second regime (10^{-9}s to 10^{-18}s). In this section we will look at some fundamental features of Gaussian pulses, which can be translated into any other pulse shape without loss of generality [62]. The generation of ultra short pulses is only briefly touched upon, but the reader is referred to any introductory book on the topic, see [62, 69, 16].

Lasers producing ultrashort pulses are known as ultrafast lasers. Modulation plays a key role in creating ultrashort pulses. There are two main types of modulation, passive and active modulation or passive and active mode-locking, respectively. Active mode-locking has an externally applied modulator (e.g. an acousto-optic modulator), while passive mode locking uses nonlinear materials to self-modulate. Nonlinear materials used in passive mode-locking, for example a saturable absorbers, are driven by short pulses and can modulate much faster than an externally driven modulator. Hence the shortest pulses generated to date are done by passive mode-locking [69].

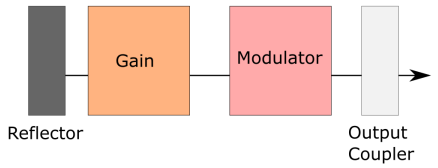

Figure 2.1: Brief visualization of the generation of an ultra short laser pulse with active mode-locking. Exchanging the modulator with for example a saturable absorber will yield a passive mode-locking scheme.

Description of the time envelope of an optical pulse with a carrier frequency ω_0 can be seen in Figure 2.2 and written as,

$$E(t) = e^{-at^2} e^{-i(\omega_0 t + bt^2)}. \tag{2.42}$$

Here the $a - jb$ is the *complex* Gaussian parameter. As we will see later its real and imaginary part can be associated with the instantaneous intensity $I(t)$ and instantaneous phase/frequency, respectively. Note that the spatial extent of a femtosecond pulse in the direction of propagation is in the scale of micrometers. This spatial extent is limited by central frequency ω_0 of the wave known as the fundamental-pulse-width [69]. An introduction on the spatial extent in the perpendicular plane to propagation of Gaussian beams is included in Appendix F.3.

The complex Gaussian parameter and its real part, can be used to describe the instantaneous intensity as

$$I(t) = |E(t)|^2 = |e^{-2at^2}| = e^{-4\ln(2)(t/\tau_p)^2}. \tag{2.43}$$

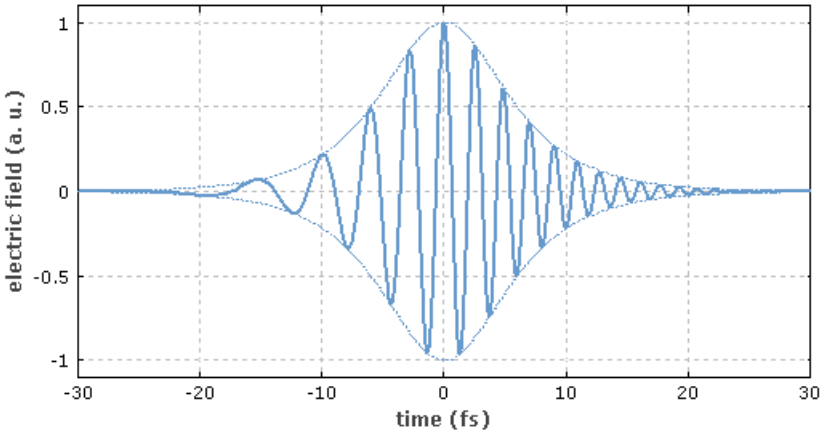

Figure 2.2: A chirped pulse where the instantaneous frequency increase with time, from [52]

The pulsewidth, defined as τ_p, is calculated by the commonly used FWHM (full width half maximum) of the intensity $I(t)$. We can relate the parameter a to the pulsewidth as follows,

$$\tau_p = \sqrt{\frac{2\ln(2)}{a}}. \tag{2.44}$$

Mathematically speaking, big a gives a short pulse and vica versa. For a pulse with intensity FWHM of 100fs, a would be in the order of 10^{26}.

The imaginary part of the Gaussian parameter, can be used to analyze the frequency change of the sinusoidal signal within the Gaussian pulse itself known as the $chirp$ of the pulse. The instantaneous phase ϕ_{inst} can be found through

$$E(t) \propto e^{-i(\omega_0 t + bt^2)} = e^{-i\phi_{inst}(t)}, \tag{2.45}$$

and is written as

$$\phi_{inst}(t) = \omega_0 t + bt^2. \tag{2.46}$$

The instantaneous frequency of the sinusoidal signal within the Gaussian envelope is interpreted neatly in the words of Anthony Siegman, as "... the rate at which the total phase of the sinusoidal signal rotates forward, or alternatively 2π the number of cycles completed per unit time, as measured in any small time interval ..." [62]. Mathematically this translates to

$$\omega_{sin} = \frac{d\phi_{inst}(t)}{dt}, \tag{2.47}$$

which in this case leads to

$$\omega_{sin} = \omega_0 + 2bt. \tag{2.48}$$

The implication of equation (2.48) is that any Gaussian pulse with nonzero b has a linearly varying instantaneous frequency w.r.t time. This variation is the chirp, and the

pulse is known as a chirped pulse. Quantifying the effects of the chirp in a system may be important as it can cause signal degradation. Usually frequency dependent time delay and chirp in conjunction leads to the aforementioned. These effects can be negated by changing the chirp from the Laser.

2.3 Second harmonic generation (SHG)

Second harmonic generation or SHG is the nonlinear phenomenon where two photons of angular frequency ω fuse into one photon of angular frequency 2ω. It can be shown that this is an effect that resides in the second order susceptibility tensor. We will now consider the response of a nonlinear medium to a harmonic electric field with angular frequency ω and amplitude E

$$\mathcal{E}(t) = Ee^{-i\omega t} + c.c. \tag{2.49}$$

Where c.c. denote the complex conjugate. We substitute equation (2.49) into equation (2.25), yielding

$$\mathcal{P}(t) = 2\epsilon_0\chi^{(2)}_{ijk}EE^* + [\epsilon_0\chi^{(2)}_{ijk}E^2e^{-i2\omega t} + c.c.] \tag{2.50}$$

From the nonlinear wave equation (2.35), we see that the source term $S(t)$ corresponding to equation (2.50), has a component of frequency 2ω, with complex amplitude equal

$$S(t) = 4\mu_0\omega^2\epsilon_0\chi^{(2)}_{ijk}E^2 + c.c.. \tag{2.51}$$

Since the amplitude of the second harmonic wave is proportional to the source $S(t)$, the intensity $I_{2\omega}$is proportional to the fundamental wave

$$I_{2\omega} \propto \mid S(t) \mid^2 \propto \frac{\mid E \mid^2}{2\eta}, \tag{2.52}$$

where η is the impedance of the medium. One of the most commonly used materials today for SHG is β-Barium borate (BBO). BBO belongs to the trigonal lattice with point group (3m) [10]. We assume that our light source is linearly polarized in y-direction and propagating in z-direction, thus we can write it as

$$E(z,t) = A(z,t)e^{i(kz-\omega t)}\hat{y}. \tag{2.53}$$

Where A is the complex envelope. From equation (2.15) second-order nonlinear relation between the polarization density and the incident optical wave can be expressed as

$$\vec{P^{(2)}} = \boldsymbol{\chi}^{(2)}E(z,t)E(z,t) \tag{2.54}$$

$$... = \boldsymbol{\chi}^{(2)}(A^2(z,t)e^{i2(kz-\omega t)} + A(z,t)A^*(z,t)) \tag{2.55}$$

From equation (2.29), we see that the electric displacement field $\vec{D}$ radiates with the same frequencies as the polarization density vector. In our case, $\vec{P^{(2)}}$ radiates with angular frequency 2ω, this radiation induces a new electrical field with frequency 2ω. This can be written as

$$\vec{D} \propto \vec{P}^{(2)} \propto e^{i2\omega}. \tag{2.56}$$

Returning to the BBO-crystal, the polarization of the second harmonic wave will lie along the extraordinary axis of the crystal [10]. We now decompose the incident wave of angular frequency ω along the ordinary and extraordinary axis of BBO as E_{n_o} and E_{n_e}, respectively. In addition, we assume that all of the electric field polarized along the extraordinary axis is going trough the process of equation (2.50).

$$\vec{P}(t) = \{2\epsilon_0 \chi^{(2)}_{ijk} E_{n_e} E^*_{n_e} + [\epsilon_0 \chi^{(2)}_{ijk} E^2_{n_e} e^{-i2\omega t} + c.c.]\}\hat{x} + \epsilon_0 \chi^{(1)_{ijk}} E_{n_o}(z,t)\hat{y} \tag{2.57}$$

In this approximation, the field along the extraordinary axis is directly proportional to the generated second harmonic. Thus any rotation would change the amount of second harmonic generated. This is similar to [9, 46], although these references use a detailed model.

The second harmonic generation is an important part of generating THz in air-filament, because of the increased amount of THz radiation generated as the second harmonic is introduced, as discussed in section 2.5.3.

2.4 Pockel's Effect in $\bar{4}3m$ Crystals

A fundamental part to the detection scheme (see section 2.6) in this thesis is Pockel's effect, specifically for the symmetry group $\bar{4}3m$ (GaP). The discussion is treated with respect to the index ellipsoid and will mainly focus on the aforementioned symmetry group. The introduction to the topic is based on, and the reader is referred to [75] for details.

Returning to equation (2.29), with the assumption of no higher order susceptibility tensors, $P^{(\vec{NL})} = 0$, we can write the displacement field as

$$\vec{D} = \epsilon_0(\boldsymbol{I} + \boldsymbol{\chi}^{(1)})\vec{E}. \tag{2.58}$$

By choosing the principal coordinate system, all the off axis elements of $\boldsymbol{\chi}^{(1)}$ becomes zero. We can write the electric permeability ϵ_{ij} as,

$$\epsilon_{11} = \epsilon_0(1 + \chi_{11}) \tag{2.59}$$
$$\epsilon_{22} = \epsilon_0(1 + \chi_{22}) \tag{2.60}$$
$$\epsilon_{33} = \epsilon_0(1 + \chi_{33}). \tag{2.61}$$

By postulating a solution of the wave equation in the same form as in equation (2.39), with a wave propagating in the z-direction, we see that the wave vectors in x and y direction becomes

$$k_x = \omega\sqrt{\mu_0 \epsilon_{11}} \tag{2.62}$$
$$k_y = \omega\sqrt{\mu_0 \epsilon_{22}}. \tag{2.63}$$

In an anistropic uniaxial crystal ($\epsilon_{11} \neq \epsilon_{22}$), the phase velocity of the two parts of the optical beam differs, this is known as $birefringence$. Generalizing this case to propagation along some arbitrary direction inside a crystal, the two allowed wave polarizations and their respective phase velocities have to be determined. This is commonly done with the index ellipsoid,

$$\frac{x^2}{n_x^2} + \frac{y^2}{n_y^2} + \frac{z^2}{n_z^2} = 1. \tag{2.64}$$

Here the major axis of the ellipsoid is along x,y and z with respective lengths $2n_x$,$2n_y$ and $2n_z$. Determining the polarization and phase velocity of an optical beam is done by finding the intersection between the ellipsoid and the normal plane of propagation through the origin of the ellipsoid. This yields an ellipse with major and minor axis equal $2n_1$ and $2n_2$, where n_1 and n_2 are the refractive indices of the solutions.

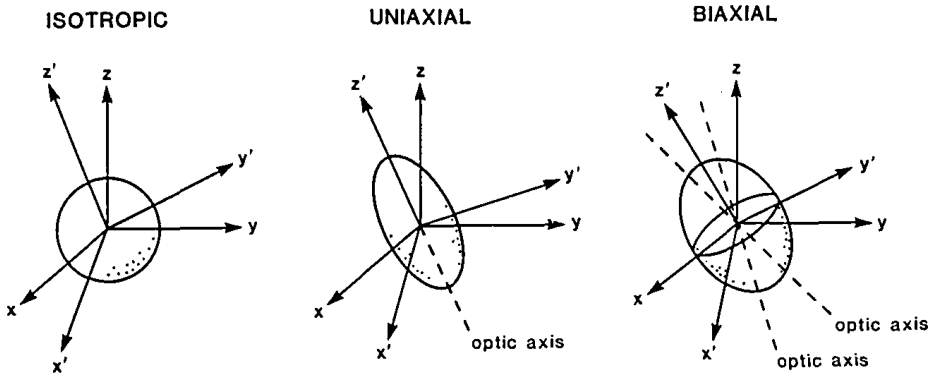

Figure 2.3: The index ellipsoid for an isotropic $n_x = n_y = n_x$, an uniaxial $n_x = n_y \neq n_z$ and a biaxial $n_x \neq n_y \neq n_z$ crystal . The principal axis are shown as z',y' and x'. Figure from [41].

Considering an uniaxial system as shown in the middle of Figure 2.3, and taking the direction of propagation along x'. We define the principle refractive indices $n_o = n_{y'}$ and $n_e = n_{z'}$ as the $ordinary$ and $extraordinary$ refractive indices of the uniaxial crystal, respectively. The ellipse for this system become

$$\frac{y'^2}{n_o^2} + \frac{z'^2}{n_e^2} = 1. \tag{2.65}$$

By geometric considerations of the ellipse, this can be rewritten as

$$\frac{1}{n_e^2} = \frac{\cos^2\theta}{n_o^2} + \frac{\sin^2\theta}{n_e^2} \tag{2.66}$$

Where θ is defined as the angle between the direction of propagation and the z' axis.

Pockel's effect, in the words of Amnon Yariv [75], "... is the change in the indices of the ordinary and extraordinary rays that is caused by and is proportional to an applied electric field ...". The effect is present in crystals which do not inhibit inversion symmetry [75].

In order to finally arrive at Pockel's effect expressed as a tensor, we rewrite equation (2.64) with the existence of an electric field as

$$\frac{x^2}{n_{(1)}^2} + \frac{y^2}{n_{(2)}^2} + \frac{z^2}{n_{(3)}^2} + 2\frac{yz}{n_{(4)}^2} + 2\frac{xz}{n_{(5)}^2} + 2\frac{xy}{n_{(5)}^2} = 1. \tag{2.67}$$

Which for zero applied electric field and x, y, z chosen along the principal axes x', y', z' should return to equation (2.64). Such that the indices $n_{(i)}$ becomes

$$\frac{1}{n_{(1)}^2} = \frac{1}{n_x^2}, \frac{1}{n_{(2)}^2} = \frac{1}{n_y^2}, \frac{1}{n_{(3)}^2} = \frac{1}{n_z^2} \tag{2.68}$$

$$\frac{1}{n_{(4)}^2} = \frac{1}{n_{(5)}^2} = \frac{1}{n_{(6)}^2} = 0. \tag{2.69}$$

The linear change due to an applied constant electric field

$$\vec{E} = (\mathcal{E}_x, \mathcal{E}_y, \mathcal{E}_z) = (\mathcal{E}_1, \mathcal{E}_2, \mathcal{E}_3),$$

in each of the indices $n_{(i)}$ can be written as

$$\Delta\frac{1}{n_{(i)}} = \sum_{n=1}^{3} r_{in}\mathcal{E}_n \tag{2.70}$$

Here r_{in} is the elements of the electrooptic tensor, and we can write out all the elements in terms of matrices

$$\begin{bmatrix} \Delta\frac{1}{n_{(1)}} \\ \Delta\frac{1}{n_{(2)}} \\ \Delta\frac{1}{n_{(3)}} \\ \Delta\frac{1}{n_{(4)}} \\ \Delta\frac{1}{n_{(5)}} \\ \Delta\frac{1}{n_{(6)}} \end{bmatrix} = \begin{bmatrix} r_{11} & r_{12} & r_{13} \\ r_{21} & r_{22} & r_{23} \\ r_{31} & r_{32} & r_{33} \\ r_{41} & r_{42} & r_{43} \\ r_{51} & r_{52} & r_{53} \\ r_{61} & r_{62} & r_{63} \end{bmatrix} \begin{bmatrix} \mathcal{E}_1 \\ \mathcal{E}_2 \\ \mathcal{E}_3 \end{bmatrix}. \tag{2.71}$$

Following any tables that relates electrooptic coefficients to their symmetry group, as in [75], one can appreciate that the $\bar{4}3m$ symmetry group have three non-zero and equal elements, namely r_{41},$r_{52} = r_{41}$ and $r_{63} = r_{41}$. Letting the electric field propagate in $< 110 >$ direction, the E-field can be written as

$$\vec{E} = \frac{E}{\sqrt{2}}((\hat{x} + \hat{y})), \tag{2.72}$$

where $\hat{x}$ and $\hat{y}$ is the unit vectors along the cubic edges of the $\bar{4}3m$ crystal. The resulting index ellipsoid is

$$\frac{x^2 + y^2 + z^2}{n_o^2} + \sqrt{2}r_{41}E(xy + zx) = 1 \tag{2.73}$$

rotating the coordinate system of equation (2.73) until there are no mixed terms, the refractive indices becomes

$$n_{x'} = n_o + \frac{1}{2} n_o^3 r_{41} \mathcal{E} \tag{2.74}$$

$$n_{y'} = n_o - \frac{1}{2} n_o^3 r_{41} \mathcal{E} \tag{2.75}$$

$$n_{z'} = n_o. \tag{2.76}$$

Here z',y' and x' correspond to the coordinate system that gives no mixed terms in equation (2.73). This result is used in section 2.6, where detection of terahertz radiation using an $\bar{4}3m$ electrooptic crystal (GaP) is introduced.

2.5 Generation of THz pulses

Multiple arrangements for generating THz waves exist. In this thesis the work is mainly concerned with broadband THz pulses close to the single-cycle limit. Some schemes for generating such pulses will be explained in this section. Most of the formulations and mathematics in this section are based on [39].

2.5.1 Photoconductive antenna

Given that the energy is sufficient, photons can excite charge carriers when incident on a semiconductor surface. Leading to that the excited charge carriers in the localized incident area have increased mobility. This feature can be used as a switch or as a Photoconductive antenna (PCA). In a PCA, a voltage is set between two electrodes (as can be seen from equation (2.5)). A schematic outline of a PC antenna is included in Figure 2.4.

One can approximate the radiation from the PC antenna as a Hertzian dipole where the antenna size is much smaller than the wavelength of the radiated radiation. This is a valid approximation as the source size is approximately the same size as the incoming optical pulse spot size (around $10\mu m$), whilst the wavelength of the THz wave is around $300\mu m$ for 1 THz [39]. By only investigating the far field, i.e. where the propagation distance (r) is much bigger than the wavelength of THz , we arrive at the equation for far field THz dipole radiation in free space

$$\vec{E}_{THz} = \frac{\mu_0}{4\pi} \frac{\sin\theta}{r} \frac{d^2}{dt_r^2} [p(t_r)] \hat{\theta}. \tag{2.77}$$

Here θ is the angle between semiconductor front surface or i.e. the direction of the THz radiation ($\theta = \frac{\pi}{2}$ for radiation as shown in Figure 2.4), $p(t_r)$ is the dipole moment of the source at the retarded time $t_r = t - r/c$. Relating carrier density $\rho(r,t)$ to the dipole moment , and using the continuity relation

$$\vec{\nabla} \cdot \vec{J} + \frac{d\rho}{dt} = 0. \tag{2.78}$$

We arrive at

$$\frac{dp(t)}{dt} = W I_{PC}(t). \tag{2.79}$$

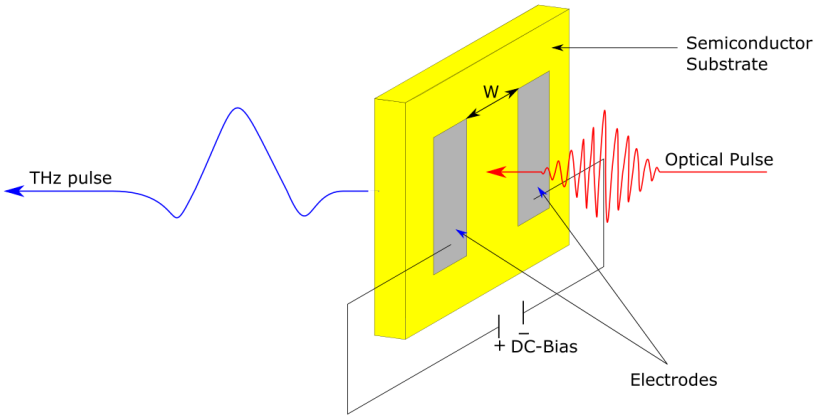

Figure 2.4: A DC-biased PC antenna. The semiconductor substrate is shown in yellow, metallic electrodes are connected to the DC bias, an optical pulse (red) is incident on the area between these electrodes and a THz pulse (blue) is generated. The length between the electrodes are given as W.

Where W is the spot size, which is approximated to be the same size as the distance between the electrodes in Figure 2.4, and I_{PC} is the photo-current. This relates the emitted THz radiation to the time derivative of the current flowing from one electrode to the other by

$$\vec{E}_{THz} = \frac{\mu_0 W}{4\pi}\frac{\sin\theta}{r}\frac{d}{dt_r}[I_{PC}(t_r)]\hat{\theta}. \propto \frac{dI_{PC}(t)}{dt} \tag{2.80}$$

With small pump power and DC bias the field amplitude increases linearly with pump power, but is saturated quickly for increasing optical pulse power. This saturation is due to the small area between the two electrodes, and is strong relative to other THz emitter. Thus the THz conversion yield is great at small pump powers. The maximum radiation power is limited by the breakdown power of the substrate material. [39]

Exchanging the DC-bias with an ampere-meter we can measure the current flowing from one electrode to another, thus measuring the THz radiation. Instead of the DC-bias sweeping charge carriers, we let the THz pulse be incident on the semiconductor surface which in turn accelerates the charge carriers excited by the optical pulse. By changing the arrival time of the optical pulse relative to the THz pulse, we can measure the electric THz field as a function of time.

2.5.2 Optical recitification

In section 2.1.1, we discussed the occurrence of nonlinear effects in materials due to intense incident optical light on a dielectric material. Optical rectification utilizes second order nonlinear effects to generate THz. Rewriting equation (2.25), and accounting for

time dependence, we attain

$$\vec{P(t)} = \vec{P^{(2)}(t)} = \epsilon_0 \boldsymbol{\chi}^{(2)} \vec{E}^2(t). \tag{2.81}$$

Where $E(t)$ is a laser pulse with multiple frequency components

$$E(t) = \vec{A_1(t)} e^{-i\omega_1 t} + \vec{A_2(t)} e^{-i\omega_2 t} + c.c., \tag{2.82}$$

where A_i is the time dependent envelopes and ω_i is their respective carrier frequency and c.c. is the complex conjugate. In special cases of $\omega_1 = \omega_2$ we can rewrite equation (2.81) ,

$$\begin{aligned}\vec{P(t)} = \epsilon_0 \boldsymbol{\chi}^{(2)} [\vec{A_1}^{\,2}(t) e^{-2i\omega t} + \vec{A_2}^{\,2}(t) e^{-2i\omega t} + 2\vec{A_1}(t)\vec{A_2}(t) e^{-2i\omega t} + \vec{A_1}(t)\vec{A_2}^{\,*}(t) + c.c.] \\ + 2\epsilon_0 \boldsymbol{\chi}^{(2)} [\vec{A_1}(t)\vec{A_1}^{\,*}(t) + \vec{A_2}(t)\vec{A_2}^{\,*}(t)].\end{aligned} \tag{2.83}$$

We see the immediate resemblance to equation (2.54) where we have terms of second harmonic generation. The terms which are of concern are the optical rectification terms which have no frequency dependency. These vary with the time dependent envelope of the optically incident pulse. For a femtosecond laser pulse, optical rectification will yield a THz varying polarization, and as $\vec{D}(t) \propto \vec{P}(t)$ one generate THz radiation.

2.5.3 Generation of THz in Air

By focusing a high power laser one can generate a plasma in thin air. The photo-generated plasma produces radiation ranging from soft x-rays to microwaves. The complete physical description of the interaction that provides the radiation is not understood, some authors use a four-wave-mixing model while some use a miniaturized polarization model. The generation method was first demonstrated by Hamster [23, 22].

Later, D. J. Cook and R. M. Hochstrasser [13] found that mixing an optical wave with its second-harmonic created a huge enhancement of the efficiency of THz generation. Furthermore [74, 33] established that the polarity and strength of the THz field are controlled by the relative phase between the fundamental and second harmonic wave. More accurately the THz radiation is maximized when the polarization of the fundamental and the SH waves are parallel, while it is minimized when the polarizations are perpendicular.

Generation of second harmonic waves are commonly done through the use of nonlinear second harmonic crystals. One of the most commonly used materials for this is Type-I β-barium borate (BBO) crystals. In these kinds of crystals, the polarization of the fundamental wave should be perpendicular to the extraordinary axis of the BBO crystal to maximize the generation of the SH wave [74]. The generated SH wave will then be polarized parallel to the e-axis [10], hence the second and fundamental wave coming out from the BBO is perpendicularly polarized, as can bee seen from Figure 2.5.

Expressing the fundamental and the second harmonic wave as

$$E_1(t) = A_\omega e^{-i\omega t} \tag{2.84}$$

$$E_2(t) = A_{2\omega} e^{-i2\omega t + \phi}, \tag{2.85}$$

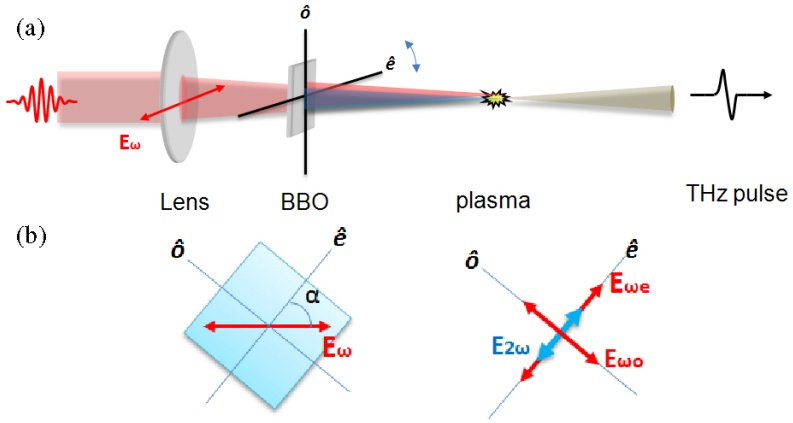

Figure 2.5: (a) Picture showing the experimental setup for generation of THz, utilizing a BBO crystal and a Lens. (b) Type-1 BBO crystal generation of second harmonic wave. Note that only a fraction of the fundamental wave have the same polarization as the SH-wave. Picture from [46]

where A_i is the complex envelopes for each wave and ϕ is the relative phase between the two waves. As shown in Figure 2.5, cold plasma is created due to the high energy concentration in the focus point. The terahertz electric field E_{THz} is proportional to the time derivative of the rectified current ($\frac{d}{dt}\vec{J}^{(3)}(t)$) generated inside the plasma [39]

$$\vec{E}_{THz}(t) \propto \frac{d}{dt}\vec{J}^{(3)}(t). \tag{2.86}$$

We can then inspect the frequency domain of equation (2.86) , which yields

$$\vec{E}_{THz}(\omega_T) \propto -i\omega_T \vec{J}^{(3)}(\omega_T) + c.c. \tag{2.87}$$

where

$$J^{(3)} \propto \sigma^{(3)} A_{2\omega} A_\omega^2 e^{-i\phi}, \tag{2.88}$$

and $\sigma^{(3)}$ is he third order nonlinear conductivity. This results in the generated THz field being proportional to

$$\vec{E}_{THz} \propto \sigma^{(3)} A_{2\omega} A_\omega^2 \sin\phi \tag{2.89}$$

2.6 Detection of THz by Free-space electro optic sampling (FSEOS)

One can achieve detection of broadband THz pulses with FSEOS. The scheme is based around the Pockel's effect (see section 2.4). A weak Near-IR pulse and the pump THz pulse propagates collinearly through an EO crystal. If the probe pulse is smaller or in proportion to half a cycle of the THz pulse, the probe sees a "constant" birefringence induced by the THz pulse [55]. The resulting instantaneous phase retardance from this

birefringence can then be detected. By adjusting the time delay between the pump and probe one can then sample the THz pulse $E_{THz}(t)$. FSEOS measures both amplitude and phase of an electric field with a precision of at least 10^{-2} rad [39]. A typical scheme for FSEOS is included in Figure 2.6.

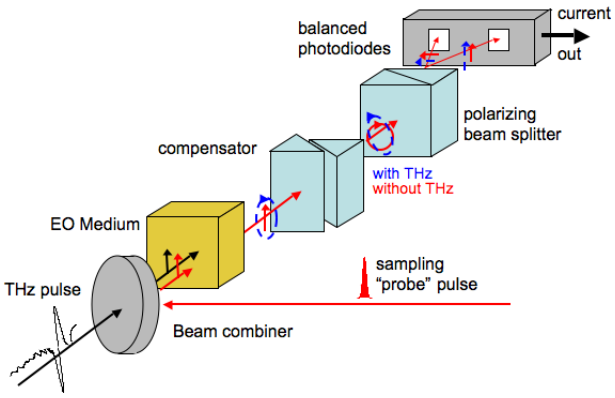

Figure 2.6: Scheme for FSEOS, an optic sampling pulse and a pump THz pulse propagates collineraly towards an electro-optic medium, the outgoing pulse from the EO medium propagates through a compensator, typically a $\frac{\lambda}{4}$ waveplate. The wollaston prism (polarizing beam spltter) creates a decomposition of the pulse in y and x directions. These pulses are fed to two photo-diodes which are cross connected to an anode and cathode, resulting in balanced detection $I = I_y - I_x$. Figure is from [4]

Following the calculations outlined in [39] and section 2.4, we arrive at

$$I = I_y - I_x = I_0 \Delta\phi = \frac{I_0 \omega L}{c} n_O^3 \mathbf{r} E_{THz} \propto E_{THz}. \tag{2.90}$$

Where I is the detected intensity, $\Delta\phi$ is the relative phase change due to birefringence inside the EO crystal, I_0 is the incident probe intensity, n_O is the refractive index of the EO-crystal at optical frequencies, $\mathbf{r}$ is the electro-optic tensor, L is the optical path length through the EO-crystal ω and c is the angular frequency and the speed of light for the probe pulse, respectively. An important aspect to FSEOS is the alignment procedure, here one blocks the THz-Pulse shown in Figure 2.6, and align the $\lambda/4$-waveplate such that the outgoing probe pulse is circularly polarized, making equation (2.90) equal zero. After this alignment, one can unblock the THz pulse, and the detected signal is solely due to the birefringence induced in the EO-crystal by the THz pulse.

The tensor properties of the detection , $\mathbf{r}$ in equation (2.90), implies that the orientation and crystal axes of the EO-crystal is vital to the nonlinear process in the detection scheme. Two of the normal electro-optic crystal used in FSEOS are ZnTe and GaP, both of zincblende structure ($\bar{4}3m$). For the case of a $\langle 1\,1\,0\rangle$-oriented zincblende crystal the THz field and the optical pulse should be aligned in $[\bar{1}\,1\,0]$, and the optical pulse should be parallel to the THz field, to maximize the birefringence in the zincblende electro-optic crystal [39].

Chapter 3

Terahertz Time-Domain Spectroscopy

This chapter gives an introduction to Terahertz Time-Domain Spectroscopy (TTDS). It will describe the general idea of how to measure signals and how to extract optical parameters from these signals. Simulated signals, as described in [63], are used to show the steps with which optical parameters are extracted.

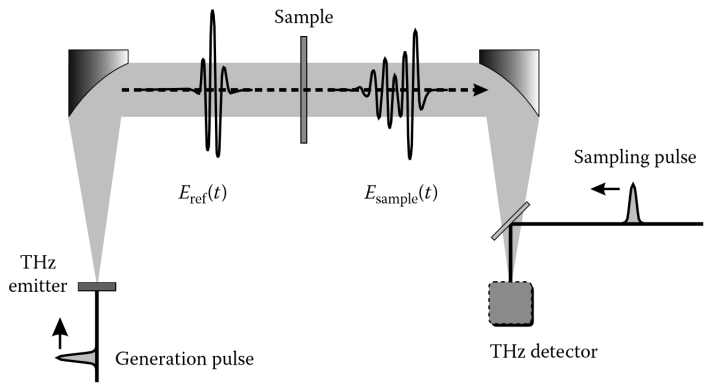

Figure 3.1: A THz pulse is generated by a generation pulse (pump), propagated trough a sample, detected at the THz detector with a sampling pulse (probe). Reference measurements and sample measurements are explained in the next paragraphs. Figure from [55]

3.1 Measurement principle

Terahertz Time-domain spectroscopy is a pump-probe spectroscopy technique, where broadband THz pulses are measured at different points in time using FSEOS. A typical time-domain signal and its Fourier transform is presented in Figure 3.2. The probing makes it possible to fully describe the temporal profile of the wave, i.e. both its amplitude and phase. A typical measurement is a two-step process. Firstly a measurement of the setup is performed, i.e. without any sample, this is called the reference measurement. The second measurement is done with a sample in the path of the THz radiation, known as the sample measurement. By comparing the spectral profile of the two measurements, one can extract the complex refractive index.

Measurements can be done with T-rays reflecting off or transmitting through a sample. Transmission measurements introduce a relative time delay between the reference measurement pulse and the sample measurement pulse. Reflection measurements, with the exception of some special techniques (e.g. ATR), requires a physical replacement of a mirror with a sample between the two measurements. This replacement often adds to the complexity of the setup and it introduces an uncertainty in the phase shift due the positional shift between sample and mirror [5], creating a preference for transmission measurements.

Electromagnetic radiation is subject to attenuation, in an extreme case a pulse is indistinguishable from the background noise. In the case of TTDS, pulse attenuation due to absorptive materials can be lowered to an acceptable level by reducing the thickness of the sample, however, thin samples are prone to Fabry-Perot effects. For the most absorptive materials, reflection measurements are necessary.

3.2 Calculations of optical parameters

Any electromagnetic signal can be described by its Fourier spectrum, given by its Fourier transform

$$E(\omega) = \int_{-\infty}^{\infty} E(t) e^{-i\omega t} \, \mathrm{d}t. \tag{3.1}$$

In TTDS both measured signals, reference and sample, are Fourier transformed and compared through division,

$$H(\omega) = \frac{E_s(\omega)}{E_r(\omega)} = T(\omega) e^{i\phi(\omega)}. \tag{3.2}$$

Here $E_s(\omega)$ and $E_r(\omega)$ are the Fourier transformed sample and reference pulse, respectively. Where $T(\omega)$ is the amplitude and $\phi(\omega)$ is the phase. Both the amplitude and unwrapped phase of the Transfer function $H(\omega)$ for the signal in Figure 3.2 is included in Figure 3.3. A similar discussion on extraction of optical parameters from TTDS is described in [60].

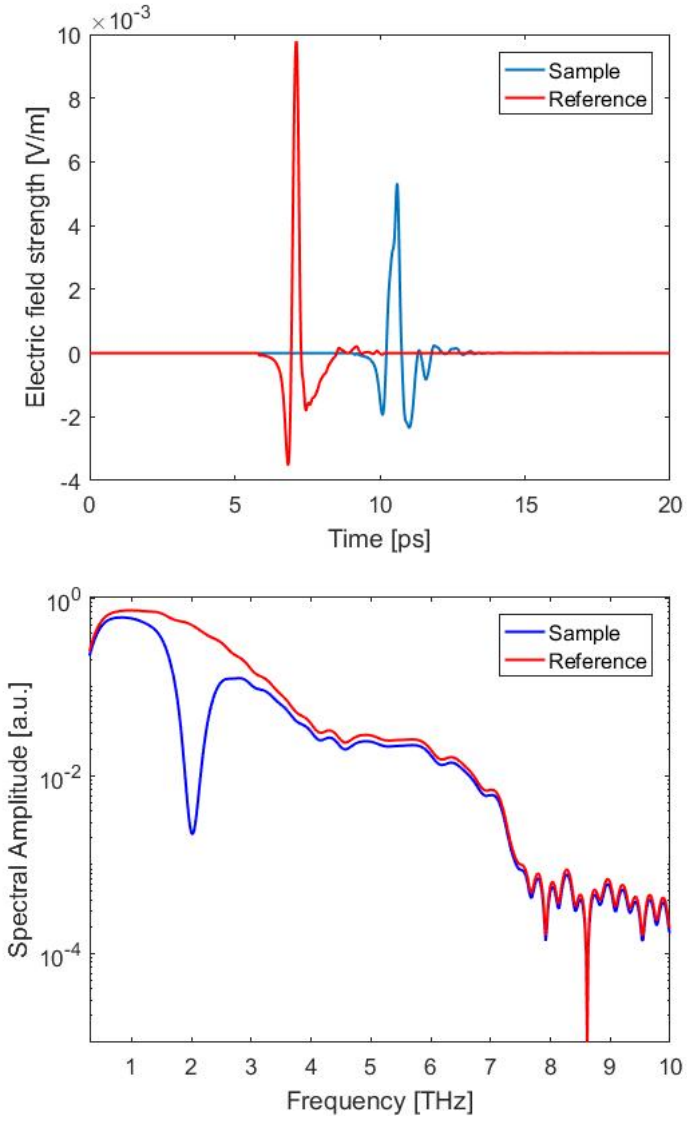

Figure 3.2: A typical TTDS time trace for sample and reference in transmission, with their corresponding Fourier-Transform. These are signals simulated with MATLAB.

3.2.1 Optically thick samples with small absorption

Considering a sample of thickness d, such that the optical thickness is large compared to the pulse width of an incoming beam at normal incidence, we can write the transfer as

$$T(\omega)e^{i\phi(\omega)} = t_{12}e^{-\kappa(\omega)\frac{\omega d}{c}}e^{i(n(\omega)-n_{air})\frac{d\omega}{c}}t_{21}. \tag{3.3}$$

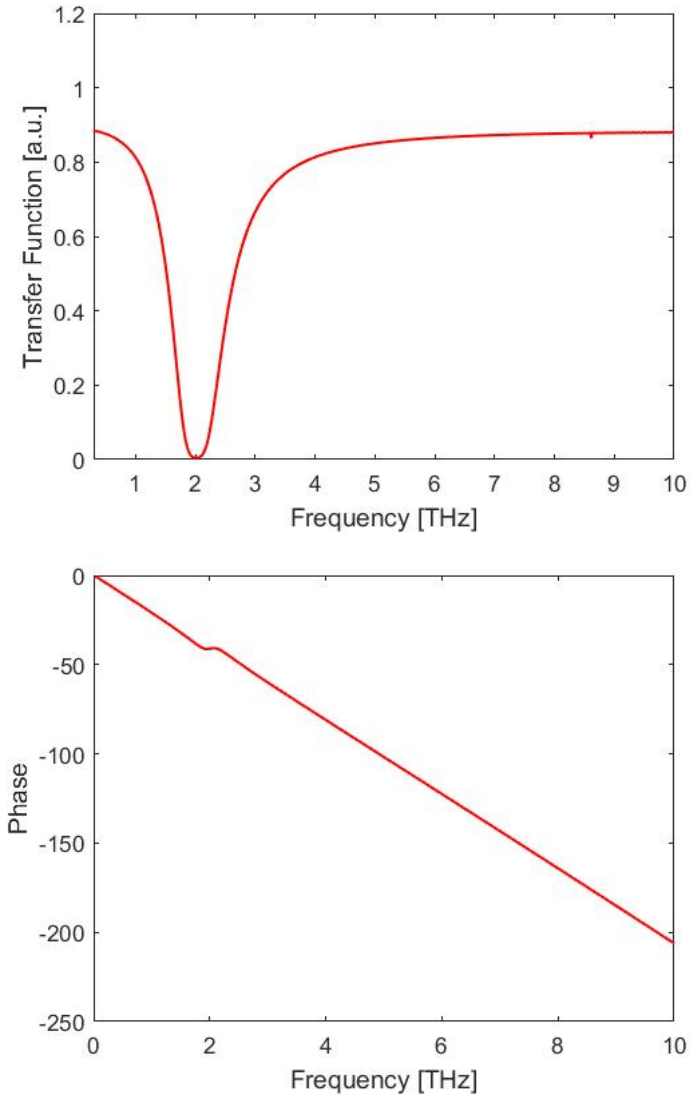

Figure 3.3: The top shows the amplitude of the transfer function, while the bottom show the unwrapped phase. Unwrapping is used as a means of removing unwanted discontinuities when the phase jumps one cycle, i.e. when the phase reach $\pm 2\pi$.

Fresnel's coefficients t_{12} and t_{21} are approximately real valued for low absorptive samples. We can solve analytically for $\kappa(\omega)$ and $n(\omega)$,

$$n(\omega) = \frac{\phi(\omega)c}{d} + n_{air} \tag{3.4}$$

$$\kappa(\omega) = -\frac{c}{\omega d}\ln[\frac{(n(\omega)+n_{air})^2}{4n(\omega)}T(\omega)]. \tag{3.5}$$

These are the simplest expressions for $n(\omega)$ and $\alpha(\omega)$ [50]. The resulting optical parameters for the simulated signals in Figure 3.2 is shown in Figure 3.4.

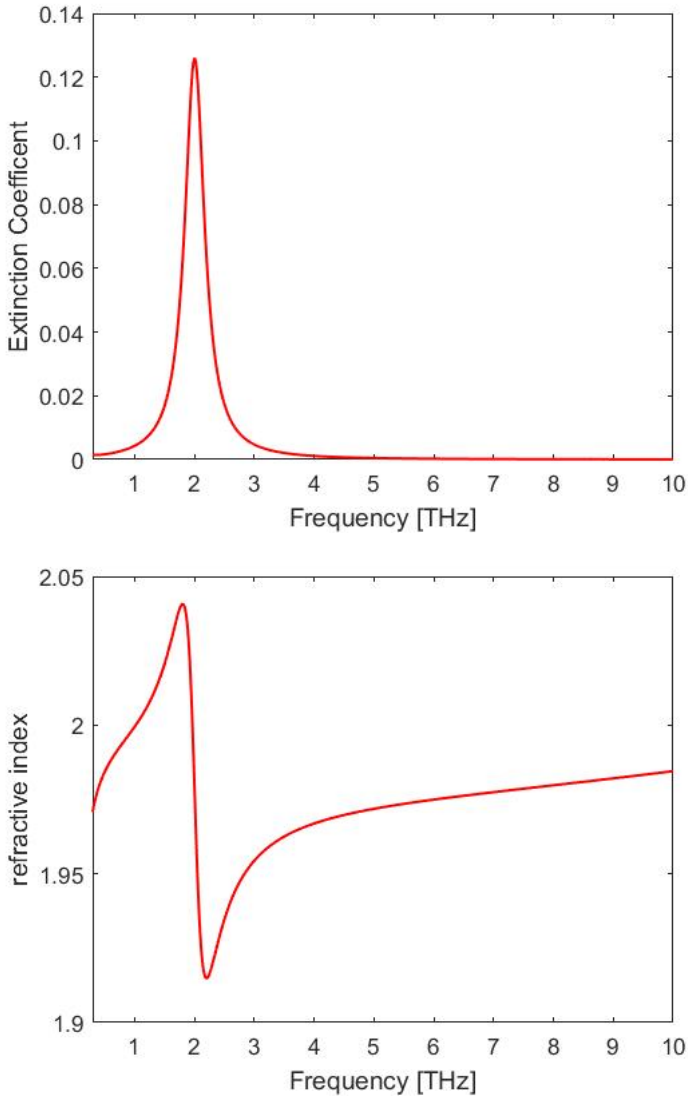

Figure 3.4: The Absorption coefficient and refractive index of the simulated sample in Figure 3.2. Calculated using equations (3.4) and (3.5). From the calculated refractive index, we can see that the simulated sample is a Lorentz medium, with the Lorentzian fixed around 2 THz.

The thickness is the biggest source of error in calculations of n and κ, which will be

discussed in section 6.1.1.

3.2.2 Samples with Absorption

Absorptive materials induce a non-negligible complex part in the transmission coefficient. As a result the formulas for extracting n and κ become non-analytical. Numerical methods , such as Fixed-point iteration, become a necessity to solve for the complex refractive index. We can represent the equations by their measurable parts and their theoretical parts as follows,

$$T(\omega) = \frac{4}{(n(\omega)+1)^2+\kappa(\omega)^2}\sqrt{n(\omega)^2+\kappa(\omega)^2}e^{-\frac{\omega}{c}\kappa(\omega)d} \tag{3.6}$$

$$\phi(\omega) = \arctan(\frac{-\kappa(\omega)}{1+n(\omega)}) + \frac{\omega}{c}(n(\omega)-1)d + \arctan(\frac{\kappa(\omega)}{\kappa(\omega)^2+n(\omega)+n(\omega)^2}). \tag{3.7}$$

A rough outline of the calculations is included in Appendix B.

3.2.3 Optically Thin samples (Fabry Perot)

In the previous sections we have extracted the complex refractive index $\hat{n}$ without considering reflection from boundaries inside the sample. This can be done when the sample's absorption and thickness will reduce the reflections or when the thickness is large enough so that for all practical purposes the Fabry-Perot effect is not observed. Fabry-Perot (FP) reflections are discussed in detail in Appendix F.2.1. The astute reader may consider limiting the time-frame of the experiment to remove any Fabry-Perot reflections. This and other methods for removing reflection in the EO-crystal in the detection scheme are discussed in section 4.5.3. These methods should in principle be applicable to the sample. Additionally, cutting the time window would have an effect on resolution of spectral features, which is discussed in section 4.2.

Thin samples are defined as samples which have optical thickness comparable to the pulse width of the beam, and for this section we assume that these samples show low enough absorption that we see Fabry-Perot reflections. A typical FP time trace and its spectrum is shown in Figure 3.5.

Apart from constraining the time window of the measurements, numerical methods have been developed to handle Fabry-Perot reflections, and were first mentioned by Duvialleret et al. [19, 20]. General considerations on numerical analysis of TTDS are included in Appendix C, and a detailed discussion can be found in [63].

The equation most often used are as following

$$H(\omega) = T(\omega)e^{i\phi(\omega)} \cdot FP(\omega), \tag{3.8}$$

where $T(\omega)$ and $\phi(\omega)$ can be the expressions shown in equations (3.6-3.7) or equation (3.3), i.e. assuming absorptive or low-absorptive material. $FP(\omega)$ is a finite variation of the summation term as proposed in Appendix F.2.1, equation (F.26).

$$FP(\omega) = \sum_{k=0}^{i}(r_{10}e^{-i\frac{n(\omega)\omega d}{c}})^{2k}. \tag{3.9}$$

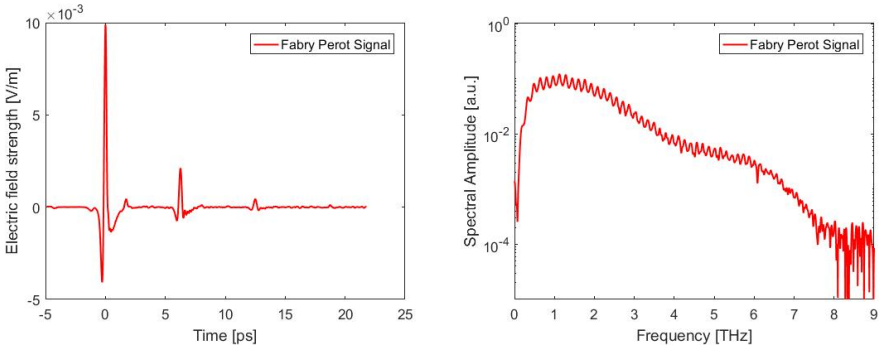

Figure 3.5: (LEFT) Fabry perot time trace from $300\mu m$ GaP (The EO-detection crystal) (RIGHT) The absolute value of the Discrete Fourier Transform of the pulse on the left.

Here r_{10} is Fresnel's reflection coefficient, and k is the k'th Fabry-Perot reflection term, whilst i is the maximum number of reflections, the case in Figure 3.5 gives $i = 2$. One possible approach to remove FP effects numerically is proposed in [60], this method is based around making a guess for n and κ, which normally is done with equations (3.4-3.5). Afterwards for each frequency a numerical method is applied to minimize the error between the measured transfer function and the analytic, see [63, 60]

3.2.4 Reflection at 45-degrees s-polarized

Calculations of the optical parameters in reflection are based on the same principles as transmission. Calculations are included in Appendix A. The final expression for n and κ for s-polarized waves in reflection at 45-degrees becomes the following

$$n(\omega) = \frac{1}{2}\frac{(1-|r|^2)^2}{(1+|r|^2-2|r|\cos(\zeta(\omega)))^2} + \frac{1}{2} \tag{3.10}$$

$$\kappa(\omega) = \frac{1}{\sqrt{2}}\frac{2|r|\sin(\zeta(\omega))}{1+|r|^2-2|r|\cos(\zeta(\omega))}\frac{1}{\sqrt{(1-\frac{1}{2n(\omega))^2})}}. \tag{3.11}$$

Here $\zeta(\omega)$ and $|r|$ are the reflection analogues of $\phi(\omega)$ and $T(\omega)$ in transmission, respectively.

A reference measurement is done with reflection of a highly reflective surface, typically a polished metal mirror. In contrast to transmission measurements, reflection measurements will not show a delayed pulse for the sample measurement. Any delay is due to the displacement between the mirror and sample, and a phase error will occur due to this. This could be circumvented to a large degree by letting the probe reflect of the same surface as the pump [5], requiring a sample surface which reflect both THz radiation and the wavelength of the probe.

Chapter 4

Experimental Methods

This chapter will present and review important aspects to the experimental setup as well as describing improvements done to it in this thesis. Section 4.1 presents the experimental setup used in this thesis. The next sections (4.2 - 4.4) describe the bandwidth and resolution, noise and the principles of lock-in amplifier. The last section 4.5, present all the improvements and studies done to understand the experimental setup better. We divide the improvements into three categories. Firstly, practical science is about the polarization, placement and beam size of the generated THz. Secondly, unexpected problems are problems that arose while continuously improving the setup. The last section is about the Fabry Perot reflections in the EO-crystal used for detection, and how one can remove them.

4.1 Experimental Setup

The experimental setup is shown as a schematic in Figure 4.1, the finished setup is shown in Figure 4.2. The setup is highly versatile, as it can be used both for reflection and transmission measurements. The change from one to the other measurement method is done by changing two flip mirrors as shown in Table 4.1 and turning the sample 45-degrees as seen in Figure.**??**.

Configuration	Reflection	Transmission
Flip mirror 1	On	Off
Flip mirror 2	Off	On

Table 4.1: Configurations of the two flip mirrors, ”On” refers to when the flip mirror is in raised position i.e. when it is reflecting the beam. Figure 4.1 shows flip mirror 1 in green and flip mirror 2 in purple.

THz is extensively absorbed in humid air. We dry air by sending air through a tube with carefully packed Drierite. The dry air is pumped into the moist air inside the sealed

box through a hose, as seen in the bottom left of Figure 4.2. We measure relative humidity with iTHX-SD from Omega, in the top left of the plexiglass box in Figure 4.2.

The schematic shown in Figure 4.1 is similar to the conceptual TTDS illustration in Figure 3.1. The THz emitter in Figure 3.1 is an analogy of the plasma, together with the BBO crystal and lens in Figure 4.1. The THz detector in Figure 3.1 is similar to the electrooptic crystal, shown as red elements together with a quarter wave plate, Wollaston prism, and an auto-balanced detector (two photo-detectors). The sampling pulse in Figure 3.1 is simply the pulse moving through the delay line in Figure 4.1.

Its superior bandwidth and lack of damage threshold makes THz generation by air filament preferred to other techniques.

The 800nm pump beam is focused by a $f = 25cm$ lens in order to generate a cold plasma. Between the generated plasma and the lens, a BBO crystal is positioned to generate 400nm (SHG) pulses, it is mounted on a translation stage to adjust the phase between the 400nm and the 800nm pump beams. Generation by air leaves strong residual 400nm and 800nm beams which are reflected by a FZHR-Silicon Spectral splitter onto a beam dump made of tightly packed razor blades.

The THz generated from the plasma is collimated by an elliptical mirror before being focused by a $f = 10cm$ elliptical mirror onto a sample placed in the focal point. The beam, given that the setup is in transmission mode, is then collimated by an identical elliptical mirror equally distanced on the other side of the sample. The THz beam is focused upon a GaP crystal where the 800nm probe, that has traveled through a delay line, interacts with the THz. In reflection mode the GaP is mounted close to the sample, reducing the need for a focusing element [5].

FSEOS is used as the detection scheme; GaP was chosen due to better bandwidth than most other electrooptic crystals. Dispersion in the EO-crystal and mismatch between optical and THz phase velocities limit the spectrum of the pulse (see section 4.5.2). Moreover, there is a trade-off between sensitivity and bandwidth. Velocity mismatch is proportional to the thickness of the crystal and will restrict the total bandwidth of the detector. On the other hand, the thickness is linearly proportional to the interaction length inside the EO-crystal, such that the sensitivity of FSEOS is proportional to the thickness of the EO-crystal [39]. Based on the arguments in this paragraph and [8], $300\mu m$ GaP thickness was deemed a good choice. However, as can be seen in section 4.5.3, a thickness in this range creates multiple reflections (Fabry-Perot) from both THz and optical beams inside the GaP crystal, which creates distortions in the calculations of the optical parameters.

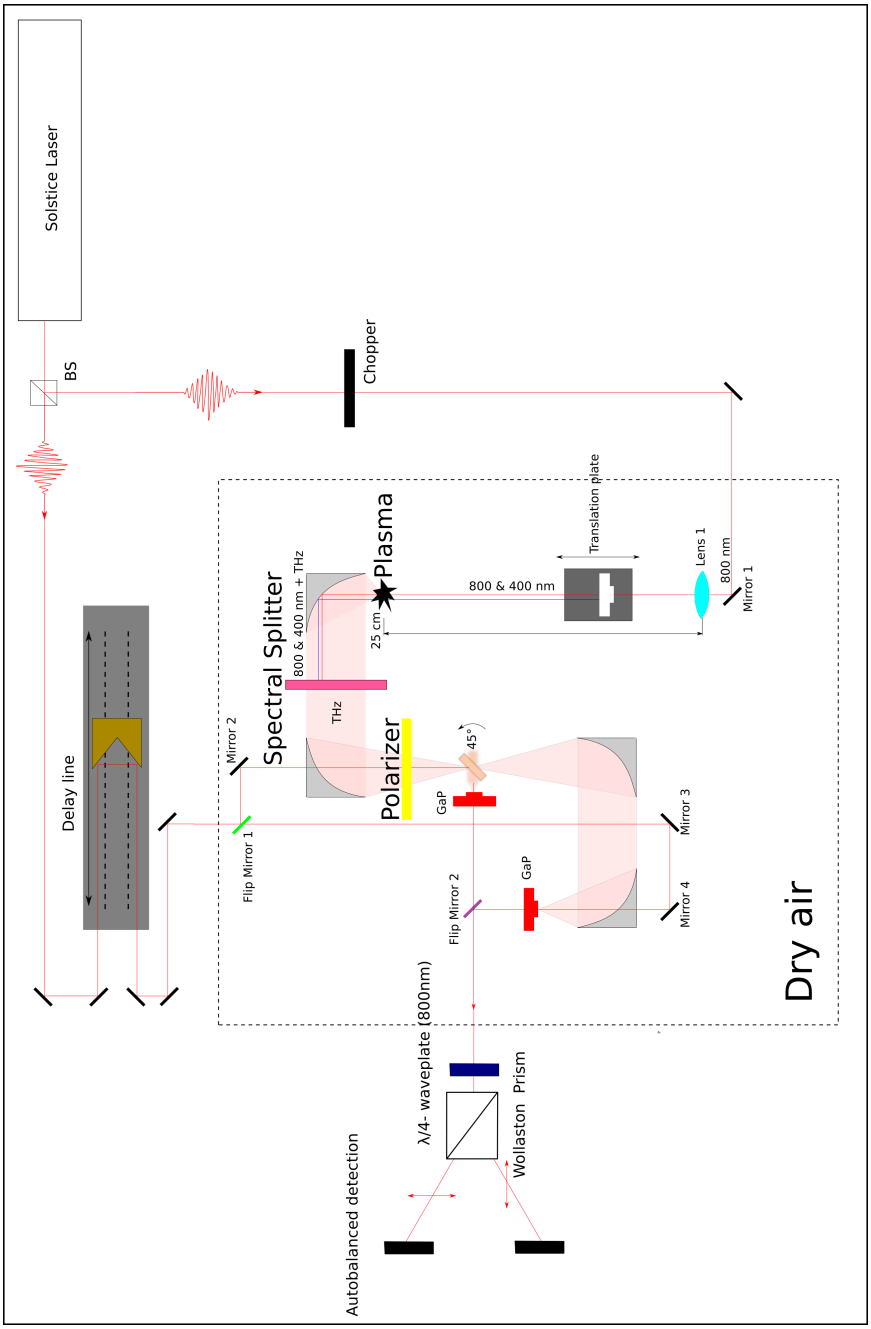

Figure 4.1: Schematic of the experimental setup.

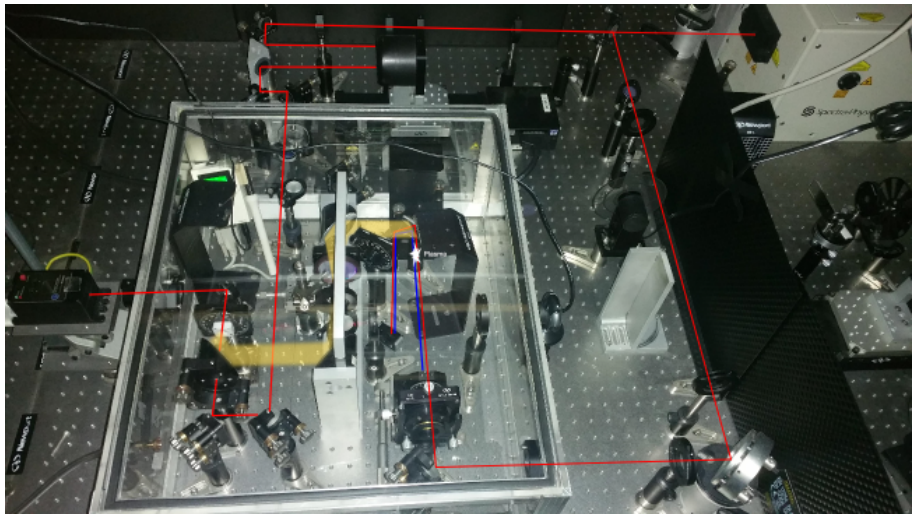

Figure 4.2: Picture of the finished setup in transmission mode. Red line is 795 nm laser light, blue is the second harmonic wave generated inside the BBO-crystal. The yellow transparent and blurred light is the THz radiation. The small white shape is the plasma. Note that the red and blue light is reflected onto the beam dump.

As can be seen in Figures 4.2 and 4.1 holes are drilled on the backside of each elliptical mirror in order to let probe light through. To create a temporal overlap between the probe and pump beam, both beams have to travel the same distance before hitting the GaP crystal. Measurements of the outlined optical path length from the point where probe and pump splits up were done with a ruler, measurements are included in Table 4.2

OPL	Transmission	Reflection
Pump	202 cm	180.75 cm
Probe	202 cm	180.75 cm

Table 4.2: Optical path length (OPL) from first beam splitter until hitting the electro-optic crystal for pump and probe beam. Measurements done while the translation stage was in equilibrium.

The data acquisition is done in MATLAB. Firstly one has to connect both the Lock-in Amplifier(see section 4.4) and the delay line motor to a computer. Next, choosing incremental step length, scan length and scan start is done in MATLAB. The delay line is set to 0 in the middle of the delay line, a raw data file plot from one of the channels on the Lock-in Amplifier is shown in Figure 4.3.

We see from Figure 4.3 that the probe and pump do not overlap in the middle of the translation stage. As the probe beam travels back and forth in the delay line, one observes a total difference of 1.8 cm. The discrepancy is primarily due to dispersion in the optical elements, which is hard to account for. Converting translation stage position to time is done by the following formula,

$$t = \frac{2x}{c}. \tag{4.1}$$

Where x is the placement on the translation stage, and c is the speed of light in vacuum. The factor 2 comes from that the beam moves double the distance of the translation stage. By inverting the time axis, including both channels from the lock-in, and setting the $t = 0$ underneath the biggest peak, we attain a signal as shown in Figure 4.4. The arrows in Figure 4.4 show two different types of artifacts in the setup. The white background arrows show reflections inside the GaP crystal (see section 4.5.3) which impose a resolution limit as explained in section 4.2. The arrows with black background show reflections inside the spectral splitter, these are not discussed in detail throughout the thesis, but the outcome of these are similar to the GaP reflections, i.e. distortions in the final calculations and constraints on the resolution in the Fourier spectrum.

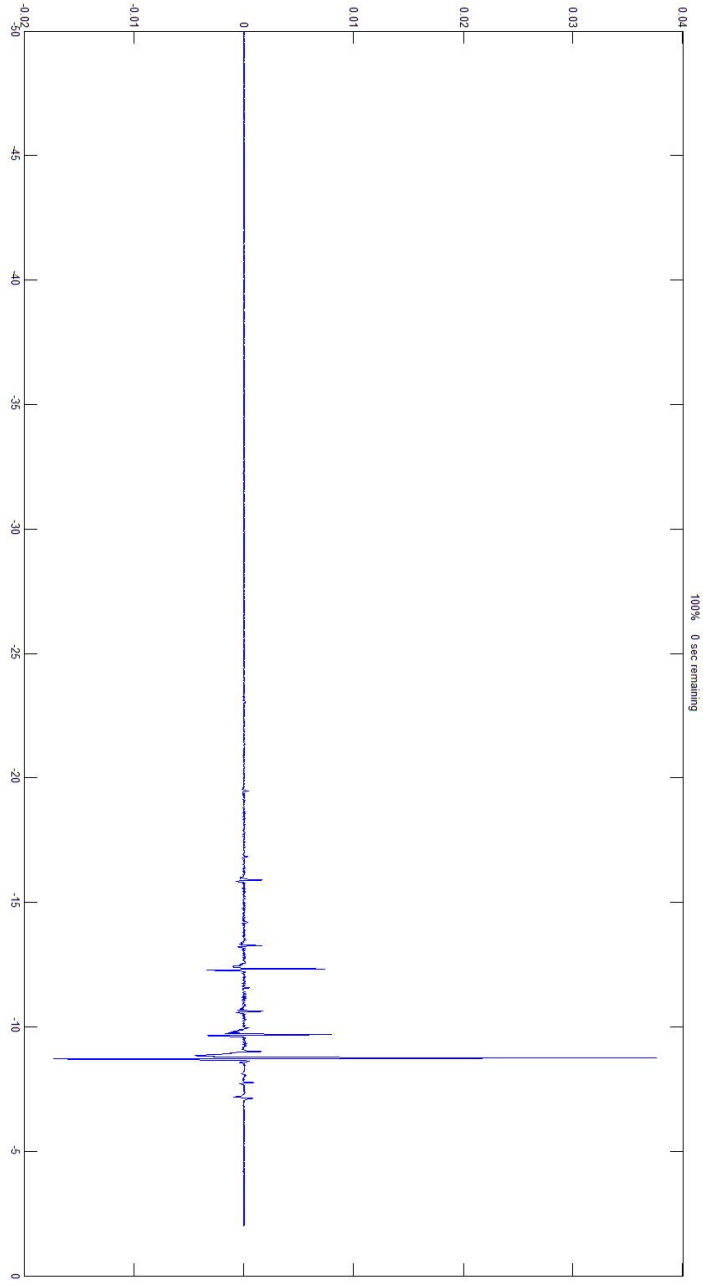

Figure 4.3: A raw data plot in transmission mode in air. The Y-axis shows the electric field strength, the x-axis is the delay line placement in mm with 0 as the middle of the translation stage. The negative X direction on the translation stage, corresponds to a smaller OPL for the IR-probe.

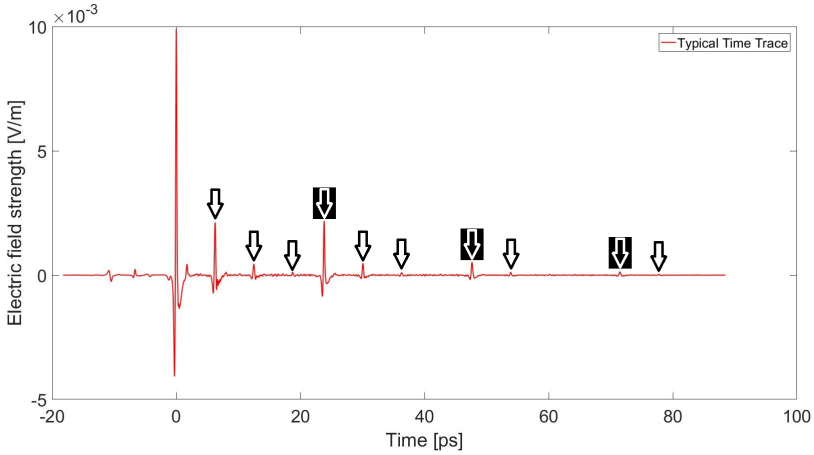

Figure 4.4: A typical time domain trace attained from the Setup with explanatory arrows. The black bordered arrows show multiple reflections inside the GaP crystal, and the black background arrows show multiple reflections inside the spectral splitter. The Gap crystal show multiple reflections from the reflections inside the spectral splitter, creating pulse trains. The reducing number of GaP reflections are a result of weaker signals as they are reflected back and forth inside the spectral splitter.

4.2 Resolution and Bandwidth

The fundamental relationship between pulse width and bandwidth is used in time-resolved spectroscopy, in this thesis, short pulses with broad bandwidths are directed through materials to identify their spectral signatures. For clarity, bandwidth and resolution will be discussed in two parts. The first part is the physical limits on the bandwidth, which is due to the host material of the laser gain medium. The second part will focus on the delay line and its settings. Briefly, the inversely proportional relationship between frequency and time in a Fourier Transform relates directly to the bandwidth and resolution of the detected THz signal. That, in turn, leads to the delay line settings being meaningful in the discussion on calculations of n and κ.

The laser system used in this thesis is Solstice One-Box Ultrafast Amplifier [53]. The system consists of a regenerative amplifier, a stretcher/compressor stage, a seed and a pump laser. Solstice delivers 72fs $sech^2$ pulses with an average power of 3.2W. Measured spectra of the seed laser pulse (MaiTai) and the Solstice pulse is shown in Figure 4.5, normalized to their respective measured peak power.

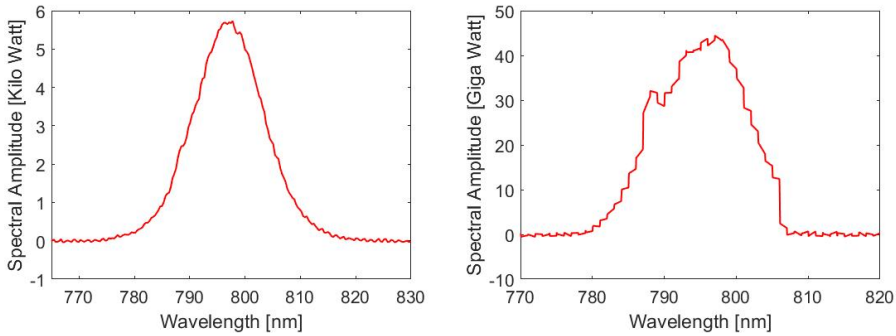

Figure 4.5: Two spectra from the Solstice laser amplification system, measured with a spectrometer and normalized to its peak power. (LEFT) MaiTai (RIGHT) Solstice

The pulse from the Solstice is used for generating and detecting THz radiation in this setup. The keen reader may appreciate that the complex process in the plasma that generates THz presents convoluted behavior between the spectrum of the Solstice pulse and the achieved bandwidth of THz. Ignoring this, we make an approximation that the FWHM of the solstice pulse is the only part of the pulse that generates detectable THz. Furthermore, we assume that the THz is directly proportional to the amplitude of each spectral component and we can present a direct relationship between the two, as follows

$$\Delta f = \frac{c}{\lambda_0^2}\Delta\lambda. \tag{4.2}$$

Here Δf is the bandwidth of the generated THz-radiation, c is the speed of light in vacuum, λ_0 is the central wavelength of the Solstice pulse and $\Delta\lambda$ is the FWHM of the Solstice spectrum. Using values from Figure 4.5, an estimate of the final THz pulse band-

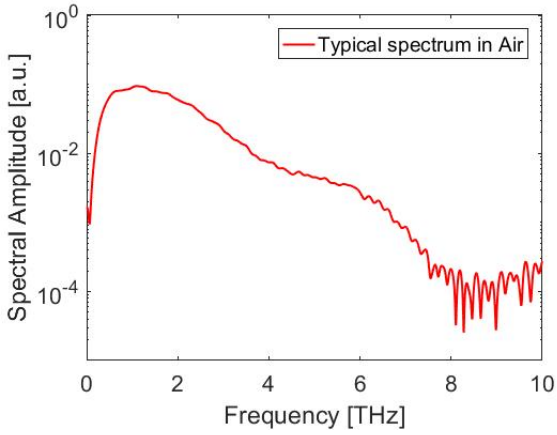

Figure 4.6: Typical spectrum of a THz-pulse in Air

width is attained

$$\frac{3 \cdot 10^8 m/s}{(798nm)^2} \cdot 17nm = 8THz. \tag{4.3}$$

A delay stage is used to resolve the signal in time. It is a retroreflector mounted on an IMS-LM from Newport, as seen at the top of Figure 4.2. The probe is delayed relative to the pump when this translation stage moves. IMS-LM has a minimum incremental motion of $0.02\mu m$, the probe beam itself will move twice this distance at each increment, yielding $0.04\mu m$. The total movement of the delay line is 100mm (200mm for the beam).

The choice of both incremental motion length (step length) and the total distance of the scan (scan length) is important for the attainable Fourier spectrum, and its resolution. The inverse relationships between time and frequency in a Fourier transform explains the behavior,

$$\Delta t_{steplength} = \frac{1}{\Delta f_{bandwidth}} \tag{4.4}$$

$$\Delta t_{scanlength} = \frac{1}{\Delta f_{resolution}}. \tag{4.5}$$

Regarding resolution limits, the Solstice has an uncertainty of around 6 GHz, which is the absolute limit for the measured spectrum. Concerning bandwidth of the FFT, the absolute limit is unknown and is in this thesis believed to be far greater than the bandwidth of the generated THz.

The bandwidth of the FFT spectrum should at least correspond to the bandwidth of the generated THz pulse. Also, one has to consider aliasing effects (Nyquist's theorem). Moreover, a total bandwidth of 20THz in the FFT is sufficient for this particular setup. From equation (4.4), this corresponds to a step length of $3.75\mu m$ ($\Delta t_{steplength} = 12.5fs$). One could argue that the probe's pulse-width (around 72fs), would limit the step length on the translation stage, and on some level, this must be true. On the other hand, the nonlinear

interaction in the EO-crystal relieves the wings of the probe pulse from any interaction, and that the limit is smaller than FWHM of the proposed 72fs probe pulse. Going beneath such a limit would yield a distorted time and frequency profile from the final signal, but from the multiple time and frequency traces seen in this thesis a hand waving argument is made that we are not crossing such a limit.

Analyzing smaller spectral features increases the scan length, but some considerations are limiting the resolution, summarized in a list below.

- The actual time each scan takes (see Scan time section 4.5.2)
- Multiple reflections from the GaP distorts the calculated refractive index(see section 4.5.3)
- Distortion of the optical parameters due to FP effects from the spectral splitter. (see Figure 4.4).

4.3 Noise, Dynamic range and Signal-to-Noise Ratio

Many sources are contributing to the noise in our setup. As long as these sources are uncorrelated and additive, averaging over multiple runs will lower the contribution of noise in the signal. This section treats all additive noise, while in section 4.5.2 we introduce correlated noise related to this setup.

The quality of a signal is measured with respect to the noise floor, leading to multiple figure of merits. The most used are Signal-to-Noise ratio (SNR), which is the ratio between the signal and the level of noise. And Dynamic Range (DR) which is the ratio between the largest and smallest value measured. From [45] we calculate them,

$$SNR = \frac{\text{mean magnitude of amplitude}}{\text{standard deviation of amplitude}} \tag{4.6}$$

$$DR = \frac{\text{maximum magnitude of amplitude}}{\text{RMS of noise floor}} \tag{4.7}$$

Here RMS is the root mean square. SNR indicates the minimal signal change detectable, while DR shows the maximum perceptible signal change. All calculations of DR and SNR in this thesis are based on the enumerated list below [45].

1. Measure the time-domain trace and note the value of the peak maximum.
2. Measure the noise signal in the absence of THz, e.g., before the arrival of the main pulse.
3. The mean signal in the absence of THz should be constant (zero for electro-optic detection, nonzero for a photo conductive antenna). Calculate its standard deviation.
4. DR=mean peak/SD of noise
5. SNR=mean peak/SD of peak

In this thesis, the noise is calculated from the first 50 data points, thus the time window should be chosen accordingly, i.e. no signal of interest should be present in the first 50 data points.

Uhd-Jepsen demonstrated that the highest absorbance one can measure is limited by the dynamic range of the experiment, and corresponds to the noise floor of the experiment [28]. This figure of merit can be written as,

$$(\alpha d)_{max} = 2\ln(DR\frac{4n}{(n+1)^2}), \tag{4.8}$$

where DR is the dynamic range of the measurement. As the THz radiation in a reflection measurement is reflected of the surface, it can be used to characterize materials which normally are limited by $(\alpha d)_{max}$. If the absorption is so great that the signal is obscured by noise, the absorption coefficient becomes $\alpha = \alpha_{max}$ [50], i.e. we can only measure an absorption $\alpha < \alpha_{max}$.

4.4 Lock-in Amplifier

A lock-in amplifier (LIA) is an instrument which substantially improves SNR. The LIA is connected to a modulation reference, in our case a chopper, and the detected signal. A phase locked loop and a phase sensitive detector (PSD) is used to multiply the detected signal and the reference signal together [2, 27]. We can write the output from the LIA as

$$V_{LIA} = LP[V_{psd}] = \frac{1}{2}V_{sigl}V_{ref}LP[\cos(\omega_{sig} - \omega_{ref}t + \phi_{sig} - \phi_{ref}) - \cos(\omega_{sig} + \omega_{ref}t + \phi_{sig} + \phi_{ref}]. \tag{4.9}$$

Here LP denotes a low-pass filter, ω_{ref}, ϕ_{ref} and ω_{sig}, ϕ_{sig} is the angular frequency and phase of the reference and detected signal, respectively. Due to the low-pass filter, we usually have the case where $V_{LIA} = 0$, however when $\omega_{ref} = \omega_{sig}$ we have the following

$$V_{LIA} = \frac{1}{2}V_{sigl}V_{ref}\cos(\phi_{sig} - \phi_{ref})). \tag{4.10}$$

Note that for $\phi_{sig} - \phi_{ref} = \pi/2$ we have no output signal from the LIA, this can be fixed by adding another reference pulse with a phase shift of $\phi_{ref2} = \phi_{ref} + \pi/2$, as follows

$$V_{LIA2} = \frac{1}{2}V_{sigl}V_{ref}\sin(\phi_{sig} - \phi_{ref})). \tag{4.11}$$

These are both DC-signals, carrying the magnitude of the signal. Where we can extract the V_{sig} by the following formula

$$V_{sig} = (V_{LIA}^2 + V_{LIA2}^2)^{1/2} \tag{4.12}$$

The PSD in combination with the low pass filter only measures the signals whose frequencies are close to the lock-in reference frequency. Noise signals are attenuated as long as they are far from the reference frequency. Noise with a frequency close to the reference may come out as low-frequency AC signals.

4.5 Improvement to the experimental setup

Throughout the thesis work, as the setup was continuously improved, new problems emerged. In this section, we discuss, all improvements made to the system as part of this thesis. We address three main topics; practical science, unexpected problems and the Fabry-Perot effect from the GaP crystal. Except for the latter section, each subsection is made up of smaller specific topics that sometimes are completely unrelated.

4.5.1 Practical Science

Locating the THz beam

This segment introduces a novel method for locating the THz spot. Its invisibility is one of the biggest challenges while working with THz radiation. Moreover, the low energy of THz photons removes the possibility of using luminescent cards. The IR pump worked like a pinpointer for the THz spot location while building the setup. Sadly, this is not a permanent solution, as it requires the removal of optical components, such as the spectral splitter, BBO crystal, and THz polarizer.

The region where locating the THz beam is most pressing is close to the sample. We sought a method to locate the THz spot to know where one should put the sample. Without having to introduce an optical attenuator and remove optical elements. This was done using a flip-mirror and two pinholes, as shown on the left in Figure 4.8. The two pinholes work as a crosshair, that always aims at the same position. Calibration of the crosshair is done by introducing a pinhole, mounted on a translation stage, on the other side of the sample, as shown to the right in Figure 4.8. The steps for localizing the beam are summarized below,

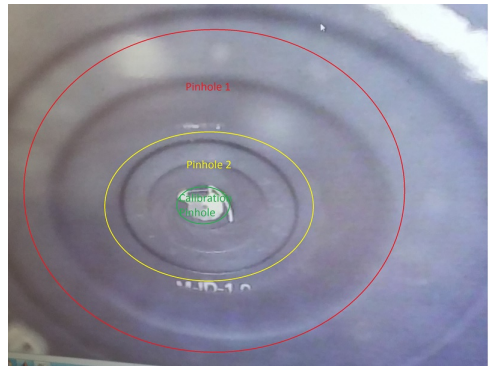

Figure 4.7: Image taken from the web camera while aiming the pinholes towards the THz radiation. The red circle shows the pinhole closest to the camera, the yellow shows the second pinhole, and the green is the small pinhole seen in Figure 4.8.

- The probe is delayed to the maximum value of the THz radiation. Such that we are at all times recording the peak value of the THz radiation on the lock-in amplifier.

- The small pinhole (right of Figure 4.8) is introduced, and moved around until the maximum is found.
- The two pinholes are aimed onto the found maximum point, as can be seen in Figure 4.7.
- The small pinhole is removed.

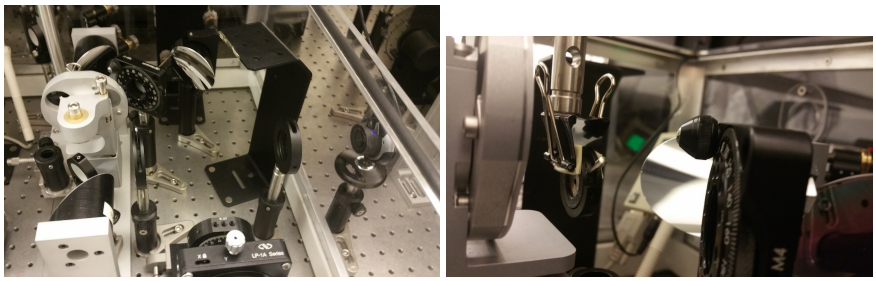

Figure 4.8: (LEFT) The crosshair. (RIGHT) The calibration pinhole introduced on the other side of the sample holder.

When the calibration is done, we can place the sample and look through the web camera, as seen in Figure 4.7. If the sample is seen through the two pinholes (in the green circle in Figure 4.7), we are convinced that most of the THz are going through the sample.

To sum up, the crosshair made the process quicker when samples had to be introduced, as one could easily put the sample at the correct place.

Beam size and sample size

The following section discusses the relationship between the spot size and the sample size. As mentioned in the preceding section, invisibility is a practical challenge in THz science. The crosshair made it easier to position the spot in space, and additionally making it simpler to install the sample in front of the THz radiation. However, errors in the calculations of n and κ is an issue if the THz Spot size is bigger than the sample.

An easy way of knowing if the beam was completely hitting the sample, is to compare the reference and sample measurement time traces. If any signal is present in the sample measurement at the same place as the main peak for the reference measurement, there must be some THz that propagates through the setup without hitting the sample (see Figure 4.9).

The crosshair made sure that most of the THz radiation was going through the sample. By introducing a pinhole behind the sample, one can make sure that all THz radiation detected at the end is going through the sample. The idea now is that when doing any measurement, we first introduce the sample, and run one quick scan. From the scan we find at what position the translation stage is when we record the maximum value of THz. Now, we move the translation stage to this position. We reduce the pinhole size until we have decreased the peak value about $5 - 10\%$. By doing so, we limit the signal to that which propagates through the sample. By leaving the aperture size untouched for the reference measurement, we compare the same portion of the beam in both analyses. This

method will for smaller sample reduce the peak value. Thus different measurements of the aperture size and value of the THz peak was conducted, see Table 4.3.

Pinhole diameter[mm]	Percentage of Peak Amplitude [%]
1.75	16
3.15	35
4.73	49
10.05	73
24.85	100

Table 4.3: The size of the pinhole and the measured peak amplitude. The measurements were conducted with a relative humidity around 30% and sub-optimal alignment of the whole setup.

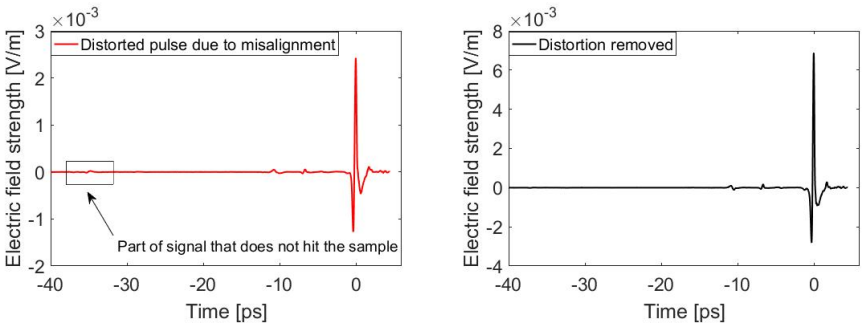

Figure 4.9: (LEFT) The time domain trace of radiation that is partly hitting the sample. (RIGHT) The same trace after the pinhole size and sample position have been adjusted. The bigger peak value is mostly due to re-positioning of pinhole and sample, it is a proof of bad alignment on the left picture.

The pinhole method is independent of whether or not we are focused before or after the sample, as it will remove any signal that does not hit the sample. Based on our measurements, we believe that we are focused before the pinhole, as the pinhole tend to be bigger than the sample before the peak value starts to drop. With this in mind, a measurement of the beam size in the estimated focus point was conducted. The sample was changed to a pinhole, and measurements of the peak value was conducted as can bee seen in Table 4.4.

Pinhole diameter	Percentage of Peak Amplitude
1.70 mm	61.7%
2.69 mm	73.53%
3.89 mm	86.76%
4.68 mm	95.58%
24.85 mm	100.0%

Table 4.4: The size of the pinhole and the measured peak amplitude. The measurements were conducted with a relative humidity around 36% and sub-optimal alignment of the whole setup.

Disregarding diffraction, we are convinced that samples down to the size of 1.70mm can be used in the current configuration of the setup. The location of the precise focus along the propagation axis have not been investigated thoroughly.

THz-Polarizer

As a means of studying the effect of polarization and potentially improving the setup, we introduced a polyethylene THz-polarizer from TYDEX into the setup. We positioned the polarizer between the first focusing elliptical mirror and the sample position. Note that a THz polarizer is not necessary to determine the polarization of the THz beam [54, 17].

Before moving onto the measurements, some important aspects should be noted. The literature states that in a single color plasma, the THz-polarization is perpendicular to the initial IR-pump pulse, theoretically and experimentally verified in [77] and [43], respectively. However, we use a two color plasma; the BBO-crystal generates a second harmonic wave with the polarization along its extraordinary axis. The extraordinary wave interacts with the fundamental wave in the plasma, and the relative angle is of importance[17]. Throughout these measurements the BBO crystal is kept at a fixed angle. Moreover, the THz radiates as a superposition of Gauss-Laguerre modes [58], however, we assume single mode Gaussian propagation. Typically, authors report elliptically polarized THz-beams with plasma generation [17, 12].

For an arbitrarily polarized beam, one can align measurements along the weak and strong axis of the polarization, and map it onto an ellipse, as seen in Appendix F.1. In our setup, the relative angle between THz and IR-probe change the efficiency of detection in the EO-crystal, see equation (4.13)[54]. This equation is a more generalized form of equation (2.90). The angle θ is the angle between the IR-probe and the c-axis of a $\bar{4}3m$-crystal, whereas α is the angle between the THz pump and the c-axis.

$$I = I_y - I_x = I_0 \Delta\phi = \frac{I_0 \omega r_{41}}{2c} n_O^3 (cos(\alpha) sin(2\theta) + 2sin(\alpha) cos(2\theta)) \tag{4.13}$$

What we learn from equation (4.13) is that the relative efficiency of detection is a function of relative polarization of the probe and THz field and the azimuthal angle of the GaP-crystal. The efficiency is maximized when the relative angle between pump and probe is either 0 or 90 degrees. This can best be seen from the bottom and top sinusodial graphs in Figure 4.10. The azimuthal rotation is shown with three numerated pictures and their corresponding points on the graph, the blue and red axis are shown for clarification of the rotation. The efficiency dependence on angle is an important aspect to this polarization discussion.

To check if our setup obeyed the behavior proposed in [54], we conducted a series of measurements without the THz polarizer in place. These are shown in Table 4.5, the values were recorded from the lock-in amplifier while positioned the peak value and rounded to the closest integer.

Run nr.	1	2	3	4	5	6
Azimuthal angle [Deg]	90	30	330	270	210	150
Rounded peak amp. [mV]	6	-3	3	-6	3	-3

Table 4.5: Recorded peak values for different angles of the EO-crystal. Recorded from the lock-in amplifier while positioned on the peak value.

The red numbers in the figure correspond to the run number in the table. According

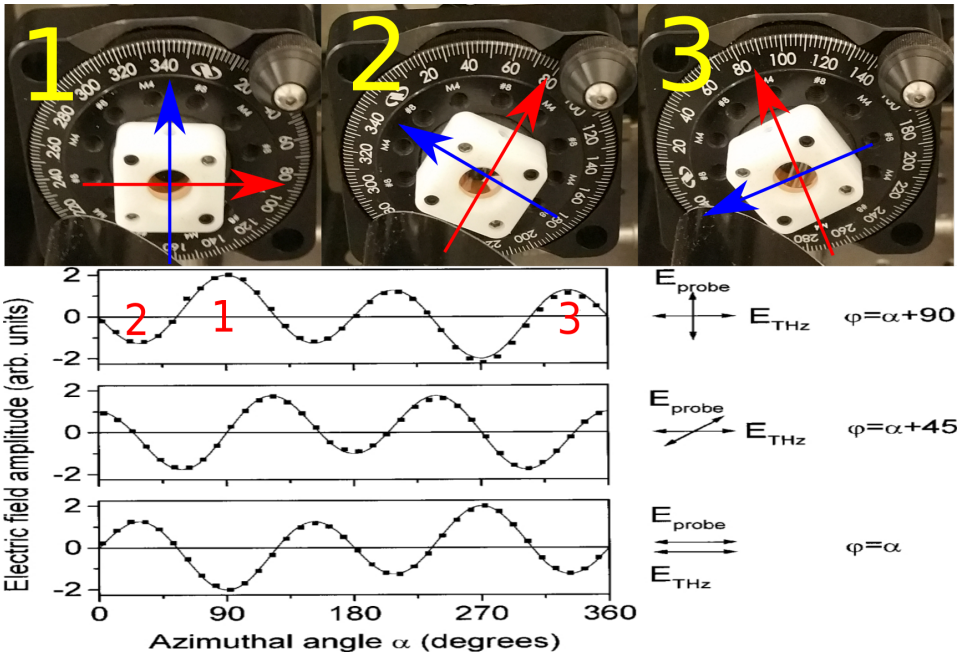

Figure 4.10: (TOP) Rotation of the GaP (EO-crystal) used in this setup. The blue and red arrows are to clarify the rotation. (BOTTOM) Graph corresponding to equation (4.13) from [54].

to specifications, the Solstice laser system delivers IR light polarized parallel to the table. The behavior proposed for a paralell or perpendicular relationship between IR-probe and THz pump polarization in [54] work is similar to what we're experimentally observing in this setup.

Next, we inserted the wire-grid polarizer to find in which axis the polarization is strongest. From the results, we observe that most of the THz is indeed in the perpendicular direction with regards to the table. The interested reader may notice that this is perpendicular to the IR-pump/probe and at an angle with the second harmonic wave. The latter is situated at approx. 55-degrees to the fundamental wave (optical table), in accordance with [33]. Note that the wire grid polarizer is not completely perpendicular, but at a very small angle. This might indicate a small dependence on SH-wave polarization direction as compared with the case for no second harmonic wave [77, 43]. We did the same checkup with the polarizer in perpendicular position as we did for no polarizer, and the work of [54] still held true, i.e. we experienced two maxima and four saddle points at the same orientations that we saw in Figure 4.10.

Most work done on polarization of THz from plasma filament show an elliptical polarization. Thus, the elliptical polarization should be expected for this setup [17, 12]. To verify this we can measure the weak axis of a proposed elliptical polarization by turning the polarizer. This is done with the caveat that the THz polarization is now parallel to the IR-probe polarization. The peak-to-peak values of perpendicular polarization,horizontal polarization (w.r.t the table) and no polarization experiments are shown in Table 4.6.

No polarizer [mV]	Perpendicular [mV]	Horizontal [mV]
6.6430	6.5640	0.1858

Table 4.6: The three recorded peak-to-peak values for, from the left, no polarizer, perpendicular oriented polarizer and horizontal oriented polarizer.

In principle the values measured with the polarizator grids oriented horizontal and perpendicular constitute the weak and strong axis of a proposedely elliptical polarization (as seen in Appendix F.1). However, the control procedure was done as the polarizer was oriented along the weak axis of the proposed elliptical polarization. The behavior changed from the last two measurements, now a maxima was observed for rotation angles that were saddle points for polarization perpendicular to the table and with no polarizator in the setup. This is typically expected when the probe is not parallel or perpendicular with the THz polarization (see Figure 4.13). This behavior have not been addressed but it may be related to a complex change of polarization, focusing of THz at GaP or the polarizator being imperfect. We chose to use the polarizer in the position that gave the best peak value, as that would give a better dynamic range. This position is perpendicular w.r.t the optical table for this setup.

We compared the spectra from the two measurements consisting of 300ms time constant, 50mV sensitivity and 24dB/Oct on the lock-in amplifier with a time window of 6ps + padding (see section 4.5.3). And we see no downside of using the polarizator. The spectrum rolls off quicker for the higher frequency, but the frequency above 7 THz are usually too small to be used for spectroscopic analysis. In addition, it seems to be a smoother spectrum from 5-6 THz, however it could be related to the time window.

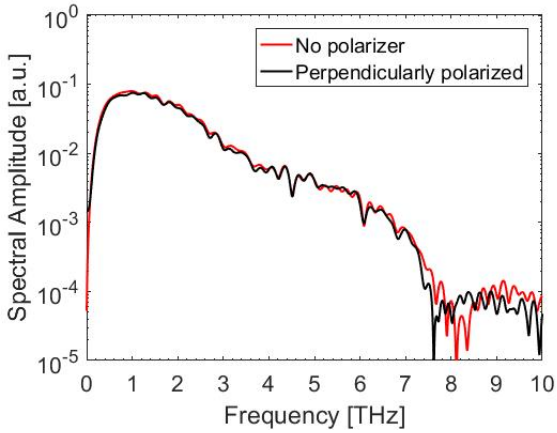

Figure 4.11: The two spectra recorded, one with (red) and one without(blue) polarizer. The scans were conducted on 50 mV sensitivity on the Lock-in, $100ms$ time constant over 5 runs.

In conclusion, by comparison with the works of Planken [54] we saw that our THz polarization is strongly polarized in the perpendicular direction of the fundamental IR-pump. By introducing the polarizer, we saw no drastic change in the spectrum. There seems to be neglible negative effects, and we left the polarizator in as a way of knowing our polarization.

4.5.2 Unexpected problems

Scan time

Next, we consider the work done to optimize the scan time versus the dynamic range of the time domain trace. The incremental step length, scan length and time constant on the lock-in amplifier are all connected to the dynamic range, resolution, and signal to noise ratio of this time-resolved measurement method. If one average out the noise with multiple runs, SNR and DR increase. If step length decrease and the scan length increase, the resolution, and bandwidth of the attained signal is increased (as discussed in section 4.2). An increase in bandwidth and resolution is then associated with a longer scan time, i.e., there is a trade-off between the time it takes to conduct an experiment and the characteristics above.

The lock-in amplifier has a time constant, which is the integration time for each data point, with a range from microseconds to seconds. Changing the time constant is the same as changing the number of averages for each data point as the translation stage is still. The difference between $1s$ and $1ms$ is then 1000 averages per data point. The program computed for this particular setup allows multiple scans, i.e. one can conduct a scan n times to remove any noise. In each scan, there is a set number of data points and a set incremental step length. Multiplying these gives the total scan length. For this study, the number of data points and incremental step length were kept constant at 3000 and $0.00375mm$, respectively.

Next, we assumed that with a time constant of $1s$ and 60 data points one scan should

take no more than 1 minute. Furthermore, setting the time constants to $10ms$ with 60 data points, 100 scans should also take no more than 1 minute. Which be formulated as in the equation below,

$$timeconstant \cdot \#datapoints \cdot \#scans = scantime \tag{4.14}$$

In order to find the optimum method, we compared the DR and scan times of runs with different parameters.The final dynamic range is calculated for the averaged signal from all scans in one measurement. The study was conducted in air and is included in Table 4.7. Except for the last measurement, the dynamic range and scan time of the study should not vary much, as the total number of averages should be equal for these cases.

Time	Number of scans	Time constant	DR	Relative Humidity (RH)
15 min	30	10ms	2212	6.6%
7.5 min	10	30ms	2442	5.3%
5 min	3	100ms	2574	5%
4 min	1	300ms	2688	4.9%
12 min	1	1s	3255	4.8%

Table 4.7: The time of each scan to the left, number of scans conducted with its respective time constant, calculated dynamic range and the relative humidity of the measurement.

The study shows that the number of scans significantly increase the time spent on one measurement, which was not as expected. We believe that. because the translation stage has to do n-fold more incremental steps for n scans the time increase substantially. Also, the number of total data points increases as the number of scans increased, thus for n scans the number of data points sent from LIA to computer increase n-fold, which can contribute to the scan time increase. The MATLAB code itself can also contribute to the growing time, as it saves each scan before averaging them at the end.

The next part shows an increase in the dynamic range as time constant increase and relative humidity decrease. The latter seems plausible, as lower humidity decrease the absorption of THz in the humid air, thus increasing the amount of signal relative to the noise. We assume a linear relationship between dynamic range and relative humidity between 6.6 to 4.8 % , and create a mathematical expression.

$$DR \cdot RH = X \tag{4.15}$$

Here X is the slope of DR vs inverse RH. Plotting X in a table for the 5 dynamic ranges and its relative humidity , as seen in Table 4.8, gives an indication that the humidity of air is not the reason for increased DR. The trend shows that X is decreasing as RH is increasing, which seems unlikely. Thus it seems likely that the change in DR in Table 4.7 is mostly from the number of scans and the integration time.

From this study, one can be led to believe that multiple runs are beneficial for the Dynamic Range. On the other hand, as the number of runs increase, the total time of one experiment increases to a prohibitive length. Consequently, we surmised that one scan with significant integration time ($3s$) was best.

DR-RH	2212 - 6.6%	2442 - 5.3%	2574 - 5%	2688 - 4.9%	3255 - 4.8%
X	146	129	129	132	156

Table 4.8: Dynamic range and Room humidity at the top. The parameter X at the bottom calculated from equation (4.15)

We used the long integration time for some experiment. However after conducting multiple scans on different samples with this long integration time method, the experiments had to be rethought. The noise contribution from small misplacement or uncertainty in the delay line is not averaged out. Causing errors in the calculated n and κ. Thus for the proceeding measurements, multiple scans were used with a smaller integration time. The averaging of the delay line, could in part explain the higher X for multiple runs.

Chirp

In this section, we set out to study how the chirp of the IR pulse altered the signal trace. We surmised that the chirp could compensate for the positive dispersion in the optical elements, thus impact the detected THz bandwidth. For clarity, the discussion firstly introduces pulse stretching and compression where one anticipates chirp generation. Next, we present two experimental studies of the chirp's impact on the THz radiation.

In section 2.2, we introduced the chirp of a pulse. In the Solstice laser system, the chirp of the pulse arises from the stretcher and compression stages, which are similar in form. Figure 4.12 illustrates typical stretcher stage.

Here two gratings diffract the pulse such that the longer wavelengths and the shorter wavelengths of the pulse are separated spatially. The photons are reflected back by a mirror, and the pulse is compressed/stretched. By moving the mirror, one can alter the chirp of the pulse. For the Solstice system, a clever scheme is used, with only one grating and one mirror. Conceptually it is the same as in Figure 4.12. The system allows for translation of the mirror, which in turn allows for changing the chirp of the pulse.

Solstice allows for the mirror in the compression stage to move. It can either step away from the grating (L) or closer to the grating (R). At any time, the Solstice control program records the position of the mirror. The representation normally varies between 0 and 3500 , where a large number relates to a significant distance between grating and mirror [53].

A study was conducted, by moving the mirror two steps in one direction and doing scans between each iteration. The iterative process continued for 8 times, before stepping the mirror back to the initial position. At this point, the process was repeated, but in the opposite direction. Note that the translation stage is imperfect, so after doing 8 scans in one direction clicking oneself back to initial point did not always yield the same result.

Table 4.9 shows the data for two experiments, represented by their respective dates. Run number 0 is the initial point at that particular date. Between the two experiments, the laser was overhauled and cleaned. The laser was then optimized, which explains the change in initial value. Hereafter, all figures refer to the run number, e.g. 6L, and the reader should conciliate with Table 4.9.

Figure 4.13 shows the time traces from both experiments. The biggest impact from changing the chirp is the peak value. We witness a drastic change in peak amplitude for

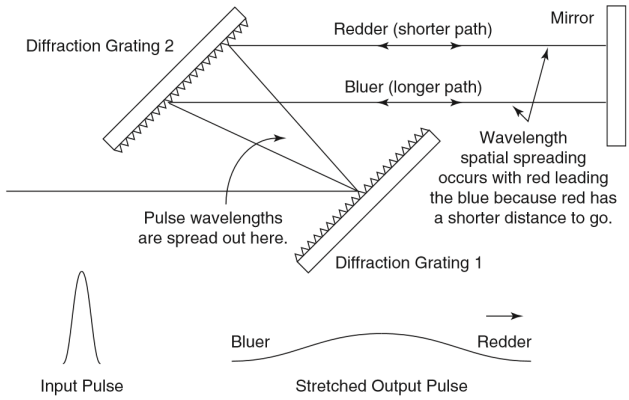

Figure 4.12: Conceptual illustration of pulse stretching using (See [53]). The scheme for pulse compression is comparable. Pulse chirp relates to the distance between the mirror and grating. The distance for a longer wavelength is shorter than for the smaller wavelength, producing the chirp. Figure from [53].

May 29th	April 7th	Run number
3148	3370	16L
3168	3388	14L
3194	3405	12L
3221	3434	10L
3247	3478	8L
3276	3503	6L
3315	3525	4L
3340	3565	2L
3370	3578	0
3396	3630	2R
3426	3660	4R
3461	3694	6R
3486	3730	8R
3513	3756	10R
3547	3789	12R
3577	3819	14R
3603	3846	16R

Table 4.9: The measured position of the retroreflector motor inside Solstice compressor stage for two measurements measurements conducted. The ”R” and ”L” is the total steps away or towards the grating inside the compressor stage, respectively

run number 6R and 8R. This behavior could be related to the generation process in the plasma, or it could be an artifact from the detection scheme.

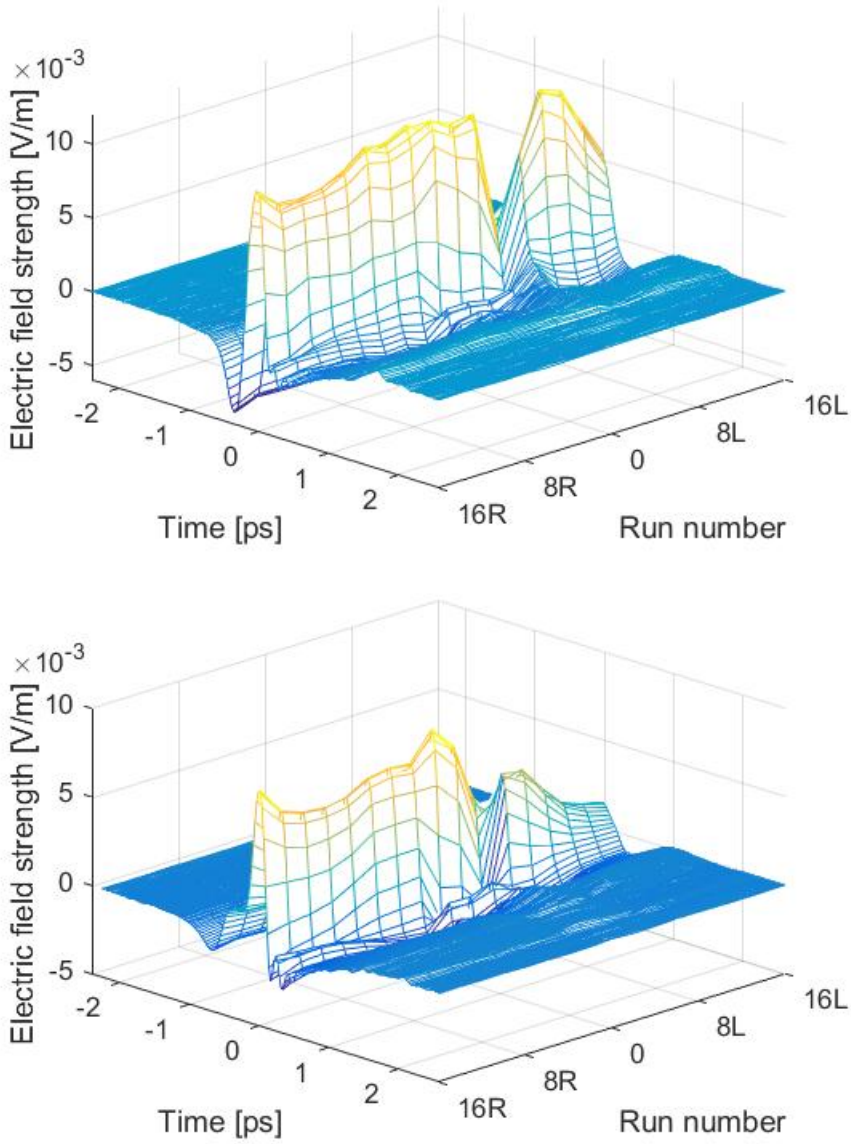

Figure 4.13: Time traces from the scans conducted between each increment, (TOP) May 29th (BOTTOM) April 7th. The upwards going y-axis shows the electric field amplitude, the horizontal axis on the right shows run number and the horizontal axis on the left is time in picosecond.

Any change imposed by chirp is arguably best observed in the frequency domain. Here the spectral components and their strengths can be observed giving an indication of how far out in the spectrum one can attain information. Figures 4.14 and 4.15 shows heat maps

and contour plots of the spectra of the time traces in Figure 4.13. Both figures have color bars, indicating the large and weak spectral components. Regarding bandwidth, 0 to $4R$ and $16L$ are excellent run numbers.

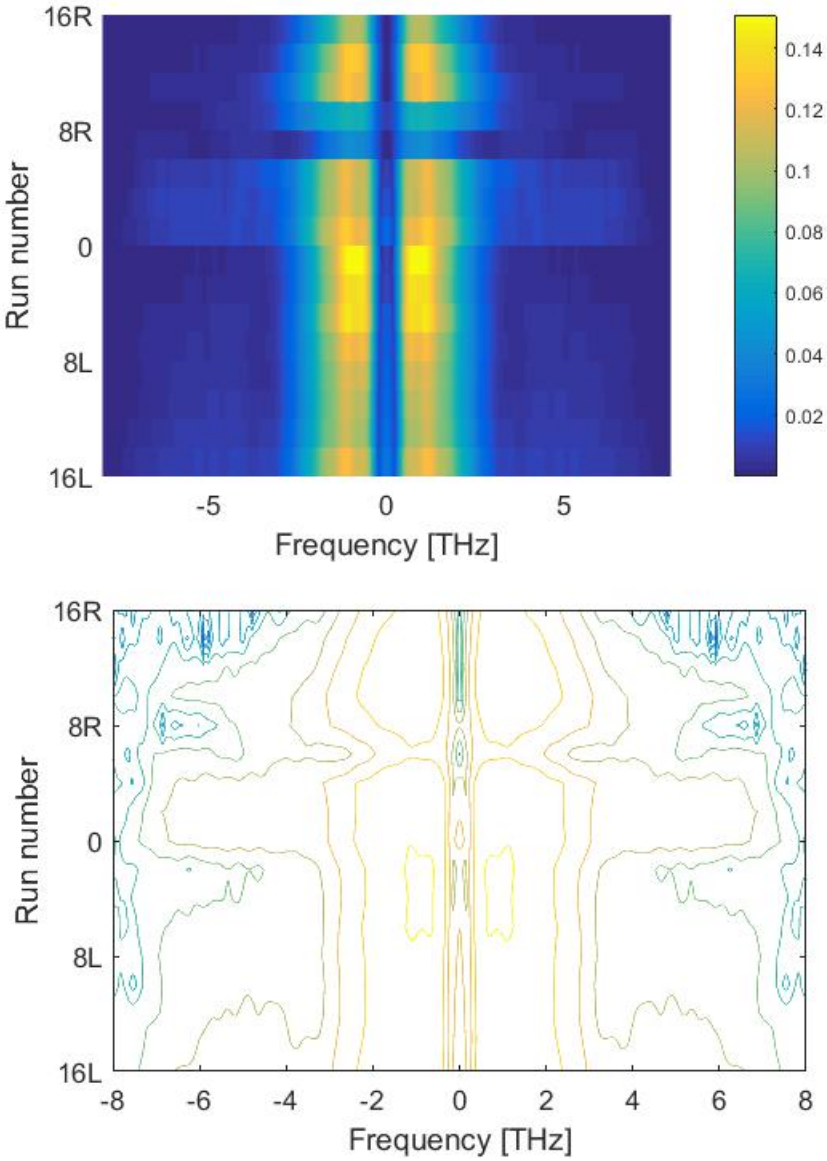

Figure 4.14: Scans from May 29th.The figures show the spectral amplitude seen from above. (TOP) Heat map of the spectral amplitude, w.r.t the colorbar to the right. (BOTTOM) Contour plot of the heat map on the top, w.r.t the colorbar on the top right. As we can see from both figures, the spectral bandwidth is greatest for values 0 to $4R$ and at 16L.

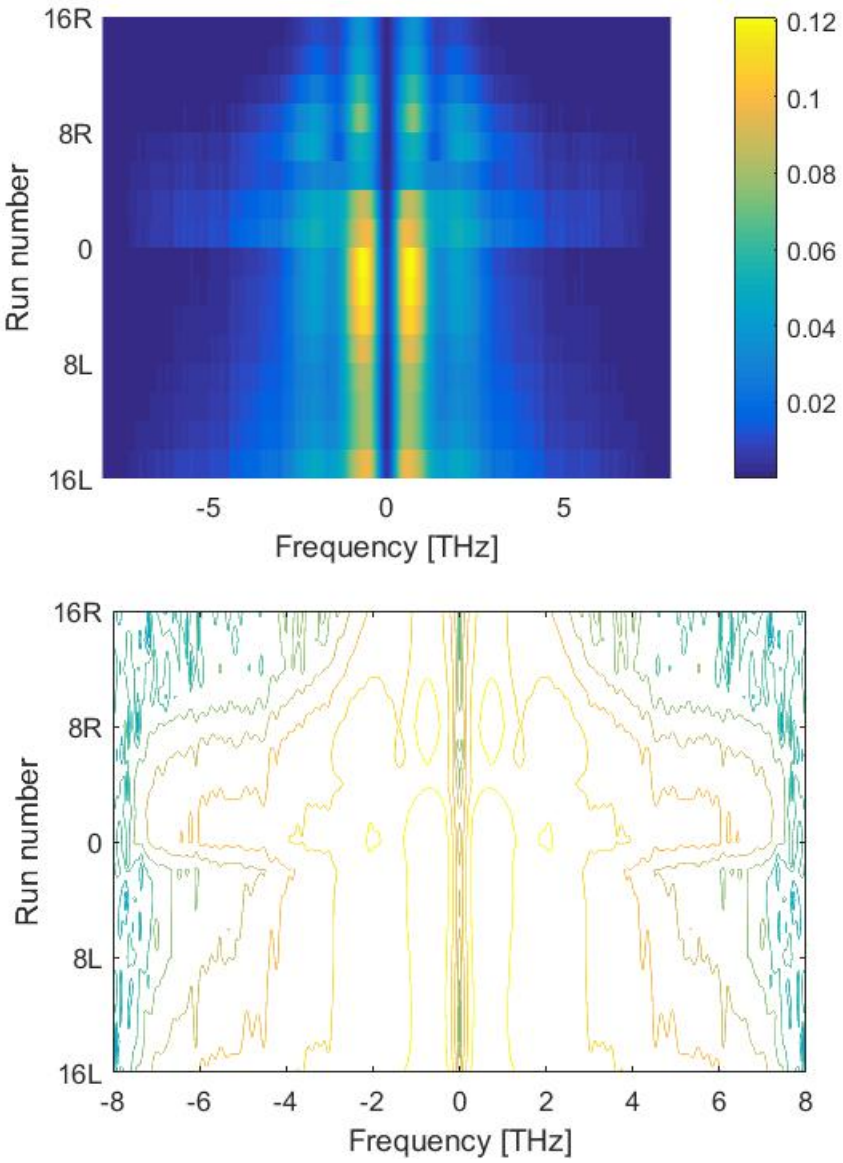

Figure 4.15: Scans from April 7th.The figures show the spectral amplitude seen from above. (TOP) Heat map of the spectral amplitude, w.r.t the colorbar to the right. (BOTTOM) Contour plot of the heat map on the top, w.r.t the colorbar on the top right. Similar behaviour to Figure 4.14, where the spectral bandwidth is greatest for values 0 to $4R$ and at 16L.

The observant reader may notice the discrepancy between mirror position in Table 4.9 and the optimum chirp for the two experiments. By overhauling the laser one tries to maximize the IR peak power by shortening the pulse width. Recalibration of different elements

in the laser might yield a different optimal position of the mirror in the compressor stage.

Shorter IR pulse width should give broader bandwidth as explained in section 4.2. Also, it seems plausible that a bigger IR peak power would yield an overall stronger THz pulse. The first scan, run number 0, for both experiments show a significantly broader bandwidth and maximum peak value for THz than most of the other scans. As we move away from the initial value, there seems to be a decline in both peak value and bandwidth range. To first order, this indicates that a shorter IR pulse and stronger peak amplitude gives a broader and stronger THz spectrum. The study concluded with 0 being the best run number, both for the IR pulse and THz pulse.

Correlated noise

The next part of the dissertation is a study of a correlated noise phenomenon for this setup. In short, one observed correlated noise after a certain threshold of signal quality (DR bigger than 10000). Figure 4.16 contains a spectrum which includes the correlated noise, best seen in the features at 7 and 12.5 THz and the ringing after 6-7THz. The nature of correlated noise is opposite of the previously discussed noise in section 4.3. The more one average the signal, the more prevalent the correlated noise becomes.

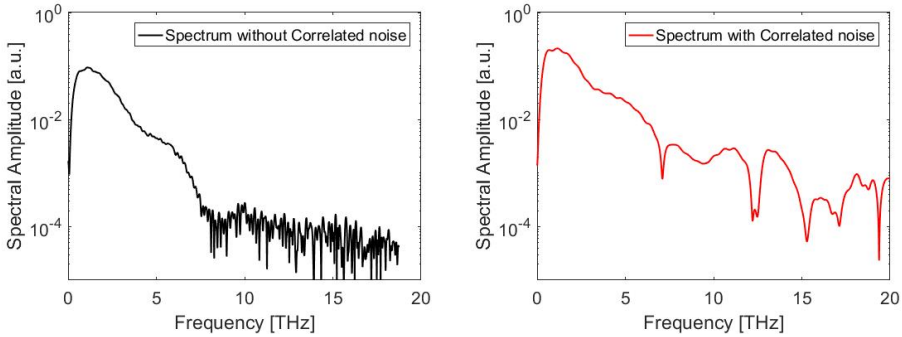

Figure 4.16: (LEFT) A typical spectrum for air with a dynamic range around 2000 calculated w.r.t the time trace. (RIGHT) Similar spectrum that includes correlated noise with a dynamic range above 10000. Light-Phonon interactions and phase mismatch between the THz-Pump and IR-probe are believed to be the reason for the ringing behavior.

In Figure 4.16, the spectrum without correlated noise show the expected behavior, i.e. no features and goes straight to noise floor at 7THz. On the other hand, the red spectrum shows clear features at 7 and 12.5THz, as well as a ringing function throughout the spectrum. The latter makes it hard to define the noise floor for the red spectrum. The features at 7 and 12.5 THz show a crystalline like response, which led to a belief that they were due to some optical element. However, as the lock-in amplifier is a vital part of removing the noise in the setup, a definitive study was done beforehand to understand how the lock-in varied the features.

Figure 4.17 displays multiple runs of the same silicon sample and air, done at different sensitivity settings on the lock-in amplifier. At first, we see that the dents at 7 and 12.5 THz move or disappear as one varies the sensitivity on the lock in. However, the pattern is inconsistent; for the same sensitivity setting the slope at 7THz shows up for the sample but not for air (red spectra). If the lock-in amplifier were solely responsible for the correlated noise, there would be some change in periodicity or amplitude in the spectrum at the bigger frequencies for each sensitivity setting. The line of thought here is that higher sensitivity has a higher threshold for detecting small signal changes.Consequently, less sensitive lock-in settings lead to losing more signal information at higher frequencies. From Figure 4.17 there seems to be an almost arbitrary relationship at higher frequencies between the different sensitivity settings.

The study continued with the EO-crystal (GaP $300\mu m$). Multiple authors discuss the problem asserted in an electrooptic detection system [7, 11, 8, 73]. Firstly there are phonon

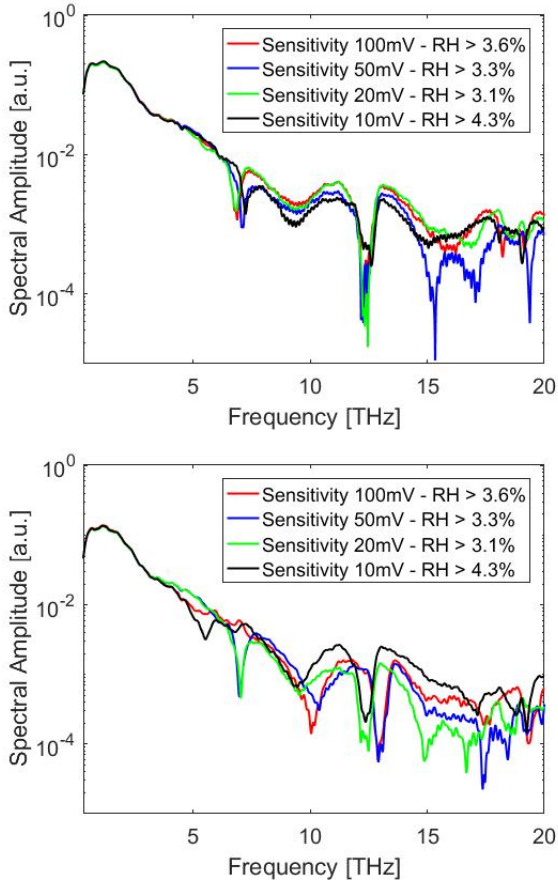

Figure 4.17: Spectra from multiple runs with different sensitivity. The experiments took over 10 hours, to achieve the remarkable dynamic range. Consequently, imposing fluctuations in humidity. The relative humidity (RH) is the lowest humidity throughout the scan, the maximum for each scan is 5% RH. (TOP) Silicon $500\mu m$ (BOTTOM) Air

modes in the THz regime for all the conventionally used EO-crystals, e.g. ZnTe, GaAs, and GaP. These restrict available bandwidth. Secondly, there is a phase mismatch between the group velocity of THz and the IR probe. Additionally, the complexity of the problem rise as the phase mismatch varies across the THz spectrum. It seems like the phase mismatch together with the phonon modes creates a profoundly complex spectrum.

The correlated noise is believed to be associated with the phase mismatch and phonon modes inside the $300\mu m$ GaP crystal. There is a believable resemblance of the frequency response given in Fig. 4.18 and that of the correlated noise in Figures 4.16 and 4.17. Following this line of thought, the correlated noise could bear into the believable higher frequencies around 6.5 THz due to phase mismatch. The correlated noise is a phenomenon observed at absurd signal qualities; fewer averages and a lower time constant gives a lower

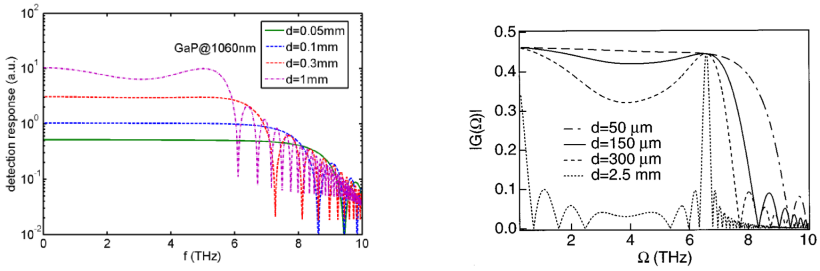

Figure 4.18: Detection response of the GaP crystal based on numerical analysis. The disparity between the figures is due to the different modeling. On the other hand, the ringing features are prominent for both models. (LEFT) Semi-logarithmic plot of the frequency response of GaP at various thicknesses. Figure from[8] (RIGHT) Normalized frequency response of GaP at several thicknesses. Figure from [73].

signal quality that ultimately eliminates the correlated noise. This can be seen from the first two spectra in Fig. 4.16. The approach is problematic, as it lowers the potential of the measurements as the dynamic range and signal to noise ratio drops.

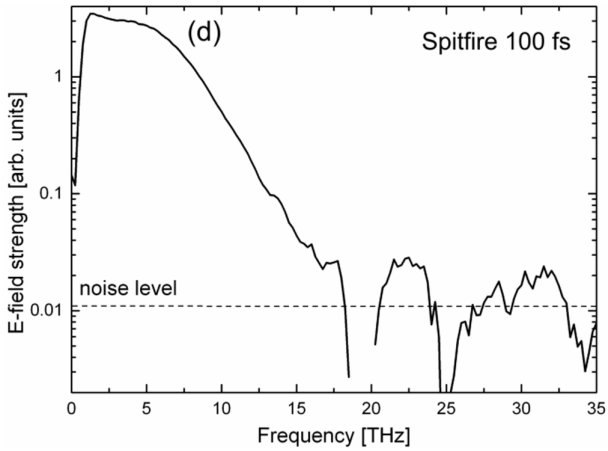

Figure 4.19: The THz spectrum from a generation in photo-generated plasma. ABCD is used as the detection scheme, making it possible to detect ultra-broadband THz pulses. The laser specs are; pulse width of 100-fs, 1 KHz repetition rate and $3.2W$ average power, very similar to the laser in this thesis. Figure from [76]

The observant reader may notice, that one of the implications of the latter is that a 100-fs pulse produces THz bandwidth way beyond the normal FWHM approximation in section 4.2. The obscuring by phase-mismatch creates a problem in justifying this experimentally. However, one encountered a similar system with a similar laser in [76], using the same generative method they reported a bandwidth of 15 THz, as shown in Fig. 4.19. This shows that an alternative detection method alike ABCD[25] is superior to the

EO-crystal method we use in this thesis.

4.5.3 FSEOS - Fabry Perot effect

In this section, we will present a Fabry-Perot phenomenon that arises from using electrooptic detection. Briefly explained, the THz radiation is reflected back and forth inside the electrooptic crystal. Ultimately, this constrains the resolution, as discussed in section 4.2.

The reflections mentioned above come out as a periodic response in the time-domain trace and the Fourier spectrum, as shown in Fig. 3.5. The effect will be present in all coefficients that are being extracted from the spectrum and have to be addressed to find the complex refractive index. Additionally, most EO-crystals show dispersion for a broadband THz pulse, consequently, the phase mismatch between the IR-probe and THz pump varies with frequency. The acquired phase mismatch increases with thickness. The preceding concludes in; decreasing bandwidth, increasing phase mismatching and increasing polarization change in the probe as the thickness of the EO-crystal increase.

In this thesis, we explain two different approaches to this problem. Firstly, we introduce an antireflective coating based on the research in [35, 36]. Next, we discuss the commonly used time window cutting. Where one simply leaves out any Fabry-Perot effect in the time trace by shortening it.

We exclude a detailed discussion on using a numerical approach. This approach removes the periodic nature of the reflections by looking at the frequency response of the GaP. On the assumption that all necessary information about the EO crystal is known beforehand. Including a detailed understanding of the phase mismatch between the two waves which includes dispersion relation for both wavelengths. Furthermore, a comprehensive knowledge of the phonon spectrum of the EO-crystal is required. The models are often used to fit experimental data onto the theoretical calculated model; this implies that the optical parameters cannot be extracted directly from two measurements. Also, in some cases the degrees of freedom can be increased, small variations of the EO-crystals attributes yield different results. Similarly, one could argue that the thickness of the EO-crystal itself is also a degree of freedom. All degrees of freedom should be accounted for, and explained. In this exposition, we exclude based on the above, numerical methods of the Fabry-Perot reflections in GaP. More precisely, we do not have a comprehensive understanding of the GaP-crystal. Thus a numerical analysis of the sort above creates less transparency and lowers the integrity of the results.

Coating GaP

The purpose of this segment was to coat a GaP crystal to get rid of the FP-reflections. By coating with a thin metallic layer (Cr), one was able to reduce the reflections inside the GaP crystal. However, work remains to eradicate the reflections completely.

The traditional approach $\frac{\lambda}{4}$ dielectric anti-reflective coating suffers from not being broadband enough. Also, THz radiation (1-10 THz) is in the range of $\lambda = 30 - 300\mu m$, requiring the layers to be tens of micrometers thick. Reported in [35, 36], metallic anti-reflective coatings (MARC) overcome the shortcomings above. The choice of material for MARC is any metal. However medium conductivity is preferred as high conductivity

metals require more precise control of the coating thickness [35]. In this thesis, we used Chromium as it was available at the lab.

The coating was done using a homemade thermal evaporator (dubbed $CMKIII$) as shown in Fig. 4.20. Thermal evaporation is a common method of thin-film deposition. Under vacuum conditions, a source material is evaporated. Vapor particles from the source travel directly to the substrate where they condense. In these depositions, a chrome plated tungsten rod from The R.D. Mathis Company was evaporated by direct resistive heating and the deposition rate measured by a crystal oscillator (Inficon SQM-160 thin film deposition monitor).

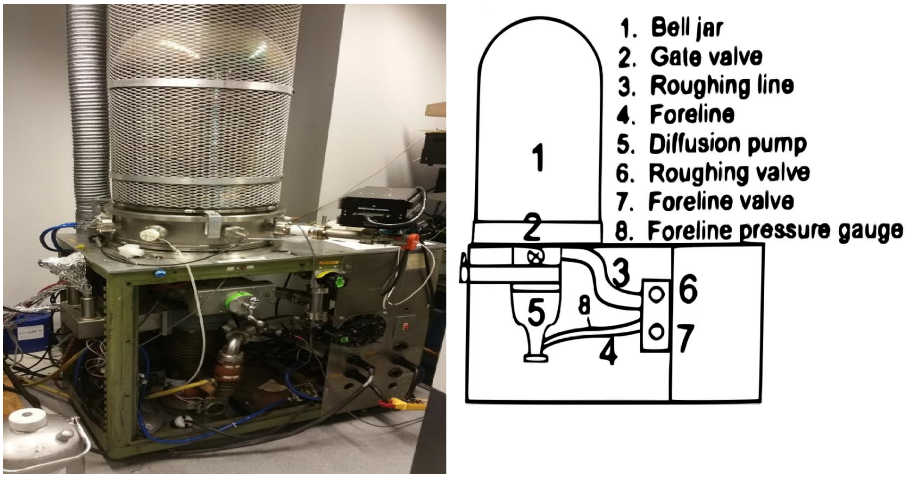

Figure 4.20: CMK III thermal evaporator deposition system. The bell jar (vacuum chamber) can be lifted up to install deposition source and specimen. (LEFT) CMK III (RIGHT) Explanatory schematic of CMK III.

We coated the GaP crystal at two instances; Table 4.10 shows the deposition information for each deposition. We chose to do small increments of deposition on the same crystal, to see the diminishing of THz reflections with thin layers of Cr on GaP. By considering the results for Si/Cr/Air interfaces in [35], we chose 30 and 50Åas targets. In between each deposition, we did experiments to see the effect it had on the peak amplitude of the reflections, seen in Table 4.11.

Deposition number	1	2	
Target Thickness of film	30	50	[Å]
Deposition Rate	2 - 2.4	1.8 - 2.8	[Å/s]
Base Pressure	$8 \cdot 10^{-6}$	$4.6 \cdot 10^{-6}$	[Torr]
Pressure during deposition	$3 \cdot 10^{-5}$	$6.5\text{-}6.8 \cdot 10^{-6}$	[Torr]
Pressure after deposition	$5.6 \cdot 10^{-6}$	$4 \cdot 10^{-6}$	[Torr]
Applied voltage bias	2.1	2.1	[V]

Table 4.10: Information for thermal evaporation deposition of Cr on GaP.

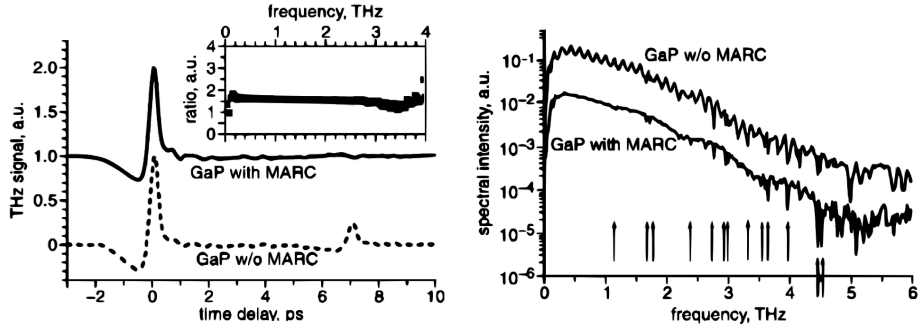

Figure 4.21: Comparison between THz signals measured with GaP with and without Cr MARC. Both of the curves are offset for clarity.(LEFT) Time trace with the frequency dependence of Cr MARC film. (RIGHT) Frequency domain data where arrows indicate water absorption lines. From [35]

From Table 4.10, the difference in pressure after the deposition and during shows that most of the pressure change is due to the evaporation of Cr. The deposition was conducted with a shutter between the sample and source. By resetting the total deposition counter and opening the shutter in the same instance, one measured the total deposited film thickness. As one reached the target thickness, one closed the shutter. The shutter was typically open for around 20 seconds.

Cr Thickness	1st FP-pulse
0	27.84%
30Å	26.84%
80Å	21.35%

Table 4.11: Table showing in percentage the relative peak amplitude of the first Fabry-Perot reflection to the main pulse

From Table 4.11 we see a decline in the relative amplitude between the main pulse and the first FP reflection from GaP. Based on simple linear model the optimum thickness should be around 370Åfor the total removal of the reflections. As [35] does not report the thickness of their GaP/Cr coating, we have no comparable results.

The trade-off using MARC is that one imposes partial absorption of the IR probe going through the coating. Figure 4.21 shows GaP coated with Cr, reportedly suffering a 45% loss of the probe power [36]. The same authors suggest using ITO instead of Cr to prevent the 45% loss.

Time Window

In this section, we introduce the time window limiting. By limiting the time trace of the signal, one can leave out the reflections coming after the main pulse. However, as

discussed in section 4.2, a shorter time window restricts the resolution of the FFT. Consequently, filtering out spectral traits like absorption lines and dispersion effects.

A typical cutting of the time domain and the effect on the spectrum, optical parameters, and time signal are shown in Figures 4.22 and 4.23. The spectra and time traces in Fig. 4.22 correspond to the refractive index and absorption in the same row in Fig. 4.23. From those above, we see the distortions produced by the multiple reflections inside the GaP. By reducing the time window to a smaller portion of the time trace, we remove the distortion as can be seen in the middle and lower part of the figures.

In this segment, we consider two important aspects of cutting the time window. Firstly, we will address the problem of physical interactions and their end and start. Next, we discuss approaches to the resolution constraints by including more of the scan before the main peak.

By cutting the time window, one may lose physical information. The loss will typically lead to an ill behavior in the refractive index. On the other side, the time window is restricted by the period between the reflections. A thicker crystal will have more delay between each pulse. Thus bigger time windows can be used. Arguably, proper restrictions on the time window can be made to contain the information. Particularly for thicker EO-crystals.

Looking at the top of Figures 4.22 and 4.23, we see periodic ringing in both n and κ. Moving down one row, we see that by removing the FP reflections from the GaP we reduce the effect, but there is still some malformation. We believe this is due to the artifacts before the pulse, which are not unique to this system. By moving to the bottom of the figures, we see that by removing the artifacts, we attain cleaner absorption coefficient and refractive index. This behavior plus the constraints on the time window in each direction due to FP and artifacts implies that the system is restricted to either low-resolution measurements or distorted n and κ. The resolution is sub-optimal 87 GHz for the signals at the bottom of the figures.

A Personal discussion with Eric W. Hansen at Thayer School of Engineering at Dartmouth, made us believe that we could add zeros on the end of the signal trace to increase the FFT resolution. Figure 4.24 shows a typical zero-padded signal and its counterpart. We use the small time window at the bottom of Fig. 4.22 and add 160ps of zeros at the end. By doing so, we are always underneath the Solstice laser beam uncertainty of 6GHz. The bottom of Fig. 4.24, shows an absorption coefficient, from 4.3 to 4.5 THz. Due to the inverse relationships between frequency and time, a longer padded signal will create a more refined spectrum profile. Consequently, the absorption coefficient calculated by a padded signal should be more accurate. [71] includes a discussion on the matter; reporting that a padded signal is better than a small time windowed signal. However, the physical counterpart of the padded signal is superior, i.e. a full scan. For the setup in the current configuration, we believe that a padded signal with a smaller time domain is the best possible signal producible.

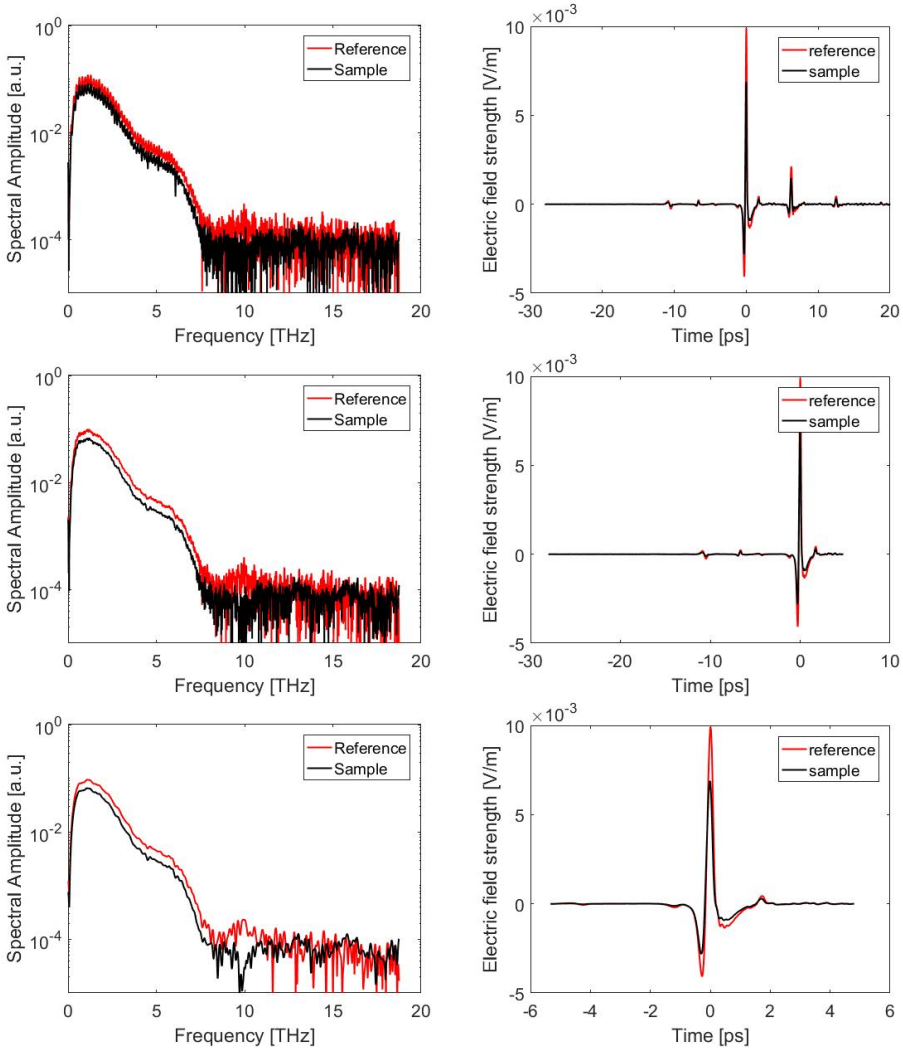

Figure 4.22: Three time-windows and their corresponding spectrum to the left. (TOP) The longer time window, including main pulse, both artifacts and multiple FP-reflections from the GaP. (MID) Time window including main pulse the artifacts (BOTTOM) Time window only including the time window. We see from all the figures that removing the artifacts and FP-reflections gives a cleaner and less distorted spectrum. Note that the spectra bandwidth is limited to 19 THz because of the incremental step length of the measurements

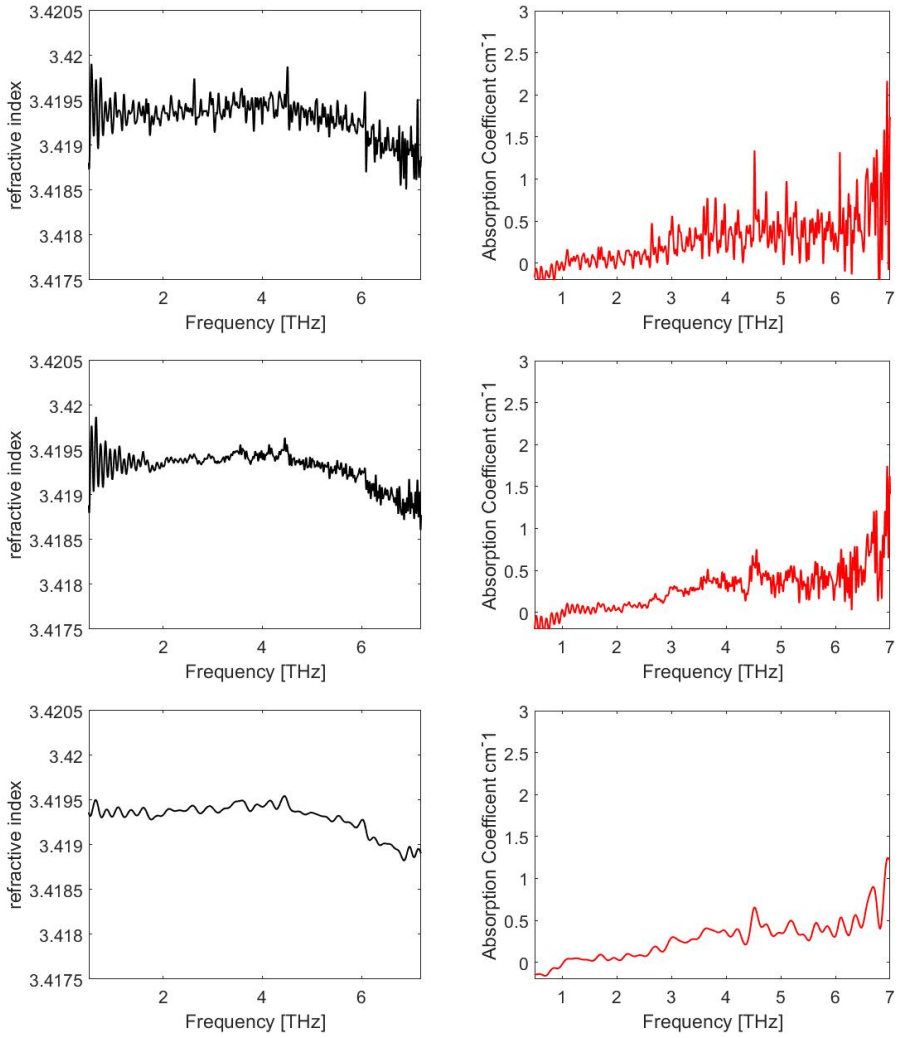

Figure 4.23: The calculated refractive index (LEFT) and absorption coefficient (RIGHT) of the signals in Fig. 4.22. The top, middle, and bottom correspond to the top, middle and bottom signals in Fig. (4.22). We observe that the values are essentially the same for the refractive index and absorption coefficient for the three calculated cases but with less noise due to artifact and Fabry Perot reflections in the GaP.

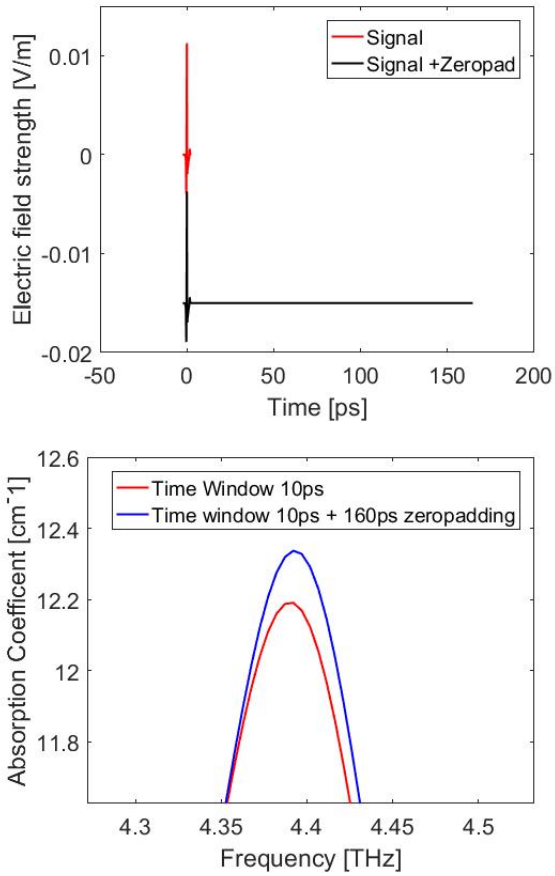

Figure 4.24: (TOP) Time trace of a unpadded and padded signal. (BOTTOM) Absorption coefficient for the same sample, calculated with or without zero-padding.

Chapter 5

Results

In this chapter, we present several measurements done with an improved THz-TDS setup. The idea behind all the measurements is to compare them with published data to find out whether the setup is working or not. We will answer this as a discussion with all the results in mind in the next chapter. Moreover, we will use the next chapter to clarify the source of significant errors in the experiments.

Each sections in this chapter is a mixture of results and discussion. We base the sections discussion on the discrepancy between measurements and literature with a small conclusion at the end. The Silicon section is different; here we also include two small sub-sections on polishing and doping. We state what we believe to be errors in each single measurement and let them form the baseline for the discussion in the next chapter.

For the measurements, we wanted a variety of samples linked with THz science. The sample chosen for these measurements are part of two research efforts NTNU and KTH. Silicon, Germanium and Fused Silica are of interest in the field of THz-waveguiding (NTNU). KTP is a potential source for efficient THz generation through quasi-phase-matched optical rectification(KTH). Additionally, as a means of understanding the limitations it imposed as an EO-crystal, we measured GaP. We will also present a proof-of-concept from the reflection part of the setup.

We include a list of technical similarities between all measurements below. These are true unless stated otherwise in the respective section.

- A time window is used to exclude artifacts/Fabry-Perot reflections from the EO-crystal.
- The time trace is padded such that the FFT resolution is 6 GHz, the padding is not shown in any figures.
- We offset the time traces vertically and horizontally for clarity. In the horizontal direction we introduce an arrow indicating the time delay
- All calculations of n and κ are done using the formula for material with absorption (equation (3.6) and (3.7)).

- The chopper modulates the pump beam at 200Hz
- Every measurement is done with an incremental step length smaller than $4\mu m$
- All samples thicknesses are measured using a caliper.
- Apart from the GaP-crystal, all samples were cleaned carefully with isopropanol

5.1 Silicon

The extensive studies on Silicon in THz regime together with a THz waveguiding research effort at NTNU made them excellent candidates to consider. In this section, we discuss three different Silicon samples. These are intrinsic optically polished Si, Intrinsic semi-polished Si, and n-type optically polished Si. By comparing the results, we wanted to check the effect of doping and polish as well as checking our results with published data.

Silicon has a well documented real refractive index of $n = 3.42$ in THz regime[61, 14, 29, 21]. Note that the published data differs w.r.t the absorption coefficient in the THz-Regime. Figure D.4 shows the results from [14], which is the experiment reporting the lowest THz absorption in Silicon [14]

From the results Silicon results, we will try to answer if polishing has an effect on the measured n and κ. Does doping increase absorption? How does our data for intrinsic HRFZ Silicon compare to published data, and what can we learn from it?

5.1.1 HRFZ Silicon 4.46mm

We present a measurement of an optically polished 4.46mm thick HRFZ (High Resistivity Float Zone) [111]-cut silicon ($R_0 > 20000\Omega cm$) sample. The measurements consist of five runs with a time constant of 100ms, 50mV sensitivity and 24dB/oct filter decay. The relative humidity of the reference and sample measurements were 3%.

Figure 5.1 show the time domain trace and spectrum of the two pulses in the measurement. The spectral signals reaches the noise floor around 7.5THz.

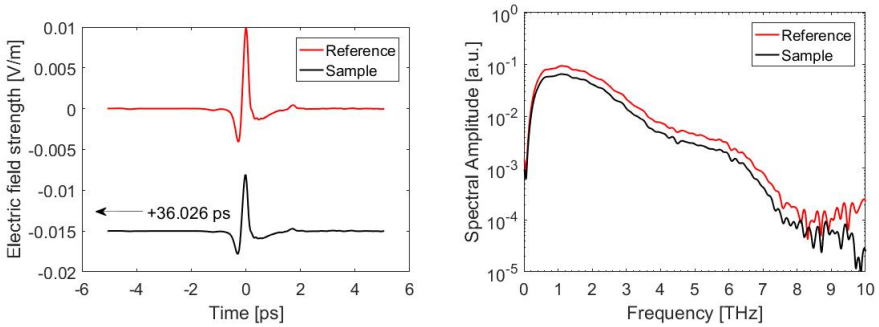

Figure 5.1: (LEFT) The time trace of the two measurements (RIGHT) The corresponding spectra for the figure to the left.

From Figure 5.2 we observe that the maximum measurable absorption coefficient limits the experiment to 7.5THz (see section 4.3). The increased fluctuation in the measured absorption coefficient is due to the lower DR at higher frequencies. The absorption coefficient (Figure 5.3) has negative values until 1THz; this is not uncommon in THz-TDS and can be seen in e.g. [3, 14]. Moreover, the authors of [38] shows the importance of a factor explaining the Gouy phase shift (see Appendix F.3) as one focuses the THz beam. We believe the negative absorption is related to the Gouy Phase shift and improper geometrical beam consideration in the calculation/experimental model presented in this thesis. This will be discussed in section 6.1.3.

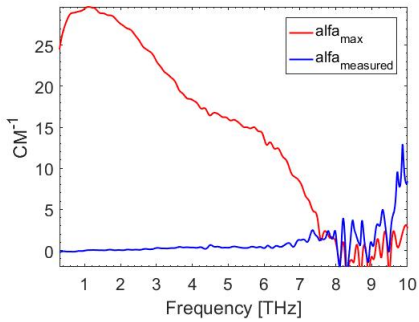

Figure 5.2: Absorption coefficient in blue and the maximum measurable absorption in red.

Figure 5.3 shows very low absorption in the regime 1 to 2.5 THz, comparable to the values in [21]. However, compared to [14] (Figure D.4) these measurements are at least a magnitude above for the lower frequencies. The next region, from 2.5 to 4.5 THz, shows much higher absorption and a relative rise in absorption compared to [14]. Comparing results to an earlier experiment [40], we see similar values for the higher frequencies, but far lower values for the lower frequencies. The discrepancy between [21, 14] and [40] is explained in [21, 14] as sample purity. However, the sample in this thesis is similar to the purity level in [14, 21]. Therefore, we assign the discrepancy in absorption coefficient to the relative change in humidity between reference and sample measurements. The humidity discrepancy is further discussed in section 6.1.2. The absorption increases in the regime from 4.5 to 7THz, these values are similar to that of [40]. However, we believe that these values should be lower due to sample purity and the aforementioned ambient environment surrounding the sample.

The refractive index is close to the values proposed in the published data of 3.42, with modest to no dispersion. On the other hand, the refractive index is unstable compared to [14]. Most likely related to the issues mentioned when discussing the absorption coefficient. As the refractive index from 1 to 4.5 THz is similar to [14], we believe that the values after 4.5THz are valid. However, small features in the fourth decimal, like the one at 3.5 THz in Figure D.4 cannot be determined. Nonetheless, [14] observe a gradual decline around 4.5THz in the refractive index. In this thesis, the behavior stretches further into the higher frequencies. The gradual decline is contrary to measurements of Si in the region [40]. The results indicate that Si is non-dispersive across most of the THz bandwidth, but

that there might be a decline at 4.5-7THz.

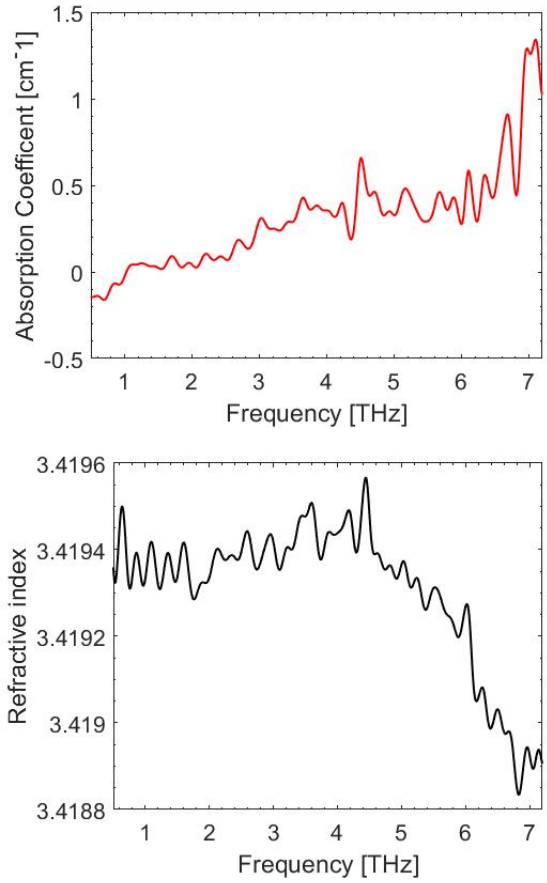

Figure 5.3: (TOP) Absorption coefficient of Silicon (BOTTOM) Refractive index of Silicon

We have investigated optically polished HRFZ [111]-cut Silicon in the regime 1 to 7 THz. In conjunction with existing literature, we have observed that Si is transparent and show negligible dispersion in the THz regime with $n = 3.4194$. There might be a gradual decline after 4.5 THz but we observe a negative absorption coefficient in the lower frequencies and an unstable refractive index, assumingly connected to improper geometrical consideration (Gouy phase shift). We record an overall higher absorption coefficient than [14, 21], which we suppose to be related to the change in relative humidity between reference and sample measurements.

5.1.2 Silicon Polish

We did measurements on another semi-polished Si sample from the same bulk as the Si sample above. We wanted to check the importance of scattering, i.e. does it matter for the calculations of n and κ if the surface is less polished?

Figure 5.4 shows the two samples used, HRFZ-1.48mm thick (semi-polished) and HRFZ-4.48mm (optically polished) thick Silicon from the same bulk piece. The relative humidity of the reference, optically polished and semi-polished sample were 3%,3% and 4%, respectively. Note that we did not understand how sensitive the setup was to small changes in RH at this point time of measurements.

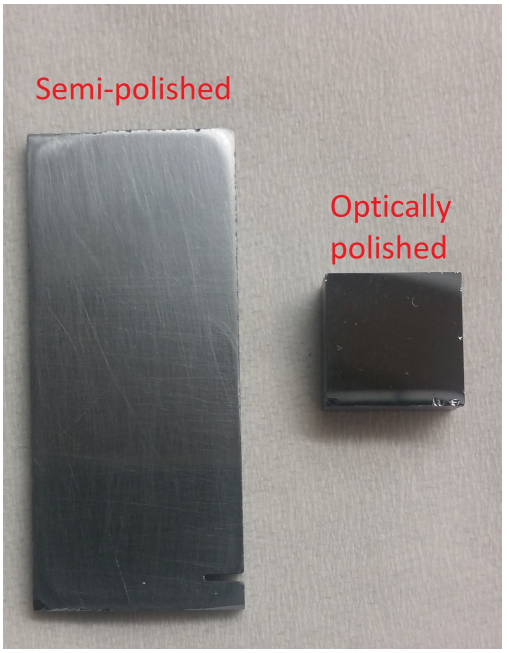

Figure 5.4: The two (LEFT) Semi-polished and (RIGHT) Optically polished Silicon samples.

From Figure 5.5 we see the resulting refractive index and absorption coefficient for the two measurements. Except for the feature at 4 THz, the polished sample shows much lower absorption coefficient than the semi-polished sample. Some of the increase in absorption is due to the slightly higher humidity in the semi-polished experiment. The refractive index shows a much more eccentric behavior. But, to first order, it is in the right area, compared to literature and the polished sample.

To understand the impact of humidity compared to scattering, we compare measurements of optically polished HRFZ at high humidity (around 7%) with a reference of lower humidity (3%). Opposing Figure 5.6 with Figure 5.5 we see that the behavior and features centered at 3 and 5.5 THz in Figure 5.5 is mostly due to humidity. However, the rise in absorption at lower frequencies is likely not from higher humidity. We observe scattering in the lower frequencies for this semi-polished sample. Moreover, it suggests that accurate

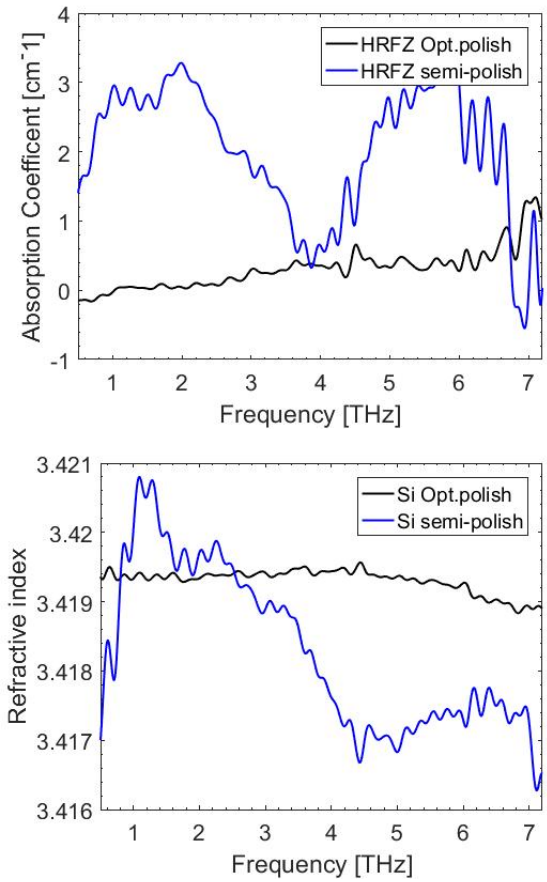

Figure 5.5: The measured n and α for optically polished HRFZ Silicon in black and semi-polished HRFZ Silicon in blue.

measurements of the absorption coefficient require optically polished specimens.

We believe that scattering effects are seen at the lower frequencies for this semi-polished sample. We further believe that accurate measurements of the absorption coefcient require optically polished samples, which makes sense as the calculation model does not take into account the scattering on surface.

When calculating n, the first frequency components are critical for settling the unwrapped phase, explained in Appendix E. Small variations in the start of the phase may bias the measurement; not observed in these measurements. Scattering effects at lower frequencies might propagate into the higher frequencies because of the MATLAB unwrap function. We believe that optically polished samples (on both sides) should be used for accurate measurements not only for α but also n.

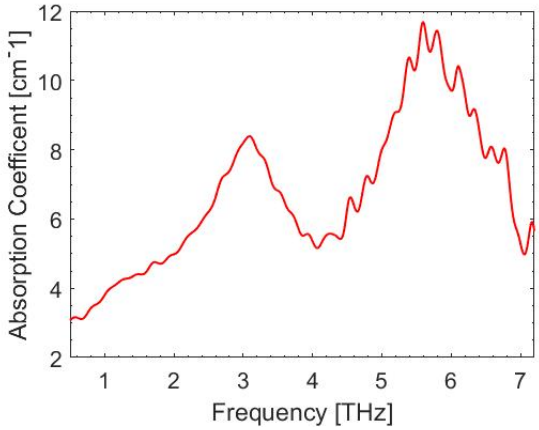

Figure 5.6: Measured absorption at relative humidity 7% for sample measurement and 3% for reference

5.1.3 Heavy doped n-type Si

We conducted an experiment on an optically polished 4.51mm thick n-type Silicon sample doped with Phosphorus ($R_0 = 0.05$ - $0.15\Omega cm$). The relative humidity of reference and sample measurements 3% and 7%, respectively.

From Figure 5.7, we observe a strong attenuation in the time trace. Besides, the spectrum for the sample is attenuated strongly for all frequencies. In [67] they measure a $260\mu m$ thick $0.1\Omega cm$ silicon sample in the range from 0.1 to 2THz using TTDS. They argue that the measured silicon sample is practically opaque at room temperature, and thus they were not able to do a proper analysis. We believe that we are observing a similar effect in this measurement. Thus we are not able to correctly measure n or κ.

By lowering the temperature of the sample to 80K, the signal increased sufficiently to determine n and κ. At this temperature, they show an absorption of $300cm^{-1}$, whereas we measure $20cm^{-1}$ at 300K. We believe the values from our measurement to be wrong. In [67], they also study less doped samples, which they can measure at room temperature. For the more moderately doped samples, they observe that absorption broadens into the higher frequencies at higher temperatures. One can assume that this is also the case for the highly doped sample. Agreeing with this experiment, where we observe full absorption into the higher frequencies. We surmise that Silicon becomes less transparent for THz radiation with increasing doping. We believe the absorption to be mostly related to free carrier absorption. We understand the temperature dependent behavior from [67], as the increase in the number of phonons at higher temperatures supplies the momentum needed for Free carrier absorption (FCA).

We can understand FCA through plasma oscillations, described by its resonance frequency ω_p [67]. Above this frequency one expect the FCA to be drastically lower. In [67], they find this frequency to be 2THz at 80K for the sample comparable to ours. Typically, the plasma frequency increases with temperature and doping, which may explain why we observe attenuation throughout the spectrum for our measurement.

To sum up, we do not believe the values of n and κ in this measurement because of the massive absorption of the sample signal. However, we observe that doping Si lowers its transmission as a THz-material due to free carrier absorption.

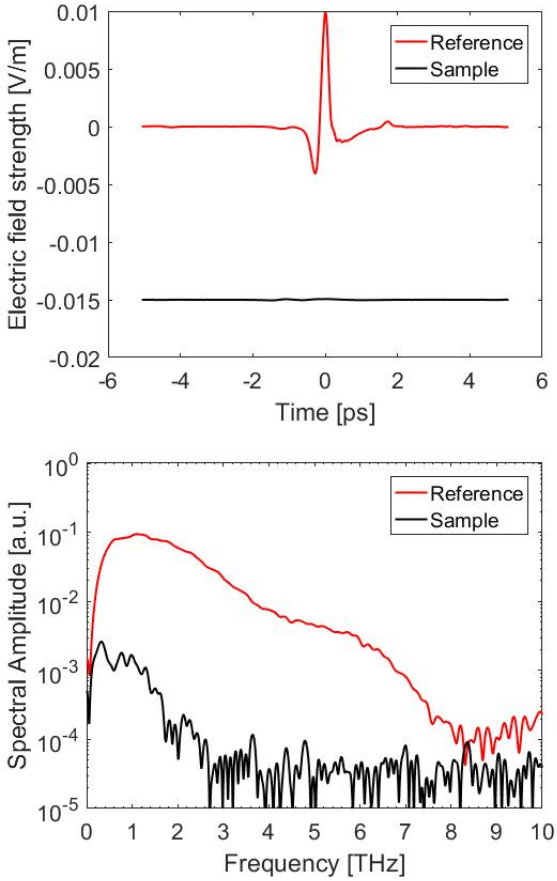

Figure 5.7: Time trace and spectra of the heavy doped n-type Silicon measurement

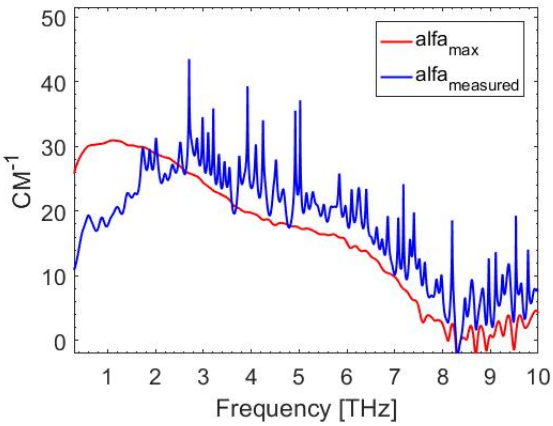

Figure 5.8: The calculated absorption coefficient and the corresponding maximum measurable absorption for optically polished n-type Silicon.

5.1.4 Fused Silica $1030.8\mu m$ (Fused Quartz)

A research effort at NTNU made fused silica an interesting material for THz wave guiding. The large absorption coefficient is well-documented [21]. Fused Silica finds its main use as material for communication fibers,its optical isotropy, producibility, relative low index of refraction, and cost can make fused Silica interesting as a THz fiber cladding material.

The results here are used to compare results from the experimental setup with literature. Also, by investigation Silica in the ranges that this spectroscopy setup allows, we create a base of knowledge that may find its use in further investigation on THz waveguiding.

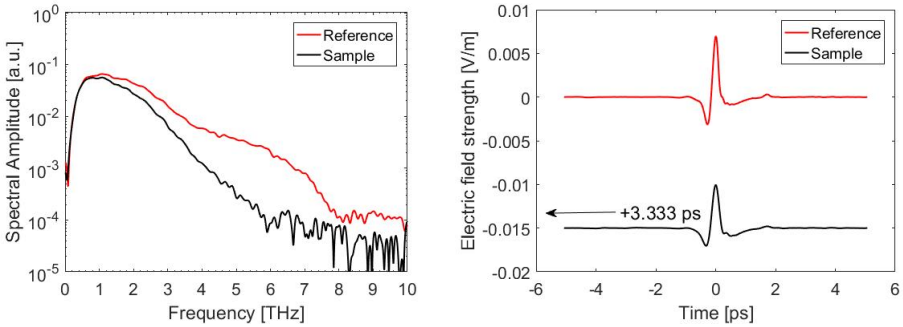

Figure 5.9: Reference in red and $1030.8\mu m$ fused Silica in black (TOP) The spectra from the two pulses. (BOTTOM) The time trace for sample and reference are separated by 3.33 ps, vertically offset for clarity.

Figure 5.9 shows the time trace and spectra of the measurement. Here black is the $1030.8\mu m$ fused Silica and red is air. The relative humidity of the reference and sample measurements were 2.8% and 3.7%, respectively. The sample and reference spectra go abruptly to noise floor at around 6THz and 8THz, respectively. The uncertainty after 8THz is the truncated correlated noise from doing fewer averages and reducing the time constant.

Figure 5.10 displays the absorption coefficient in blue, alpha max in red and the refractive index in black. Based on alpha max, the measurements are believable until 6 THz. Similar to the first Silicon measurement (4.46mm), the absorption coefficient has negative values in the start. Consequently limiting the total believable bandwidth to 1-6THz

We compare results for refractive index from [21] (see Figure D.3) with Figure 5.10. The difference is in the order of 0.01, for this particular experiment we used a Total Variation scheme as described in [63] to calculate the thickness of the sample to $1030.8\mu m$. The error might be connected with sample alignment. The calculation method assumes normal incidence, and any small variation in angle will cause the transmission coefficients to change. Consequently, causing an error in the calculated refractive index. The small artifacts seen at the lower and higher frequencies of both the absorption coefficient and refractive index is believed to be system related.

From Figure 5.11 report an absorption coefficient of $6.9cm^{-1}$ at 2THz, whereas [21] report about $8 - 10cm^{-1}$ at 2THz.

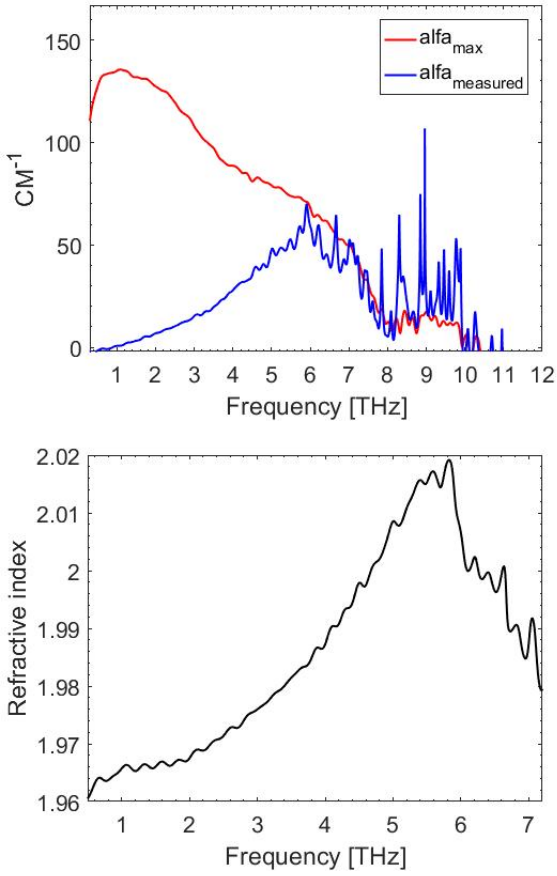

Figure 5.10: (TOP) The calculated absorption coefficient and the maximum measurable absorption based on [28] for fused Silica. (BOTTOM) The calculated refractive index for fused Silica.

Typically, amorphous materials like Fused Silica, have a quadratic relationship between absorption and frequency [72]. We can check if this relationship is obeyed by $f(x)/x^2 = a$, where a should be constant if the relationship is quadratic, the result is shown in Table 5.1. We have normalized the ratio w.r.t the absorption coefficient's value at 1 THz ($= 0.78$). Also, we observe a small increase as the frequency goes upwards. This is plausible, as the frequency dependent dynamic range rolls off towards higher frequencies, thus, the uncertainty of the measurement increase.

We would expect the true absorption coefficient to be lower for the sample, as we have a difference in humidity from the reference and sample run. It is likely that there is some difference in sample purity, and that ultimately this is seen as a difference in refractive index and absorption. Typically for fused silica this would be a difference in hydrous (OH) content and metallic content. [21] report a OH ppm content of 5, the fused silica used here is bought from UQG (Heraeus HOQ 310) with a OH $<$ 30ppm [1]. [21] report

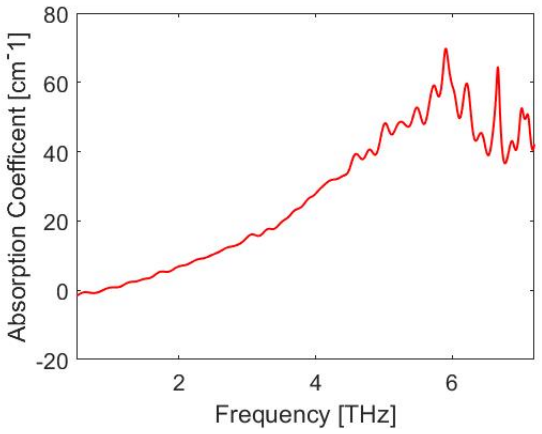

Figure 5.11: The calculated absorption coefficient of Fused Silica.

$\alpha\ [cm^{-1}]$	Frequency [THz]	Ratio $(\alpha)/(0.78 \cdot Frequency^2)$
6.91	2	2.2051
15	3	2.1368
27.87	4	2.2404
47.81	5	2.4513
69.56	6	2.4765

Table 5.1: The measured absorption at integer points of frequency. The ratio between the measured absorption coefficient and the frequency squared.

a metallic ppm of typically 1 while our Silica typically show an aluminum impurity more than 10 [1]. On the other side, [72] reports that synthetic silica glass of $1ppm$ impurities have smaller absorption than this measurement. We have higher ppm both OH and metallic content than two studies, and show higher absorption than one and lower than the other. This indicates that absorption is independent of OH or $metallic$ impurity at this low concentration, however further study is needed.

To summarize, Fused Silica shows a gradually increasing refractive index from 1 to 6 THz. As a cladding assuming a dispersion free core, the dispersion would create a frequency dependent interface between cladding and core. We observe a quadratic dependence of absorption and frequency, as expected. The results from published data are similar to what we have measured here from $1THz$ up until 2THz, where their measurements stop. This leads us to believe that the rest of the measurements are accurate until 6THz. However, there seems to be a difference of 0.01 for the refractive index and about -3 cm^{-1} for the absorption coefficient at 2THz. The differences are believed to be connected to the sample purity and the difference in humidity between the reference and sample run.

5.2 Germanium $1mm$

Germanium is a well-documented material with a relatively high index of refraction. In this section we will compare results from this setup with the results from the work of [21] (see Figures D.1) and [40]. The Germanium sample is optically polished.

Figure 5.12 shows the time trace and spectra of the measurement. Where black is a $1000\mu m$ optical grade Germanium window and red is the reference measurement. The relative humidity of the reference and sample measurements were 3% and 2.7%, respectively. Both spectra go to noise floor around 7.5 THz.

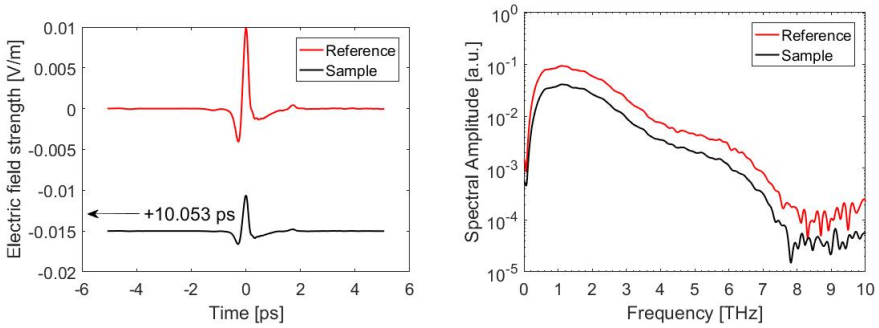

Figure 5.12: (LEFT) Time trace of the two THz pulses that are compared, black is $1000\mu m$ optical grad Germanium window and red is Air. The time delay between reference and air is 10.053 ps.Vertically offset for clarity. (RIGHT) The corresponding spectra for the pulses in the top.

From Figure 5.13 we observe the calculated index of refraction and power absorption with the measurements corresponding maximum absorption. From α_{max} we see that our measurement is believable until 7THz. The measured absorption is far higher than that of [40, 21]. Doping/impurity carriers might explain the higher absorption as doping of germanium alters the absorption in the low-frequency regime [51] (see Figure D.2). The method of growing Germanium may have an impact on absorption, as documented for Silicon [47]. Also, we would expect that the measured Germanium, in reality, has a slightly higher absorption. Because of the relative humidity of the sample run being lower than that of the reference measurement.

The refractive index is reported by [40, 21] to be in between 4.000 to 4.007 in the studied regime. The refractive index in this measurement is rising from 3.995 to 4.015 at around 3THz where it is stable until 7THz. The features between 3 to 5 THz are believed to be related to the difference in humidity from reference and sample run. The features at the higher frequencies could be related to the decrease in DR. The rise of n and decline of α in lower frequencies is similar to [21], and can explained by carriers.

We have measured optical grade Germanium; it seems to be in conjunction with existing literature when its refractive index is determined. However we see a much higher absorption coefficient than [40, 21], and wonder if it could be related to the method with which the sample was made.

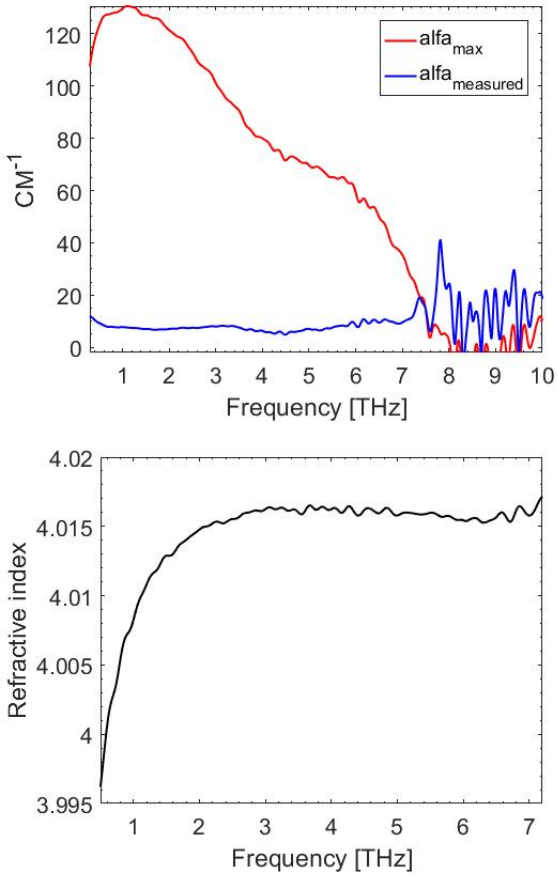

Figure 5.13: (TOP) Absorption coefficient in blue and the maximum measurable absorption in red (BOTTOM) The calculated refractive index for the measurement.

5.3 GaP $5mm$

One of the major concerns in this thesis is the Electrooptic detection scheme. As a part of understanding the behavior of the GaP crystal, we conducted a measurement on a $5mm$ thick [110]-cut GaP crystal, courtesy of the laser physics group at KTH. Moreover, GaP has well-documented features in the studied domain, making it an interesting material to compare with published data [32, 26, 34, 15, 48, 70, 57, 56, 68, 64, 24] .

From the results, we wanted to answer two questions: How do the results compare to the works of others, and how is GaP as an EO-crystal constraining the measurements in this setup?

Figure 5.14 shows the corresponding spectra in THz and time traces in ps of two THz pulses propagating trough air in red and through a 5mm [110]-cut GaP in black. We observe a odd behavior in the spectrum after 7 THz, this is due to correlated noise (see section 4.5.2) and is not linked with the particular sample. The reference measurement were done at 5.9% relative humidity and sample run at 7.8% relative humidity. The measurements consist of 1 run at $20mV$ sensitivity, $12dB/Oct$ and $3s$ time constant on the SR830 Lock-In-Amplifier. Figure 5.15 shows the calculated absorption coefficient in blue with the maximum possible measurable absorption coefficient in red (α_{max}[28]) together with the calculated refractive index. The parameters have been extracted using the equations for samples with absorption (equations (3.6-3.7). Regarding α_{max}, the results are believed to be believable from 0.5 THz to 6.2 THz.

The refractive index is off by 0.1 compared to Figure D.6. The discrepancy is partly explained by the calculation methods heavy dependence on thickness, as we were not able to measure the sample with a caliper. Another source of error could be that the THz pulse is coming in at a small angle to the surface normal. The absorption coefficient general trend is alike that of Figure D.6 (note the semilogarithmic scale) up until 4THz. We believe that the behavior beyond 4THz is related to pulse broadening, as discussed in section 6.1.5. In short, if the pulse is broadened substantially, the time window used in the calculation becomes shorter than the THz pulse, thus, we remove information from the analysis.

The erratic behavior after 4 THz may indicate features between 4 and 6 THz. The feature seemingly centered above $6THz$, might be related to the TO multiphonon process at $196cm^{-}1$ (5.98THz), or it be the $2TA$ which is at $207cm^{-}1$ (6.2THz) (Both modes seen in Figure D.5). The other small peaks before could be related to any of the multiphonon processes below $6THz$ that can couple with EM waves. The well reported two-phonon process at $30cm-1$ (0.9THz) is resolved in this measurement. However, these results are limited by the fact that we do not truly understand how the correlated noise is impacting the results.

Remembering that the EO-crystal is also GaP, the rising absorption between $2-4$ THz in absorption coefficient could be a reason for the drop in spectral amplitude between $2-4$ THz for the reference measurements. Comparing with the earlier Figure 4.19, we see that it does not show any behavior like this between 2 until 4 THz. There is more of a gradual roll-off, which seems to indicate that GaP as a detection crystal is not only limiting the bandwidth as discussed before but also the spectral amplitude. This limits the potentially measurable absorption, as the spectral amplitude is directly proportional to the maximum measurable absorption (α_{max}).

To some degree, the results are similar to the work of others, but we are seeing that

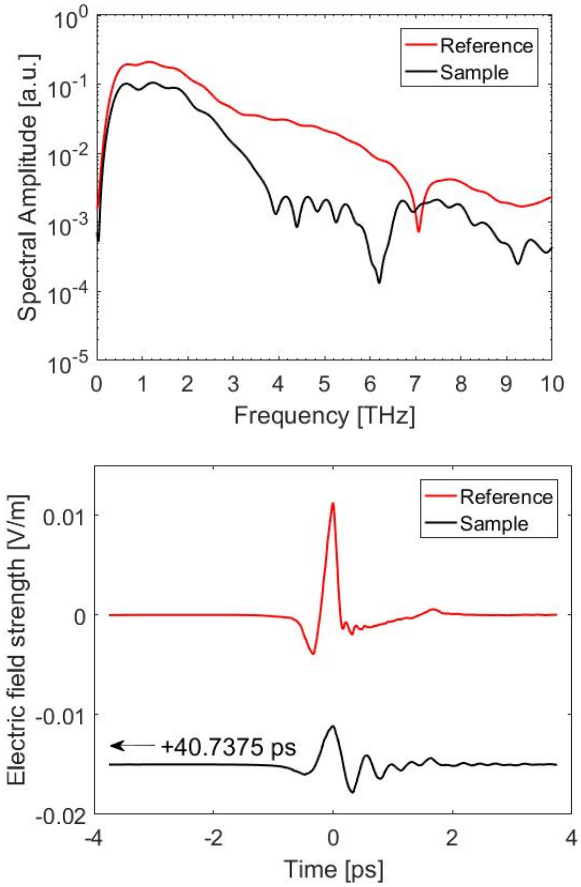

Figure 5.14: Reference in red and 5mm [110]-cut GaP in black (TOP) The spectra from the two pulses. The ringing behavior after 6-7 THz is due to a correlated noise source. (BOTTOM) Reference and Sample pulse from air and 5mm thick [110]-cut GaP, respectively. The time trace for sample and reference are separated by 40.74 ps, vertically offset for clarity.

the refractive index is off as we could not measure the thickness. With the caveat that we do not truly understand the correlated noise and that the time window might be removing information, we report findings of features that might be related to multi phonon processes. Also, the GaP as an EO crystal seems to limit all the measurements by truncating the spectral amplitude between 4 to 7 THz.

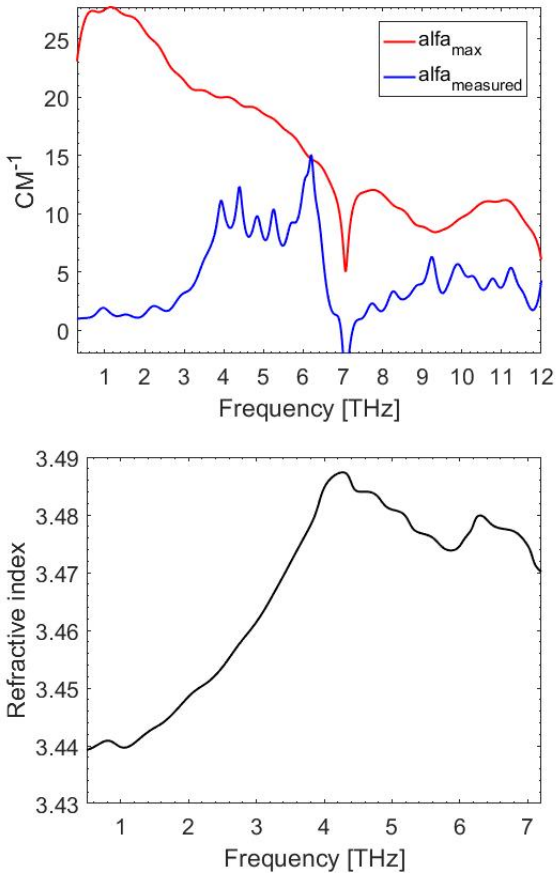

Figure 5.15: Calculated n and α from equation (3.6). The measurements are believable from 0.5 to 4 THz (TOP) Absorption coefficient in blue, and the maximal measurable absorption for this particular experiment in red. (BOTTOM) Refractive index between 0.5 THz to 7.2 THz.

5.4 KTP $KTiOPO_4$ $500\mu m$

KTP ($KTiOPO_4$) is a biaxial ferroelectric material known for its large nonlinear coefficient. Moreover, electric field poling of KTP makes it an attractive material for quasi-phase-matching structures. This, in addition to vigorous phonon-polariton couplings make it very interesting for the generation of THz. Being a part of the preliminary analysis, we did a transmission measurement of a 0.5mm thick KTP crystal. From these results, we want to check if it is possible to do KTP measurements in transmission for the setup in the current configuration before we are going on to future reflection measurements of KTP. We did the measurement with the THz beam propagating trough the KTP crystal in the z-direction with its polarization oriented in the x-direction. The relative humidity for the sample and reference run were 3% and $3,5\%$, respectively. We did 5 runs at $50mV$ sensitivity, $24dB/Oct$ and $100ms$ time constant. The time traces and frequency spectra of the two measurements are shown in Figure 5.16

There are spectroscopy studies on KTP in THz regime from 0.3 to 2.5THz along x,y,z direction in the crystal [6] and from 0.2 to 1.0 THz y and z in [44]. Where x,y,z is the axes described in Appendix D.5. [6] show a large absorption peak at 2.4THz in x-direction, the Figure is included in the appendix.

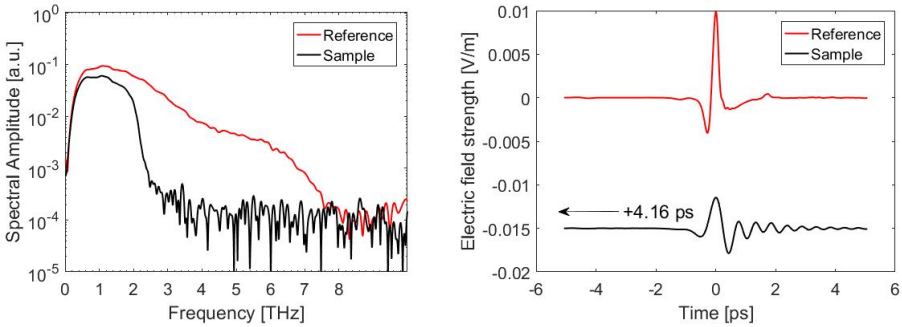

Figure 5.16: Spectra and time trace for reference (Air) in red and 0.5mm KTP propagating in z-direction with polarization along the x axis in black (TOP) The spectra from the two pulses. (BOTTOM) Reference and Sample pulse from air and, respectively. The time trace for sample and reference are separated by 4.16 ps, vertically offset for clarity.

Figure 5.17 displays the absorption coefficient in blue, alpha max in red and the refractive index in black. Based on alpha max, the measurements are believable until 2.5 THz. Similar to earlier measurements, we observe a negative absorption in the start. We see an abrupt increase in absorption coefficient around 2THz, which is probably the left wing of a phonon process. We are not resolving any Lorentzian/Voigt peaks, reported in [6]. However, this can be related to the magnitude differences in Dynamic Range. A rough estimate of the order of DR is comparing the maximum value to noise floor where the noise floor is normalized to 1. Estimating DR from [6] and Figure 5.16 gives an order of 10^8 and 3000, respectively, which indicates that they would be able to detect much larger absorption peaks. The higher dynamic range is expected from systems that have mode-locked lasers and photoconductive antenna because the repetition rate is much greater for

mode-locked lasers. Furthermore, the time trace from this experiment is limited by the reflections inside the $300\mu m$ crystal. Figure 5.18 shows that the main pulse has not died out before the reflection from the GaP crystal hits the detector, which is not the case for [6]. This indicates that we may be restricted to observe a smoother and less complete spectrum compared to [6]. The reason is believed to be that we are losing information due to the limitations imposed by the time window, or ultimately the FP reflections from the GaP. We observe a higher refractive index starting at 3.4 and increasing towards 4.2 at 2.5 THz, compared to [6] (approx. 3.25). The rise in refractive index is similar, however as mentioned before we do not see any peaks at 2.4 THz. In line with the discussion before, we believe this is also connected with the time window around the main pulse in Figure 5.18.

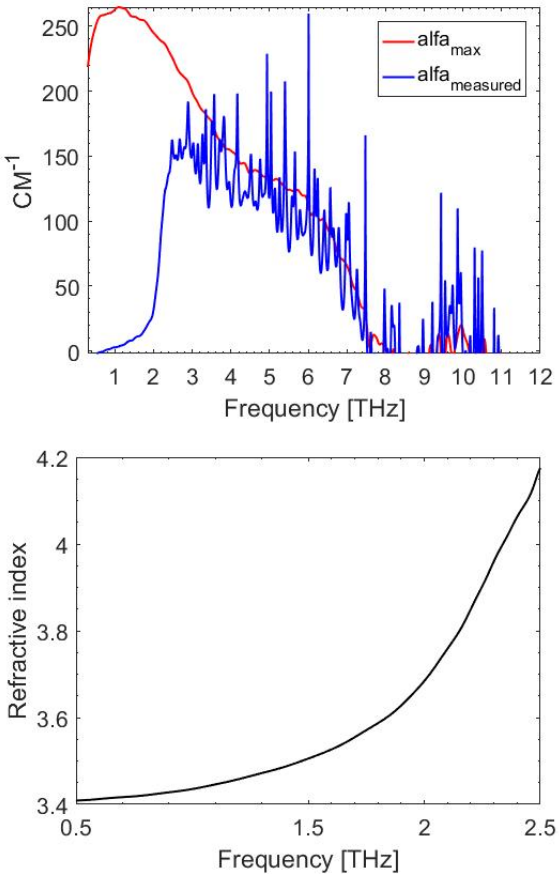

Figure 5.17: Calculated n and α for KTP in x-direction. (TOP) Absorption coefficient in blue, and the maximal measurable absorption for this particular experiment in red. (BOTTOM) Refractive index between 0.5 THz to 2.5 THz.

By creating a bigger time window and adding Fabry-Perot reflections, we distort the

spectrum but we do not exclude any information from the main pulse. The spectrum and time trace of the new window is shown in Figure 5.20. Calculations of n and κ show small features at 2.4 THz (see Figure 5.19). This indicates two things; Firstly, there might be features at around 2.4 THz but we are limited by DR. Secondly, that due to strong dispersive behavior from KTP, the time window restricting the reflections from GaP is removing information from the main pulse.

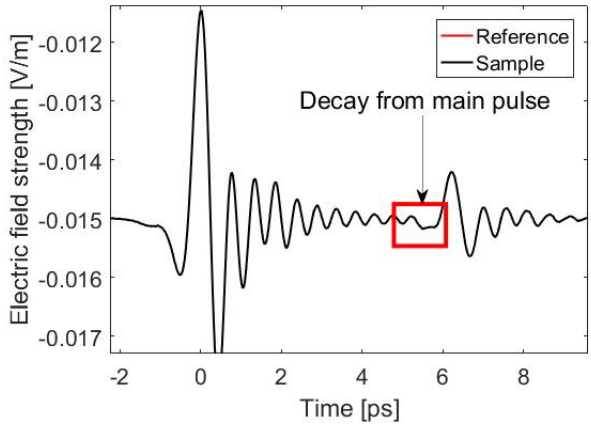

Figure 5.18: Broadening of the THz pulse due to assumable intense dispersion in THz regime. The reflection at 6 ps hits the detector before the decay from the main pulse is finished. Y-axis offset by -0.015.

The most significant result can be seen in the absorption coefficient plotted against α_{max}. Here we clearly see that the absorption coefficient comes down from the maximum measurable absorption at around 4.5THz, this suggests that there are at least one peak located between $2 - 4$THz.

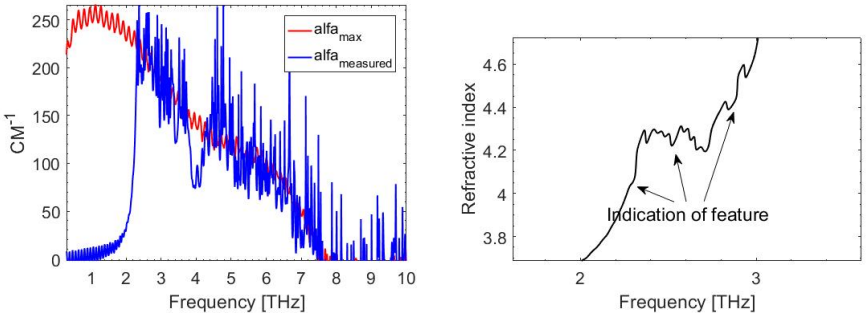

Figure 5.19: (RIGHT) Caluculated absorption coefficient and maximum measurable absorption for KTP. (LEFT) Possible features

The strong absorption and dispersion behavior is related to the optical phonons in the

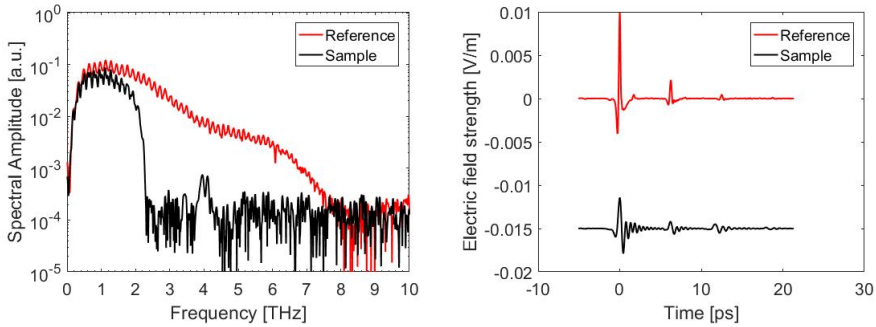

Figure 5.20: The new spectra and time trace when the Fabry-Perot reflections from the GaP are included.

THz region. We include a table with Raman active phonon modes in Figure D.7, where the most likely source of the absorption is the multiple phonons processes in Interval I.

The main objective of this study was to check if we could measure KTP in transmission mode in this setup. We have observed that, for this particular sample measurements are limited by DR and the reflections from GaP. Consequently, with the current setup configuration, this KTP sample cannot be resolved in transmission. However, we are able to say that there should be at least one peak between 2-4THz for KTP in x-direction.

5.5 Reflection Measurement

In this section, we will show a reflection measurement on a gold mirror. We based the reflection part of the setup on the work of Pashkin [5], where one does not use a focusing element to focus the beam onto the EO-crystal and instead let the probe beam coincide with the pump THz before hitting the sample. As we set out to built an improved setup, this part of the setup is one of the improvements. We include a proof of concept of the reflection part by discussing the time trace and spectra from a reflection measurement from a gold mirror.

Figure 5.21 shows the spectrum and corresponding time trace. Note that the x-axis is the translation stage position in mm. The main peak hits the detector just after -14mm, afterwards is a series of reflections from GaP and the spectral-splitter. The spacing between the main pulse and the first FP reflection is similar to that in transmission.

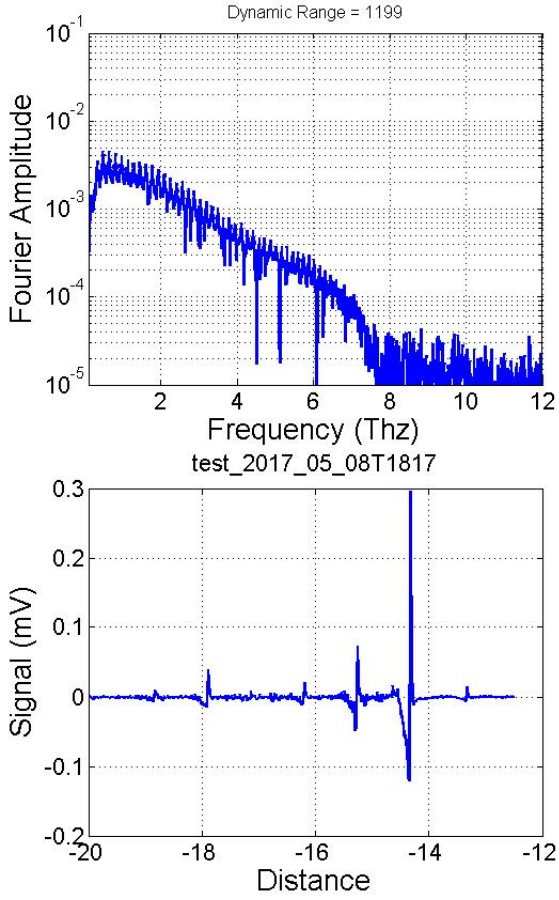

Figure 5.21: Reflection measurement on a gold mirror. (TOP) Spectrum of the pulse (BOTTOM) Time trace

The spectrum shows absorption lines due to water vapor. Its shape is similar to that of the transmission measurements, which is expected. The lower spectral amplitude values is a matter of signal strength. In an earlier iteration of the setup, we had similar strength to that of the transmission measurements. The total difference between signal and noise floor is similar to transmission measurements.

We have in this section displayed a proof of concept for the reflection mode of the thesis, based on [5]. We have seen that the Fabry-Perot effects do not disappear and that we do not need a focusing element onto the EO-crystal to do a spectroscopic analysis.

Chapter 6

Discussion

In this chapter, explain in greater detail the errors mentioned in Chapter 5. Greater error sources have a section for themselves, while we sum up smaller errors in one section. The error discussion forms the baseline for the last section of the chapter, where we present the current status of the setup.

6.1 Sources of error

In this section we discuss error sources in this thesis. We discuss the errors from the thickness measurements, humidity between reference and sample measurements. Further, we will discuss the negative absorption which we believe to be connected with the Gouy-Phase shift. Lastly, we present a brief section on smaller error sources. All of the errors mentioned here are in all the measurements performed in this thesis.

6.1.1 Thickness/Caliper

In this section we will discuss how an error in the measured thickness may propagate through the calculation scheme for n and κ. These errors may stem from the measuring tool, human error and thickness variations in the sample. For most of the samples, we measured the thickness using a caliper. The caliper is limited by its resolution (absolute error), which is 10 microns.

By defining the true thickness of a sample as d and the measured thickness as $d + \Delta d$ where Δd is the absolute error associated with the measured thickness, we can go on to check how this error propagates through our data analysis. For the refractive index, equations (3.4), the error is proportional to $\frac{1}{d+\Delta d}$. So, for overestimation of thickness, one will typically see a lower refractive index and vice versa.

Commonly one uses the calculated refractive index to calculate the extinction coefficient κ. The error then propagates from the calculated refractive index into the extinction coefficient through the fresnels coefficient.Moreover, the extinction coefficient is also in-

versely proportional to $\frac{1}{d}$ (i.e. $\frac{1}{d+\Delta d}$). However due to the logarithm, the error is less prominent (equation (3.5)).

We observe that an increasing sample thickness decreases the relative error associated with the caliper resolution. Consequently, leading to less error in the measured n and κ. Note that thicker samples yield more absorption, thus one is more likely to be limited by α_{max}. Figure 6.1 and Figure 6.2 show three calculated refractive indexes and absorption coefficients calculated with the equation for absorptive materials (equation (3.6-3.7) for Germanium and Silicon, respectively.

From the figures , we observe that the refractive index increases if we underestimate the thickness, and decreases if we overestimate. For the thicker Silicon sample, we see that the error margin is smaller compared to the thinner Germanium sample. The absorption coefficient is not as dependent on the thickness. Additionally, we see that overestimating/underestimating gives a lower/higher absorption.

To summarize, we see that the thickness measurement is one of the big sources of error. For the thinner Germanium sample, the refractive index is more sensitive to the change in thickness than the thick Silicon slab. This implies that thinner samples are more sensitive to errors in thickness when calculating its n and κ. This means that knowing the thickness of the sample is crucial, and the more accurately we know the thickness, the more precise the determination of n and κ. Note that the trends and features are not changed by a thickness measurement error, only absolute values.

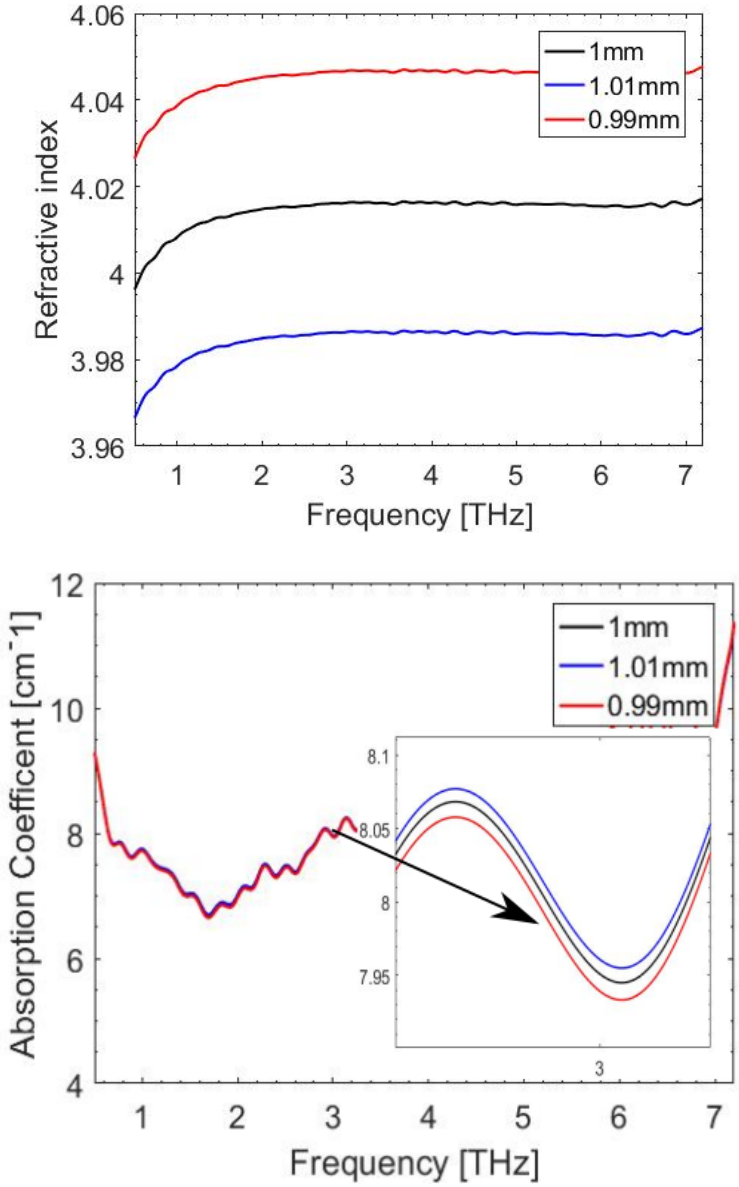

Figure 6.1: The absorption coefficient and refractive index calculated of the Germanium sample, for three different thicknesses, corresponding to the resolution of the caliper.

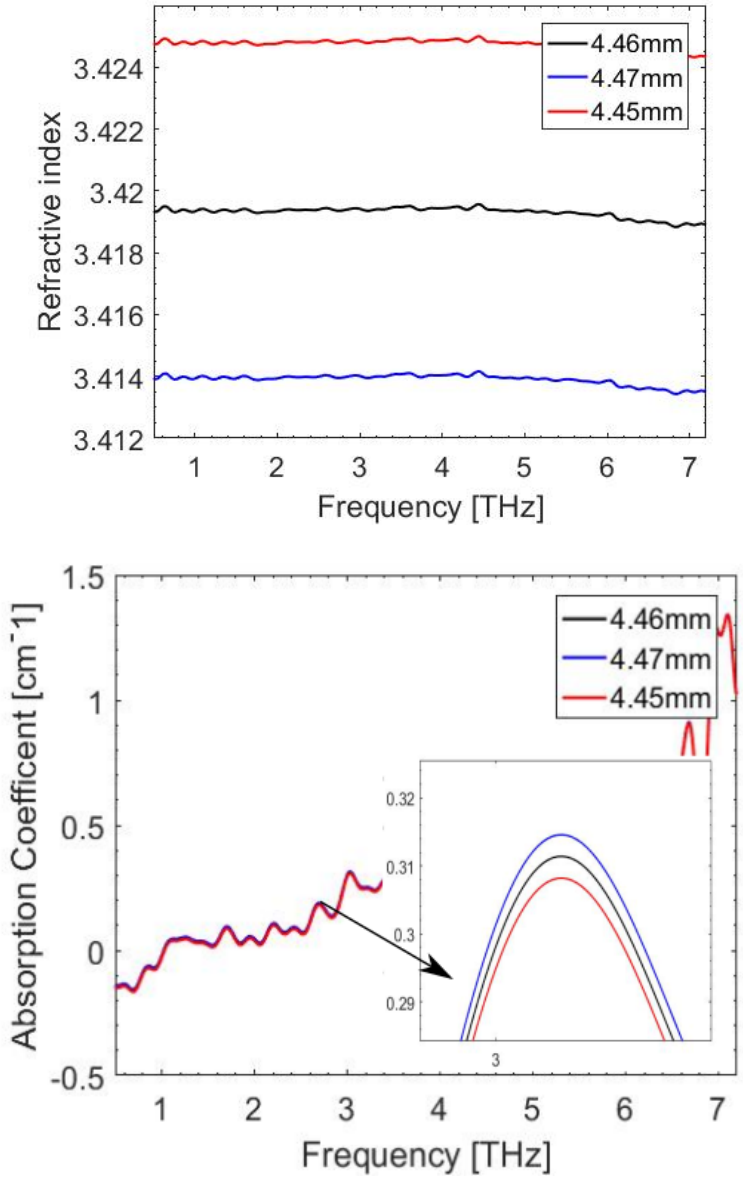

Figure 6.2: The absorption coefficient and refractive index calculated of the HRFZ Silicon sample, for three different thicknesses, corresponding to the resolution of the caliper.

6.1.2 Humiditiy

In this section we are going to discuss the problems due to a difference in humidity between sample and reference runs and the temporal stability of humidity. We do so by starting out with the fundamental equation of TTDS, i.e. the two signals FFT divided by each other. In addition, we include the extinction for different humidity in the two respective runs.

$$T(\omega)e^{i\phi(\omega)} = t_{12}e^{(K_R(\omega)L - K_S(\omega)(L-d))\frac{\omega}{c}}e^{-\kappa(\omega)\frac{\omega d}{c}}e^{i(\hat{n}(\omega)-n_{air})\frac{d\omega}{c}}t_{21}. \tag{6.1}$$

Where K_R and K_S are the extinction coefficients from humid air in the reference and sample measurements, respectively. L is the optical path length in air, and d is the sample thickness. In the calculation we separate the imaginary and real part of equation (6.1), so that we can calculate n and κ. In the case where $K_R = K_L$ we have negligible error. However, for the case where they differ we acquire $e^{(K_R(\omega)L - K_S(\omega)(L-d))\frac{\omega}{c}}$ into the calculation of α, which is observed in the experiment on polishing (Figure 5.6).

The polishing case is an extreme case, where the difference is 4%. The silicon sample is then calculated to have absorption much higher than it actually has. This kind of difference can be controlled by waiting a sufficiently long time.

However, equation (6.1) shows that the temporal stability of the humidity is crucial for accurate measurements of n and κ. Typically this stability can be achieved, either by doing runs without opening the box, and over a shorter period of time (as done in [14]). Or it can be achieved by controlling the inlet and outlet from the box, to reach a controlled equilibrium. The temporal stability of humidity is also dependent on the Drierite, as its ability to soak up humidity decrease with running time.

In this thesis, all measurements have been done disregarding the aforementioned. The RH has been recorded at the start of each run. Not accounting for the Drierite, that may soak up humidity in air faster or slower than the preceding reference measurement. The net effect is that all measurements in this thesis have a systematic error.

In conclusion, similarly to the thickness, the error associated with humidity can be understood mathematically from the formulas. Due to the strong absorption of THz in humid air, measurements are sensitive to differences in humidity between the measurements and the temporal stability of the humidity. We have found that this is a source of error for all the measurements.

6.1.3 Geometrical beam considerations

In this section, we discuss the occasional occurrence of negative absorption for frequencies above 0.5THz. We believe that there are two main contributors to the error in the measured absorption coefficient. Firstly, the Gouy-Phase shift (see Appendix F.3), which is an 180-degree phase shift that a Gaussian beam experiences between the two sides of the focal plane. We further believe that a sample may cause the THz beam to shift slightly consequently changing overlap at the EO crystal between IR-probe and the THz-Beam. We will first discuss the Gouy-Phase shift followed by the overlap at the EO-crystal.

When we calculate n and κ, we are considering a plane wave THz beam incident on a sample. Following [38], when introducing a sample we shift the THz focus as it refracts

into the sample. We can describe this as a translation of the focus in the direction of propagation as

$$\delta f = d\frac{n-1}{n}. \tag{6.2}$$

Where n is the index of refraction, d is the sample thickness, and 1 is the refractive index of air. According to [38] the focus change leads to a systematic overestimation of the refractive index. This overestimation relates to improper geometrical beam considerations. By approximating plane wave propagation, we leave out the Gouy phase shift related to Gaussian beam propagation (see Appendix F.3). This error influences the calculation of the absorption coefficient.

To understand how an overestimation of the refractive index affects the final result, we can take a closer look at equation (3.7). If the absorption coefficient is negative, then the extinction coefficient must be negative. The only possibility for the aforementioned to occur is that the factor argument of the logarithm is bigger than 1. This happens if the transfer function and the refractive index is large, it is the case for a low absorptive material such as Silicon. Any overestimation of the refractive index will, in turn, propagate into the calculation of the extinction coefficient. Particularly for the case where the extinction coefficient is close to 0 we can see a negative absorption coefficient.

The overestimation of n implies that for all samples, we see somewhat lower absorption for all the frequencies. [38] proposes an experimental method of estimating the error by moving the electrooptic crystal, to negate the effect of the longitudinal shift of focus due to the sample δf. We have not yet tried it for this setup.

A shift perpendicular to the direction of propagation at the EO-crystal may change the overlap of IR and THz, and subsequently changing the strength of polarization seen by the IR probe due to the Pockel's effect. Disregarding the loss from the sample, this may modify the strength of spectral components in the bandwidth of the sample measurement compared to the reference measurement. In [71], they argue that the linearity of the setup cannot be assumed between reference and sample measurements as a result of the above. Therefore, the perpendicular shift may change the $T(\omega)$ in equation (3.7). Moreover, if the shift is favorable for the sample measurement, one will experience stronger spectral amplitudes at certain frequencies, causing the absorption coefficient to be artificially low for these specific frequencies. As an example, if the transmission function $T(\omega)$ is larger than 0.7 for $n(\omega) = 3.42$, the extinction coefficient will be negative.

Both of the above issues occur from improper geometrical considerations in the calculations and in the experimental setup itself. We believe the Gouy-phase shift can be removed experimentally, i.e. keeping the sample consistently at one side of the focus. Also, [38] argues that the shift can be quantized and they have proposed an experimental scheme for doing this. Their method results in an extra term in the analysis of data, but it has the beneficial effect of removing the deleterious effects of the Gouy phase shift. The perpendicular shift may be circumvented with proper alignment. [71] proposes a series of measurements with HRFZ silicon plates to remove the lateral shift when introducing samples.

To summarize, the Gouy-phase shift is important when conducting TTDS. It will cause an overestimation of the refractive index which in turn can cause an underestimation of the absorption coefficient. A perpendicular shift of the THz beam as the sample is placed into

the setup may cause an error in the measured $T(\omega)$ resulting in an error of the calculated n and κ. This can be prevented by properly calibrating the setup as proposed in [71].

6.1.4 Polishing

In this section, we are going to discuss the importance of polishing both surfaces of the sample to optical quality. We base the discussion on the discrepancy between the semi-polished and polished HRFZ Silicon (section 5.1.2).

We observed that the absorption increased and the refractive index became more unstable at the lower frequencies. We believe the increase is due to scattering effects. We limit the discussion to the lower frequencies since we are confident that no other errors are critical for this frequency region.

When the terahertz pulse propagates through a sample, there are losses due to reflection at boundaries, absorption within the sample, and scattering both within the sample and from boundaries. The cause of scattering effects is stochastic variations of the refractive index in the material. Typically the variations are caused by imperfections, impurities, particle size variations and irregular or rough surfaces [31]. The HRFZ sample was made out of a highly pure Silicon piece. There should be negligible effects from impurities and particle size changes. We believe that the effects observed for the semi-polished sample are mainly because of the surface roughness. The polished sample shows a negligible increase of absorption for frequencies below 3 THz. The low absorption justifies the assumption that the scattering is primarily from surface roughness in the semi polished sample.

The scattering effect will cause less of the THz to reach the EO-crystal, and the absorption becomes artificially high as a result. The easiest procedure to reduce scattering error is to polish the sample.

The refractive index uncertainty may be related to increased uncertainty in the lower frequencies due to the absorption from scattering effects. In the worst cases, the MATLAB unwrap function produces a bias in the phase, as discussed in Appendix E. We believe that this effect is more prominent for higher surface roughnesses than our samples have.

Summarizing, we see an increase of absorption and uncertainty in refractive index due to scattering effects. We believe that the scattering is from surface roughness. The surface roughness causes an error in the analysis of n and κ which can be eliminated by properly polishing the sample.

6.1.5 Dispersive Samples

In this section, we examine how dispersion from a sample may limit the accuracy of our measurements. In particular, the relationship between the time window constraints on the calculations and the dispersive behavior. Dispersion is a phenomenon where the phase velocity of a wave depends on frequency. Typically for a pulse, this leads to pulse broadening since some frequencies move slower/faster than others.

In the calculations of n and κ, we use a time window to remove any FP-effects from the EO-crystal. By doing this, we limit the maximum change in the refractive index in the measurement. The time allows for 5 ps of phase delay, i.e., in a single pulse, the maximum relative delay between two spectral components is restricted to 5ps. The time delay of two spectral components can be described as,

$$\Delta t = \frac{d}{c}(n(\omega_1) - n(\omega_2)). \tag{6.3}$$

Where d is the sample thickness, $n(\omega_1)$ and $n(\omega_2)$ are the refractive indices of the sample at two different frequencies, c is the speed of light and Δt is the relative time delay between two spectral components. For this particular setup, if Δt exceeds 5ps for any two spectral components, we remove information by imposing a time window on the pulse.

In the Results chapter, we experienced that the KTP sample shows significant dispersion in the studied regime. Using equation (6.3), for the 0.5mm KTP sample we can only measure an absolute change of refractive index of 3, i.e. the minima and maxima of the refractive index can differ by maximum 3. A change bigger than this would create a loss of information in the time window, as the pulse is broader than 5ps. From equation (6.3), we observe that the maximum measurable absolute change in refractive index becomes bigger by measuring a thinner sample. We can also measure a bigger absolute change in the refractive index by using a bigger time window, requiring a thicker EO-crystal.

In conclusion, we observe that dispersion in a sample causes different frequencies to move slower/faster, causing broadening of the THz pulse. If said pulse becomes longer than 5ps, we remove information by using a time window of 5ps. We can increase the broadening limit by using either a thinner sample or thicker EO-crystal.

6.1.6 Other sources

This section will describe some errors that have been observed but, so far, been considered too small to warrant any further consideration. Nevertheless, the errors show that there are multiple other considerations that are important to TTDS. We include the errors as bullet points below.

- We observe the reference and sample pulses at different positions on the translation stage. Any misalignment in the delay arm may cause the probe IR intensity to change as a function of translation stage position. Thus the intensity of IR that hits the GaP may change as the translation stage moves, which could create a systematic error in the measurements.

- Typically, a noisy behavior in the lower frequencies of the THz regime will give an error in the calculated phase of the FFT. Appendix E gives a detailed description. The lower frequencies are important in calculating the refractive index and absorption coefficient due to the unwrap function used in the calculation scheme.

- We experienced fluctuations in the laser intensity at an earlier stage of the thesis work, and it should not go unmentioned. These variations relate to the generative process, as a change in IR-pump intensity alters the amount of THz generated inside the highly nonlinear plasma. However, assuming that the fluctuations are Gaussian distributed, it should be averaged by the Lock-in Amplifier. We believe that a 300ms time constant is enough, as it gives a stable value from the Lock-in when sitting on the peak. Here, stable is the same as small fluctuations in the first decimal point of mV. We can further truncate the variations by increasing the time constant.

- If the THz beam hits the sample at a small angle instead of the proposed normal incidence, Fresnels transmission coefficients will change. This change will create an error in the calculated n and κ. Some authors include the angle in the calculations [18], while some do not incorporate it [19]. An error associated angle will change Fresnel's transmission coefficients and the thickness as seen by the THz radiation. Consequently, changing the measured n and κ.

6.2 Status of the setup

In this section, we will review the status of the setup in its present configuration. We base the review on the proposed errors and the Results chapter.

We observe that for materials without significant features in the THz domain like Germanium, Fused Silica, and Silicon, we are capable of determining the refractive index and absorption coefficient very close to the values in the literature. However, complex materials, such as GaP, are harder to measure. The optical parameters can be partly resolved, but are limited by dispersion. For materials that show significant features like KTP, we see that determination of the absorption coefficient is limited by the resolvable α_{max}. Moreover, the dispersion in KTP makes it hard to calculate n and κ using a time window approach, because the pulse is broader than the time window.

In summary, the transmission system is in excellent condition, and we are aware of several issues that have to be considered in order to perform exact measurements. However, materials with high dispersion and absorption give uncertain results, and should therefore be measured in reflection instead

Chapter 7

Conclusion and Further Works

In this thesis, we have built an improved a Terahertz time domain spectroscopy setup. We have addressed several important issues for obtaining an accurate THz measurement, e.g. the size and location of the THz radiation in focus, polarization, scan time, chirp, correlated noise and Fabry-Perot reflections from the GaP crystal. By doing an extensive number of measurements on well-documented samples, we have shown that our setup yield results comparable to those found in the literature.

We have clearly demonstrated how common factors that are part of a conventional THz setup, e.g. humidity, small misalignments, beam spot and behavior around the focal plane, reflections from samples and other optical elements in the setup, and sample quality and thickness all conspire to distort the measured refractive index and absorption coefficients.

Further work would consist of

- Building a system for changing between sample and reference measurements without having to open the box containing the dry air.
- Finding a way of always placing the sample on one side of the focal plane, to negate effects from the Gouy-Phase shift.
- Calibrating the setup such that the THz beam does not move when the sample is placed in.

Also, one should study how to remove the EO-crystal reflections, e.g. by using metal coating. However, as this reduces the spectral bandwidth, one should also consider novel detection schemes. Further considerations could also include new ways of removing the IR-pump after plasma generation, where we now use a spectral splitter. Lastly, it would be interesting to be able to control pump and probe polarizations, as it could increase the efficiency of the setup.

Bibliography

[1] Heraeus hoq 310 fused quartz data sheet.

[2] http://www.thinksrs.com/downloads/PDFs/ApplicationNotes/AboutLIAs.pdf. *About Lock-In Amplifiers*.

[3] Noncovalent intermolecular forces in polycrystalline and amorphous saccharides in the far infrared. *Chemical Physics*, 288(2):261 – 268, 2003.

[4] http://photonicswiki.org/index.php?title=File:FSEOS_of_THz.png. Checked 31.12.2016.

[5] H. Nmec F. Kadlec A. Pashkin, M. Kempa and P. Kuel. Phase-sensitive time-domain terahertz reflection spectroscopy. *REVIEW OF SCIENTIFIC INSTRUMENTS*, 74(11), 2003.

[6] V.D. Antsygin, A.B. Kaplun, A.A. Mamrashev, N.A. Nikolaev, and O.I. Potaturkin. Terahertz optical properties of potassium titanyl phosphate crystals. *Optics Express*, 22(21):25436–25443, 2014. cited By 2.

[7] H. J. Bakker, G. C. Cho, H. Kurz, Q. Wu, and X.-C. Zhang. Distortion of terahertz pulses in electro-optic sampling. *J. Opt. Soc. Am. B*, 15(6):1795–1801, Jun 1998.

[8] Qiang Fu Ping Tan Yongqian Xiong Bang Wu, Lei Cao. Comparison of the detect ion performance of three nonlinear crystals for the el ectro-optic sampling of a felthz source. In *IPAC2014: Proceedings of the 5th International Particle Accelerator Conference*, 2014.

[9] Robert W. Boyd. *Nonlinear Optics, Third Edition*. Academic Press, 3rd edition, 2008.

[10] Paul N. Butcher and David Cotter. *The Elements of Nonlinear Optics*. Cambridge University Press, New York, NY, USA, 1991.

[11] S. Casalbuoni, H. Schlarb, B. Schmidt, P. Schmüser, B. Steffen, and A. Winter. Numerical studies on the electro-optic detection of femtosecond electron bunches. *Phys. Rev. ST Accel. Beams*, 11:072802, Jul 2008.

[12] Yanping Chen, Claude Marceau, Weiwei Liu, Zhen-Dong Sun, Yizhu Zhang, Francis Thberge, Marc Chteauneuf, Jacques Dubois, and See Leang Chin. Elliptically polarized terahertz emission in the forward direction of a femtosecond laser filament in air. *Applied Physics Letters*, 93(23):231116, 2008.

[13] D. J. Cook and R. M. Hochstrasser. Intense terahertz pulses by four-wave rectification in air. *Opt. Lett*, 25(16):1210–1212, 2000.

[14] Jianming Dai, Jiangquan Zhang, Weili Zhang, and D. Grischkowsky. Terahertz time-domain spectroscopy characterization of the far-infrared absorption and index of refraction of high-resistivity, float-zone silicon. *J. Opt. Soc. Am. B*, 21(7):1379–1386, Jul 2004.

[15] P. J. Dean, R. A. Faulkner, S. Kimura, and M. Ilegems. Optical properties of excitons bound to neutral acceptors in gap. *Phys. Rev. B*, 4:1926–1944, Sep 1971.

[16] Jean-Claude Diels and Wolfgang Rudolph. *Ultrashort Laser Pulse Phenomena*. Academic Press, 2nd edition, 2006.

[17] Daniel Dietze, Juraj Darmo, Stefan Roither, Audrius Pugzlys, James N. Heyman, and Karl Unterrainer. Polarization of terahertz radiation from laser generated plasma filaments. *J. Opt. Soc. Am. B*, 26(11):2016–2027, Nov 2009.

[18] Timothy D. Dorney, Richard G. Baraniuk, and Daniel M. Mittleman. Material parameter estimation with terahertz time-domain spectroscopy. *J. Opt. Soc. Am. A*, 18(7):1562–1571, Jul 2001.

[19] L. Duvillaret, F. Garet, and J. L. Coutaz. A reliable method for extraction of material parameters in terahertz time-domain spectroscopy. *IEEE Journal of Selected Topics in Quantum Electronics*, 2(3):739–746, Sep 1996.

[20] Lionel Duvillaret, Frédéric Garet, and Jean-Louis Coutaz. Highly precise determination of optical constants and sample thickness in terahertz time-domain spectroscopy. *Appl. Opt.*, 38(2):409–415, Jan 1999.

[21] D. Grischkowsky, Søren Keiding, Martin van Exter, and Ch. Fattinger. Far-infrared time-domain spectroscopy with terahertz beams of dielectrics and semiconductors. *J. Opt. Soc. Am. B*, 7(10):2006–2015, Oct 1990.

[22] S. Gordon H. Hamster, A. Sullivan and R. W. Falcone. Short-pulse terahertz radiation from high-intensity-laser-produced plasmas. *Phys. Rev. E*, 49(1):671, 1994.

[23] S. Gordon W. White H. Hamster, A. Sullivan and R. Falcone. Subpicosecond, electromagnetic pulses from intense laser-plasma interaction. *Phys. Rev. Lett*, 71(17):2725, 1993.

[24] J. Hebling, A. Stepanov, J. Seres, and J. Kuhl. Time-domain investigation of phonon-polaritons in gap. 249:99–105, 2001.

[25] I-Chen Ho, Xiaoyu Guo, and X.-C. Zhang. Design and performance of reflective terahertz air-biased-coherent-detection for time-domain spectroscopy. *Opt. Express*, 18(3):2872–2883, Feb 2010.

[26] M.V. Hobden and J.P. Russell. The raman spectrum of gallium phosphide. *Physics Letters*, 13:39 – 41, 1964.

[27] Perkin Elmer instruments. `http://cpm.uncc.edu/sites/cpm.uncc.edu/files/media/tn1000.pdf`. *What is a Lock-in Amplifier?*

[28] Peter Uhd Jepsen and Bernd M. Fischer. Dynamic range in terahertz time-domain transmission and reflection spectroscopy. *Opt. Lett.*, 30(1):29–31, Jan 2005.

[29] P.U. Jepsen, D.G. Cooke, and M. Koch. Terahertz spectroscopy and imaging modern techniques and applications [laser photon. rev. 5, no. 124166 (2011)]. *Laser & Photonics Reviews*, 6(3):418–418, 2012.

[30] J. D. Kafka, M. L. Watts, and J.-W. J. Pieterse. Picosecond and femtosecond pulse generation in a regeneratively mode-locked ti:sapphire laser. *IEEE Journal of Quantum Electronics*, 28:2151–2162, oct 1992.

[31] Mayank Kaushik. characterizing and mitigating scattering effects in terahertz time domain spectroscopy measurements, phd thesis. *The University of Adelaide*, 2013.

[32] D. A. Kleinman and W. G. Spitzer. Infrared lattice absorption of gap. *Phys. Rev.*, 118:110–117, Apr 1960.

[33] Markus Kress, Torsten Löffler, Susanne Eden, Mark Thomson, and Hartmut G. Roskos. Terahertz-pulse generation by photoionization of air with laser pulses composed of both fundamental and second-harmonic waves. *Opt. Lett.*, 29(10):1120–1122, May 2004.

[34] R.S. Krishnan and N. Krishnamurthy. The raman spectrum of gallium phosphide. *J. Phys. France*, 26(11):630–633, 1965.

[35] J. Kroll, J. Darmo, and K. Unterrainer. High-performance terahertz electro-optic detector. *Electronics Letters*, 40(12):763–764, June 2004.

[36] Josef Krll, Juraj Darmo, and Karl Unterrainer. Metallic wave-impedance matching layers for broadband terahertz optical systems. *Optics express*, 15(11):65526560, May 2007.

[37] G E Kugel, F Brehat, B Wyncke, M D Fontana, G Marnier, C Carabatos-Nedelec, and J Mangin. The vibrational spectrum of a ktiopo 4 single crystal studied by raman and infrared reflectivity spectroscopy. *Journal of Physics C: Solid State Physics*, 21(32):5565, 1988.

[38] P. Kužel, H. Němec, F. Kadlec, and C. Kadlec. Gouy shift correction for highly accurate refractive index retrieval in time-domain terahertz spectroscopy. *Opt. Express*, 18(15):15338–15348, Jul 2010.

[39] Yun-Shik Lee. *Principles of Terahertz Science and Technology*. Springer, 2009.

[40] Ernest V. Loewenstein, Donald R. Smith, and Robert L. Morgan. Optical constants of far infrared materials. 2: Crystalline solids. *Appl. Opt.*, 12(2):398–406, Feb 1973.

[41] Theresa A. Maldonado and Thomas K. Gaylord. Electrooptic effect calculations: simplified procedure for arbitrary cases. *Appl. Opt.*, 27(24):5051–5066, Dec 1988.

[42] J. Clerk Maxwell. A dynamical theory of the electromagnetic field. *Phil Trans R Soc*, 155:459–512, Jan 1865.

[43] Yasuo Minami, Takayuki Kurihara, Keita Yamaguchi, Makoto Nakajima, and Tohru Suemoto. Longitudinal terahertz wave generation from an air plasma filament induced by a femtosecond laser. *Applied Physics Letters*, 102(15):151106, 2013.

[44] P. Mounaix, L. Sarger, J.P. Caumes, and E. Freysz. Characterization of non-linear potassium crystals in the terahertz frequency domain. *Optics Communications*, 242(4):631 – 639, 2004.

[45] Mira Naftaly and Richard Dudley. Methodologies for determining the dynamic ranges and signal-to-noise ratios of terahertz time-domain spectrometers. *Opt. Lett.*, 34(8):1213–1215, Apr 2009.

[46] T. I. Oh, Y. S. You, and K. Y. Kim. Two-dimensional plasma current and optimized terahertz generation in two-color photoionization. *Opt. Express*, 20(18):19778–19786, Aug 2012.

[47] Tetsuhiko Ohba and Shunichi Ikawa. Farinfrared absorption of silicon crystals. *Journal of Applied Physics*, 64(8):4141–4143, 1988.

[48] D. F. Parsons and P. D. Coleman. Far infrared optical constants of gallium phosphide. *Appl. Opt.*, 10(7):1683–1685, Jul 1971.

[49] A. Perot and C. Fabry. On the application of interference phenomena to the solution of various problems of spectroscopy and metrology. *Astrophysical Journal, vol. 9, p.87*, 9:87, 1899.

[50] David G. Cooke Peter Uhd Jepsen and Martin Koch. Terahertz spectroscopy and imaging modern techniques and applications. *Laser Photonics Rev*, 5:124–166, 2011.

[51] Jason E. Peters, P. Darrell Ownby, Charles R. Poznich, and Jroy C. Richter. Far-infrared absorption of czochralski germanium and silicon. *Proc. SPIE*, 3424:98–105, 1998.

[52] RP Photonics. Chirp. *RP Photonics*, 2017.

[53] Spectra Physics. Solstice, one-box ultrafast amplifier laser, user's manual. *Spectra Physics*, 2008.

[54] Paul C. M. Planken, Han-Kwang Nienhuys, Huib J. Bakker, and Tom Wenckebach. Measurement and calculation of the orientation dependence of terahertz pulse detection in znte. *J. Opt. Soc. Am. B*, 18(3):313–317, Mar 2001.

[55] Rohit P. Prasankumar and Antoinette J . Taylor. *Optical Techniques for Solid-State Materials Characterization*. CRC Press, 1st edition, 2011.

[56] B. Pdr. Zone edge phonons in gallium phosphide. *physica status solidi (b)*, 120(1):207–213, 1983.

[57] Pdr, B. and Izvekov, V.P. Far-infrared lattice absorption in gallium phosphide. *Rev. Phys. Appl. (Paris)*, 18(11):737–739, 1983.

[58] Matthew T. Reiten, Stacee A. Harmon, and Richard Alan Cheville. Terahertz beam propagation measured through three-dimensional amplitude profile determination. *J. Opt. Soc. Am. B*, 20(10):2215–2225, Oct 2003.

[59] B. E. A. Saleh and M. C. Teich. *Fundamentals of Photonics Second Edition*. Wiley Interscience, Hoboken, New Jersey, USA, 2007.

[60] Maik Scheller. Data extraction from terahertz time domain spectroscopy measurements. *Journal of Infrared, Millimeter, and Terahertz Waves*, 35(8):638–648, 2014.

[61] Maik Scheller, Christian Jansen, and Martin Koch. Analyzing sub-100-m samples with transmission terahertz time domain spectroscopy. *Optics Communications*, 282(7):1304 – 1306, 2009.

[62] A.E. Siegman. *Lasers*. University Science Books, 1986.

[63] Trygve Sørgård. terahertz time-domain spectroscopy of thin material sample, master's thesis. *Norwegian University of Science and Technology*, 2015.

[64] Ken Suto and Junichi Nishizawa. Radiative recombination mechanisms in stoichiometrycontrolled gap crystals. *Journal of Applied Physics*, 67(1):459–464, 1990.

[65] L. Ouvrad M. Troost. *Compt. Rend*, 117(121), 1890.

[66] Martin van Exter, Ch. Fattinger, and D. Grischkowsky. Terahertz time-domain spectroscopy of water vapor. *Opt. Lett.*, 14(20):1128–1130, Oct 1989.

[67] Martin van Exter and D. Grischkowsky. Carrier dynamics of electrons and holes in moderately doped silicon. *Phys. Rev. B*, 41:12140–12149, Jun 1990.

[68] A. K. Wan Abdullah, G. A. Gledhill, C. Patel, and T. J. Parker. The far infrared optical constants of gap. *Infrared Physics*, 29:719–723, May 1989.

[69] Andrew M. Weiner. *Ultrafast Optics*. John Wiley & Sons, Inc., 1st edition, 2008.

[70] B.A. Weinstein. Pressure dependent optical phonon anharmonicity in gap. *Solid State Communications*, 20(10):999 – 1003, 1976.

[71] Withawat Withayachumnankul and Mira Naftaly. Fundamentals of measurement in terahertz time-domain spectroscopy. *Journal of Infrared, Millimeter, and Terahertz Waves*, 35(8):610–637, Aug 2014.

[72] C. Wolpert, S. Tani, Y. Kinoshita, T. Tanaka, and K. Tanaka. *Terahertz Response of low-OH Synthetic Silica Glass Probed by a Broadband Plasma Source*. Optical Society of America, 2013.

[73] Q. Wu and X.-C. Zhang. 7 terahertz broadband gap electro-optic sensor. *Applied Physics Letters*, 70(14):1784–1786, 1997.

[74] Xu Xie, Jianming Dai, and X.-C. Zhang. Coherent control of thz wave generation in ambient air. *Phys. Rev. Lett.*, 96:075005, Feb 2006.

[75] A. Yariv. *Optical Electronics in Modern Communications*. Number v. 1 in Oxford series in electrical and computer engineering. Oxford University Press, 1997.

[76] Maksim Zalkovskij. *Terahertz time-domain spectroscopy of chalcogenide glasses and devices for terahertz radiation manipulation*. Ph.D. Thesis. DTU Fotonik, 2013.

[77] N. A. Zharova, V. A. Mironov, and D. A. Fadeev. Anisotropic effects of terahertz emission from laser sparks in air. *Phys. Rev. E*, 82:056409, Nov 2010.

Appendices

Appendix A

Calculating optical parameters for reflection at 45-degree incidence for s-polarized waves

We want to create an analytically solvable equation for the refractive index

$$n(\omega) = \hat{n}(\omega) + i\kappa(\omega), \tag{A.1}$$

using the transfer function

$$H(\omega) = \frac{E_s}{E_r} = |r|e^{i\zeta(\omega)} \tag{A.2}$$

For s-polarized waves , and with a 100% reflecting mirror we can write the transfer function using Fresnel's equation for s-polarized reflection as

$$|r|e^{i\zeta(\omega)} = \frac{r_{sample}}{r_{metal}} = \frac{n_{air}\cos\theta_I - n(\omega)\cos\theta_T}{n_{air}\cos\theta_I + n(\omega)\cos\theta_T} \cdot \frac{1}{-1} \tag{A.3}$$

$$= \frac{n(\omega)\cos\theta_T - n_{air}\cos\theta_I}{n_{air}\cos\theta_I + n(\omega)\cos\theta_T} \tag{A.4}$$

$$= \frac{n(\omega)\cos\theta_T - \frac{1}{\sqrt{2}}}{\frac{1}{\sqrt{2}} + n(\omega)\cos\theta_T}. \tag{A.5}$$

Here we have used that the incidence angle θ_I is 45-degrees and that $n_{air} = 1$, furthermore $r_{metal} = -1$ for a perfect metal. Inverting equation A.5 yields,

$$n(\omega)\cos\theta_T = \frac{1}{\sqrt{2}}\frac{1 + |r|e^{i\zeta(\omega)}}{1 - |r|e^{i\zeta(\omega)}}. \tag{A.6}$$

Multiplication of by the denominators complex conjugate yield

$$n(\omega)\cos\theta_T = \frac{1}{\sqrt{2}}\frac{1-|r|^2+2i|r|\sin(\zeta(\omega))}{1+|r|^2-2|r|\cos(\zeta(\omega))}. \tag{A.7}$$

Using Snell's law we attain a relationship between the real part of the refractive index $\hat{n}(\omega)$ and the transmittance angle θ_T.

$$\arcsin\left(\frac{1}{\sqrt{2}\hat{n}(\omega)}\right) = \theta_T \tag{A.8}$$

Substituting A.8 into the left side of A.7 yields

$$n(\omega)\cos(\arcsin\left(\frac{1}{\sqrt{2}\hat{n}(\omega)}\right)) = n(\omega)\cdot\sqrt{1-\frac{1}{2\hat{n}(\omega)^2}}. \tag{A.9}$$

The last equality yields, as long as $\hat{n}(\omega)$ is bigger than $\frac{1}{\sqrt{2}}$. In other words, looking back at Snell's law the angle of transmittance is perpendicular to the normal, and we have total reflection. Thus it seems like this experiment is fundamentally limited by it's ambient material. It would be possible to change the angle of incidence as a thought experiment to around 22.5-degrees (w.r.t. surface normal) . In this scenario our limitation changes to $\hat{n}(\omega) > 0.38268$. This indicates that the smallest real part of the refractive index possible to calculate with this method, is limited by the angle of incidence and the ambient material around the sample. Now we rewrite A.7 by replacing $n(\omega)$ with it's real and imaginary part,

$$(\hat{n}(\omega)+i\kappa(\omega))\sqrt{(1-\frac{1}{2\hat{n}(\omega))^2}}) = \frac{1}{\sqrt{2}}\frac{1-|r|^2+2i|r|\sin(\zeta(\omega))}{1+|r|^2-2|r|\cos(\zeta(\omega))}. \tag{A.10}$$

Taking the real and imaginary part of A.10

$$\hat{n}(\omega) = \frac{1}{2}\frac{(1-|r|^2)^2}{(1+|r|^2-2|r|\cos(\zeta(\omega)))^2}+\frac{1}{2} \tag{A.11}$$

$$\kappa(\omega) = \frac{1}{\sqrt{2}}\frac{2|r|\sin(\zeta(\omega))}{1+|r|^2-2|r|\cos(\zeta(\omega))}\frac{1}{\sqrt{(1-\frac{1}{2\hat{n}(\omega))^2})}} \tag{A.12}$$

Appendix B

Calculations of optical parameters for transmission with complex fresnels coefficents

We want to derive equations that can be used to extract $\hat{n}$ and κ,

$$n(\omega) = \hat{n}(\omega) + i\kappa(\omega), \tag{B.1}$$

for transmission TTDS measurements with a sample that has complex fresnels coefficents ($t_i \in \mathbb{C}$). Starting with the transfer function

$$H(\omega) = \frac{E_s}{E_r} = T(\omega)e^{i\phi(\omega)} = t_1 e^{-\frac{\omega}{c}\kappa(\omega)d} e^{j\frac{\omega}{c}(\hat{n}(\omega)-1)d} t_2 \tag{B.2}$$

Assuming that the propagation of electric radiation is perpendicular to the sample surface, t_1 and t_2 is given by Fresnel's equations and simplified by Snell's law to

$$t_1 = \frac{2}{1 + (\hat{n}(\omega) + i\kappa(\omega))} \tag{B.3}$$

$$t_2 = \frac{2(\hat{n}(\omega) + i\kappa(\omega))}{1 + (\hat{n}(\omega) + i\kappa(\omega))}. \tag{B.4}$$

Rewriting t_i to exponential form yields,

$$t_1 = |t_1|e^{\phi_1(\omega)} = \sqrt{\frac{4}{(1+\hat{n}(\omega))^2 + \kappa(\omega)^2}} e^{j\arctan(\frac{-\kappa(\omega)}{1+\hat{n}(\omega)})} \tag{B.5}$$

$$t_2 = |t_2|e^{\phi_2(\omega)} = \sqrt{\frac{4(\hat{n}(\omega)^2 + \kappa(\omega)^2)}{(1+\hat{n}(\omega))^2 + \kappa(\omega)^2}} e^{j\arctan(\frac{\kappa(\omega)}{\kappa(\omega)^2 + \hat{n}(\omega) + \hat{n}(\omega)^2})} \tag{B.6}$$

Substituting equations B.5 and B.6 into equation B.2 we arrive at

$$T(\omega)e^{i\phi(\omega)} = |t_1|e^{j\phi_1(\omega)}e^{-\frac{\omega}{c}\kappa(\omega)d}e^{j\frac{\omega}{c}(\hat{n}(\omega)-1)d}|t_2|e^{j\phi_2(\omega)}. \tag{B.7}$$

Relating the measurable $T(\omega)$ and $\phi(\omega)$ with the real and imaginary part of equation B.7 yields,

$$T(\omega) = \frac{4}{(\hat{n}(\omega)+1)^2+\kappa(\omega)^2}\sqrt{\hat{n}(\omega)^2+\kappa(\omega)^2}e^{-\frac{\omega}{c}\kappa(\omega)d} \tag{B.8}$$

$$\phi(\omega) = \arctan(\frac{-\kappa(\omega)}{1+\hat{n}(\omega)}) + \frac{\omega}{c}(\hat{n}(\omega)-1)d + \arctan(\frac{\kappa(\omega)}{\kappa(\omega)^2+\hat{n}(\omega)+\hat{n}(\omega)^2}). \tag{B.9}$$

These are transcendental equations, and can not be solved analytically, thus numerical iterative processes are necessary to extract the complex refractive index n.

Appendix C

Numerical extraction of optical parameters

In this section we introduce a core procedure for extracting optical parameters in TTDS. This methodology was first introduced by Duivalleret et. al. [19, 20] in 1996. The principle is to minimize the error between a measured transfer function, $H(\omega)$ and it's analytic side part $\hat{H}(\omega)$. The analytical transfer function will vary with different effects, for example one might see both complex fresnel's coefficents and Fabry-Perot effects in the same sample. These effects can be included into the analytic part, and can thus be accounted for in the final resulting extraction of the complex valued refractive index n. Note that in principle this method can be used for both reflection and transmission.

By comparing two transfer functions and dividing the transfer function $H(\omega)$ into two parts, a magnitude and phase, $|H(\omega)|$ and $e^{i\phi(\omega)}$, respectively. We attain,

$$\phi_{error}(\omega) = \phi(\omega) - \hat{\phi}(\omega) \tag{C.1}$$

$$H_{error}(\omega) = |H(\omega)| - |\hat{H}(\omega)|. \tag{C.2}$$

The total error for any given frequency can then be formalized by

$$Error(\omega) = |H_{error}(\omega)| + |\phi_{error}(\omega)|. \tag{C.3}$$

The analytic transfer function $\hat{H}(\omega)$ is a function of $\hat{n}$ and κ. As there are several possible extraction algorithms, the methodology from paper to paper varies from this point on. The most common approach is to use a known numerical method, i.e. fixed point iteration, Nelder-Mead or Gradient Descent, to solve for n and κ for each frequency. In addition a common denominator is to choose the initial values of n and κ based on the simple extraction of optically thick samples with small absorption, i.e. disregarding whether the sample is absorptive or thin for the initial guess for n and κ.

Appendix D

Material properties

In this appendix we give material properties measured from other experiments.

D.1 Germanium

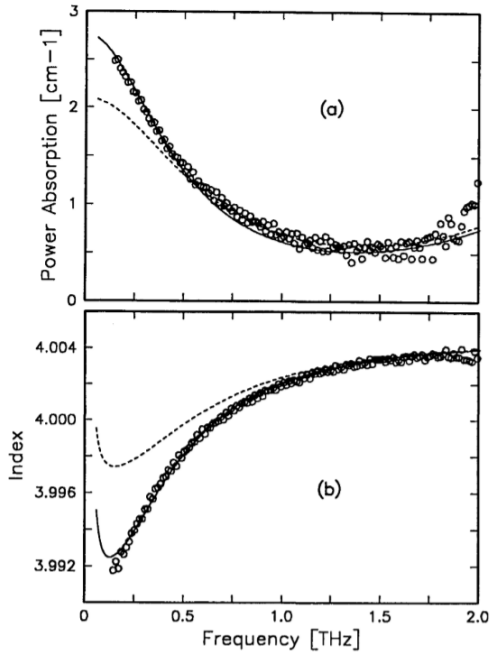

Figure D.1: Refractive index and absorption coefficient of Germanium from 0 to 2 THz, from [21]

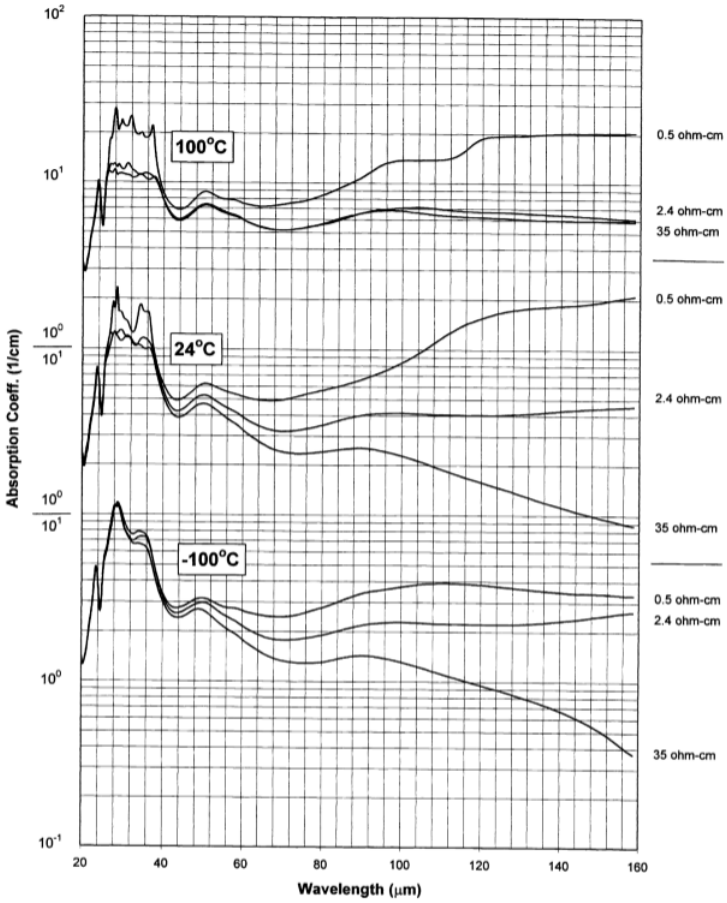

Figure 2 - Absorption coeff. vs. Resistivity and temperature for single crystal germanium at -100, 24, and 100°C for resistivites of 0.5, 2.4, and 35 ohm-cm.

Figure D.2: Absorption coefficient of Czochralski grown Germanium from 0.6 to 5.4 THz at different temperatures from [51]

D.2 Fused Silica

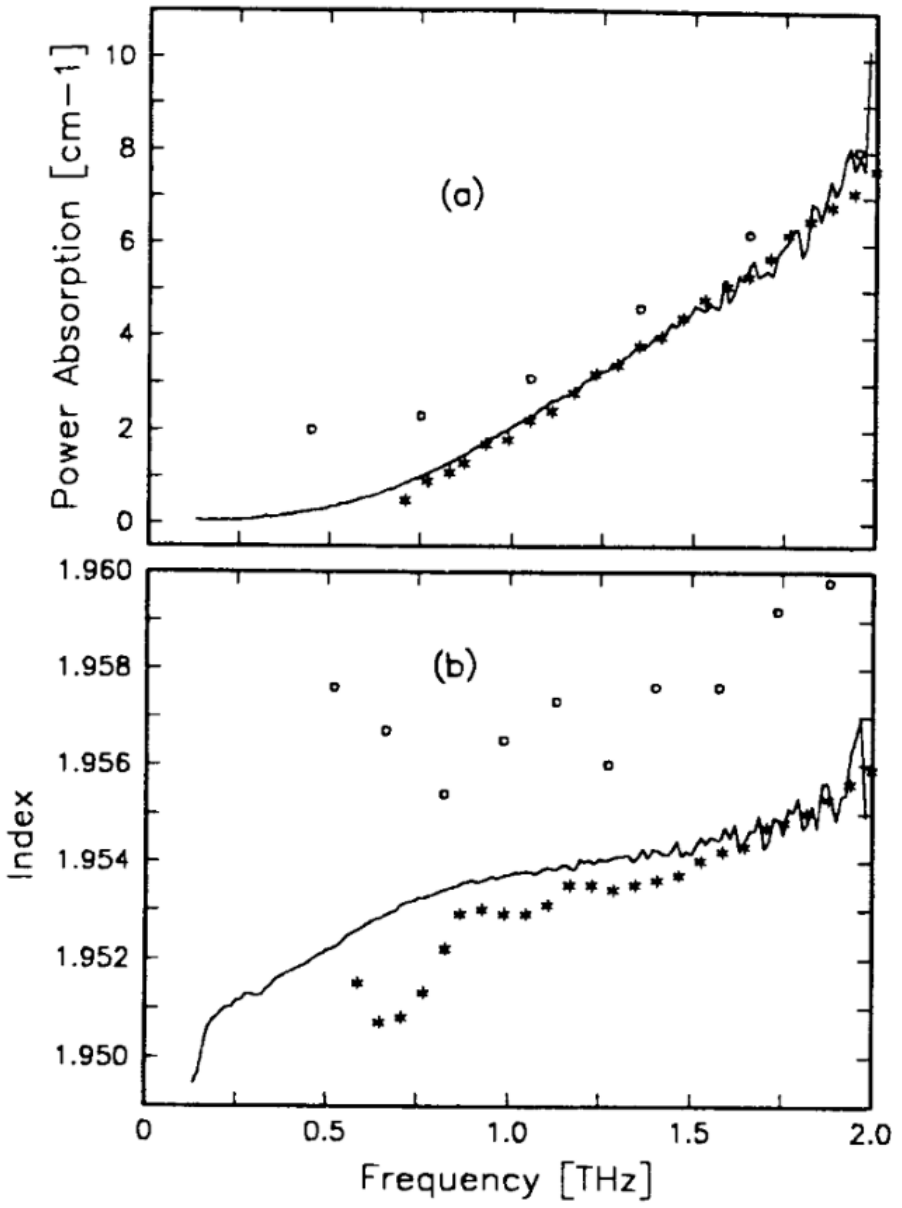

Figure D.3: Refractive index and absorption coefficient of Fused Silica from 0 to 2 THz, from [21]

D.3 Silicon

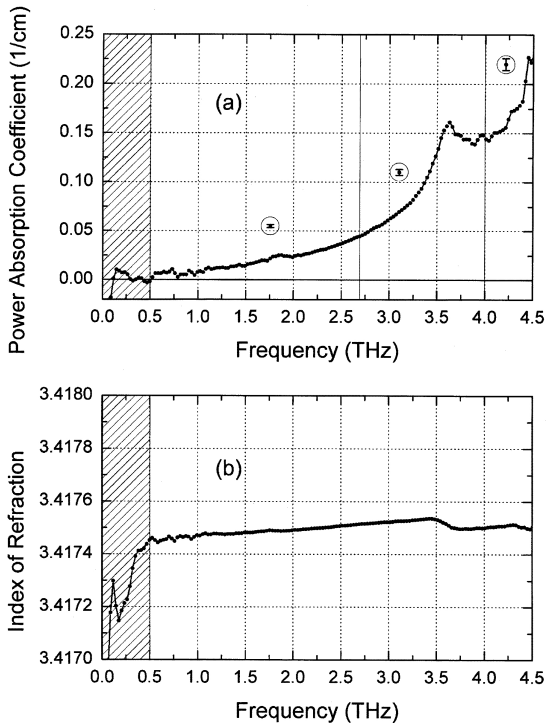

Figure D.4: Refractive index and absorption coefficient of Silicon, from [14]

D.4 GaP

Table 2
Two-phonon processes in gallium phosphide (energies at ≈ 300 K unless noted otherwise)

t / branch*)	calculated (cm^{-1})	Raman [4] (cm^{-1})	Raman [3] (cm^{-1})	Raman [5] (cm^{-1})	Raman [11] (cm^{-1})	IR [21] (cm^{-1})	IR [12, 1 (cm^{-1})
$A_{II} - A_I$	30	31	(30)	30.7			31
$A_I - TA$	50	(47)		46			38
$A_{III} - A_{II}$	60			55			62
$A_{III} - A_I$	90		(97)	93			
TO − LA	104	(105)	104				106
LA − TA	129	(131)		131			
TO − LA	140	136					
LA − TA	144.5	(149)	147	147	148		
$O_I - A_{III}$	148		(153)		154		
$O_{III} - A_{III}$	157				160		
LO − LA	160						
2 TA	172	168	166	166	172		
		177				179**)	
		(181)	182	182			
$TO - A_I$	196	(197)	196	197	195		
2 TA	209	208	210	210	208	209**)	210
$O_I - A_{II}$	208						
$O_{III} - A_{II}$	217						220
$O_{II} - A_I$	221						
$O_I - A_I$	238				238		238
$2 A_I$	244	241		244	243		245
$O_{III} - A_I$	247						250
TO − TA	248.5						
LO − TA	265.5	258	257	257		255**)	258
TO − TA	269	264		268			

Figure D.5: Phonon modes of GaP, from [56]

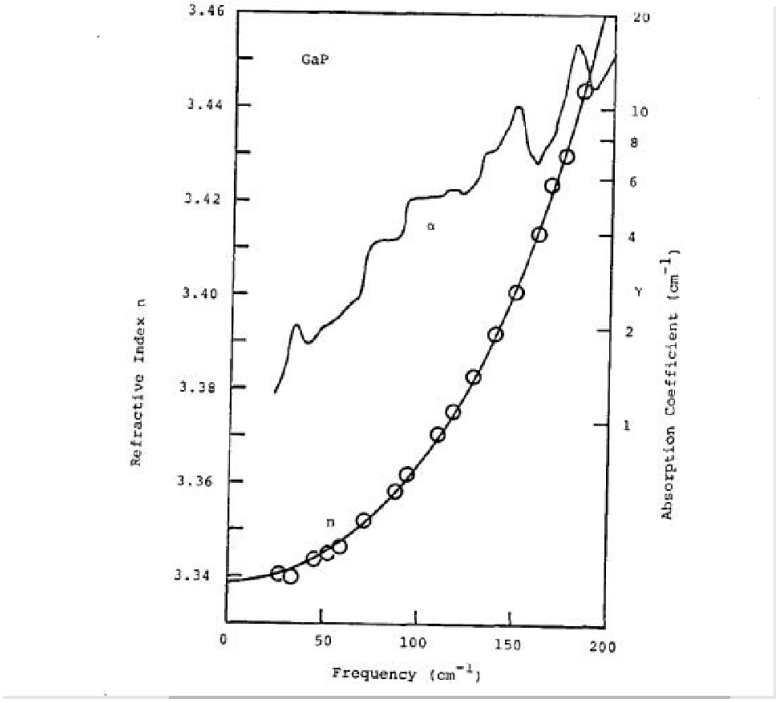

Figure D.6: n (line trough circles) and α for GaP, from 0THz trough $5,5$THz. The refractive index is extrapolated from experimental data points. Figure from [48]

D.5 $KTiOPO_4$ (KTP)

$KTiOPO_4$ (KTP) was first synthesised in 1890 [65]. KTP is known for its large nonlinear coefficient, which have led it to be a natural choice for various nonlinear processes. In addition to the big nonlinear susceptibility, KTP has a large optical and mechanical damage threshold plus a wide transparency range and a large birefringence. The aforementioned birefringence is large enough to make KTP suitable for Birefringent phase matching (BPM), and since KTP is a ferreoelectric material, it can also be used for Quasi-phase matching (QPM).

Today KTP also refers to the isomorphs of KTP, the KTP family. This is a family of crystals which are denoted by $MTiOXO_4$, where M represents either K, Rb, Tl or NH_4 and X is either P or As. The most commonly used in nonlinear optics together with the original KTP are $RbTiOPO_4$ (RTP), $KTiOAsO_4$ (KTA) and $RbTiOAsO_4$ (RTA).

KTP and RTP are both orthorombic and belong to the acentric $mm2$ symmetry group. They belong to the space group $Pna2_1$, such that the crystal axes a, b, c correspond to the optical axes x, y, z, where c is the polar axis.

	Infrared results				Raman results	
Interval	ω_{TO} (cm^{-1})	ω_{LO} (cm^{-1})	γ (cm^{-1})	$\Delta\varepsilon$	Measured frequency (cm^{-1})	Intensity (%)
I	78.5	78.7	2.5	0.1	88 sh	1.3
	91	94.2	1.7	1.5	91 w	
	95	96.5	2	0.1	95 sh	
	111	111.2	3	0.06	114 db	
	117.5	117.7	2	0.06	116 db	
	122.5	123.3	1	0.2	121 w	
	129.5	129.6	2	0.03		
	134	135.8	1.5	0.37	132 wb	
II	145	145.5	7	0.1		16.7
	154	154.8	4	0.14	153 m	
	167	167.4	4	0.07	172 m	
	178.7	179.4	6	0.11	178 sh	
	203.7	204.6	3.5	0.2	202 m	
	213	219.2	2	0.4	213 s	
					221 m	
					231 wsh	
	235	237.6	7	0.5	237 wsh	
III	260	261	2.7	0.45		11.6
	268	284.5	4.5	2.5	268 vs	
					275 s	
	288	293.2	10	0.2	289 m	
IV	311	322.5	7	1.4	314 m	8.5
	326	356.4	7	0.4	323 m	
					340 s	
					349 wsh	

Figure D.7: Phonon modes in KTP. From [37]

Appendix E

Unwrapping and Extrapolation of phase and the impact on n and κ

This section is all about the phase $\phi(\omega)$ term in the following equation

$$H(\omega) = \frac{E_s(\omega)}{E_r(\omega)} = T(\omega)e^{i\phi(\omega)}. \tag{E.1}$$

ϕ is describing the ratio between the complex and real part of the transfer function trough an angle in complex space. Using the phase term directly in calculations of n and κ gives discontinuities phase jumps due to the phase jumping from $-\pi$ to π or vice versa. To prevent this, one use unwrapping which makes the phase term continuous. Unwrapping is done by adding/subtracting 2π as the phase is 2π shifted each jump.

However, this may impose a $2\pi n$ bias in the phase throughout the whole spectrum. Specially in the lower frequencies as there are more uncertainty in the measurement due to lower spectral amplitude. A discussion on this can also be found in [71].

Some authors argue that using a linear extrapolation from the middle frequencies, where the phase is set to zero at $\omega = 0$ is a good solution. This solution is used by some authors and is discussed in detail in [19]. In this thesis we do not use any extrapolation. However, for the readers appreciation we have included two figures that show how this impacts n and κ for a particular measurement in this setup.

We extrapolated the measurement by using the phase between $0,09$ to 4.5THz. Then we use the extrapolated values for frequencies below 0.09THz.

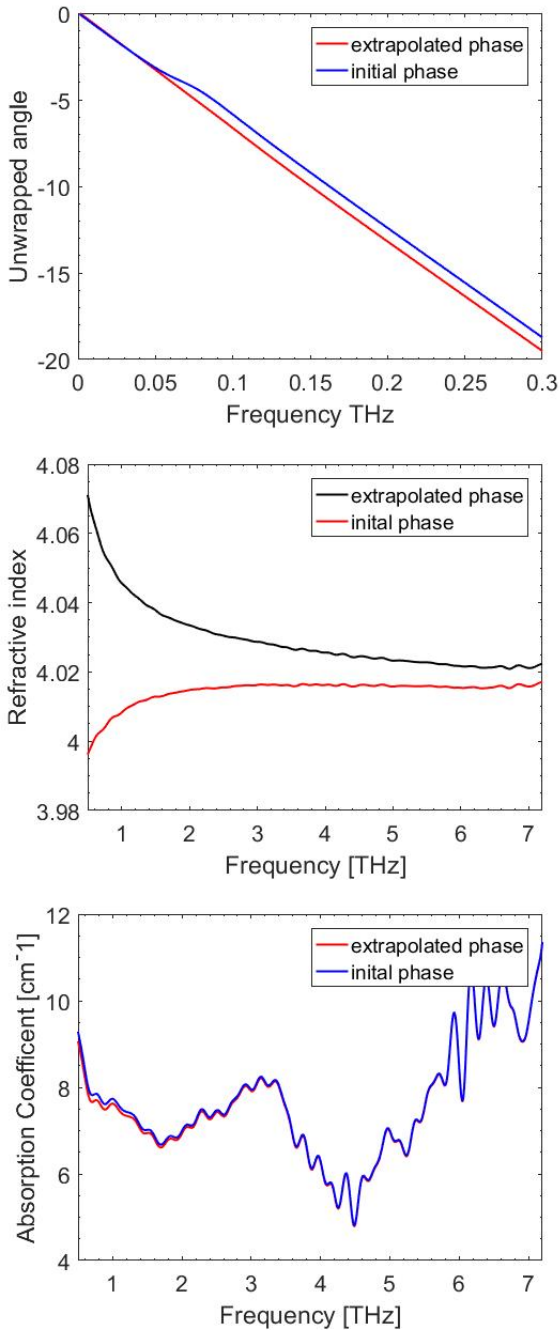

Figure E.1: (TOP) Extrapolated phase and initial phase (MID) n for both cases (BOT) Absorption coefficient for both cases.

Appendix F

Additional Theory

F.1 Polarization of Electric fields

We now consider a monochromatic plane wave with angular frequency $\omega = 2\pi f$ propagating in the z-direction with wavevector $\vec{k}$. The electric field will lie in the x-y plane and can be described as

$$E(z,t) = \Re[\vec{A}e^{i(kz-\omega t)}] \tag{F.1}$$

where $\vec{A}$ is the complex envelope of the wave. We can describe the polarization of the wave using

$$\vec{A} = A_x\hat{x} + A_y\hat{y}. \tag{F.2}$$

Now we express the complex components A_x and A_y with their magnitudes and phases $a_x e^{j\phi_x x}$ and $a_y e^{j\phi_y y}$, respectively. In addition we break the field into two parts, yielding

$$E_x = a_x \cos(\omega t - kz + \phi_x) \tag{F.3}$$
$$E_y = a_y \cos(\omega t - kz + \phi_y). \tag{F.4}$$

Here a_x and a_y are by definition real valued parameters. These are parametric equations for an ellipse, so we can write the polarization of the electric field as

$$\frac{E_x^2}{a_x^2} + \frac{E_y^2}{a_y^2} - 2\cos(\phi_y - \phi_x)\frac{E_x E_y}{a_x a_y} = \sin^2(\phi_y - \phi_x). \tag{F.5}$$

The electric field rotates in the xy-plane when it propagates in time and z-direction, repeating itself for every wavelength $\lambda = \frac{c}{f}$. For certain values of $\phi = \phi_y - \phi_x$ the electrical field will become linear or circular. More precisely the polarization becomes linear for $\phi = \pi n$, $n \in Z$ and circular for $\frac{E_x^2}{a_x^2} = \frac{E_y^2}{a_y^2}$ and $\phi = \frac{\pi}{2} + \pi n$, $n \in Z$. There are also novel but equal representations of the polarization of an optical field, namely the Poincare sphere and the Stokes vector. [59]

F.1.1 Jones Calculus

By using $A_x = a_x e^{j\phi_x x}$ and $A_y = a_y e^{j\phi_y y}$ we can describe a monochromatic plane wave travelling in the z direction on vector form, this vector is known as the Jones vector,

$$\vec{J} = \begin{bmatrix} A_x \\ A_y \end{bmatrix}. \tag{F.6}$$

From $\vec{J}$ it is possible to determine the value of the intensity

$$I = \frac{\mid A_x \mid^2 + \mid A_y \mid^2}{2\eta}, \tag{F.7}$$

and the orientation of the polarization ellipse by using the ratio $\frac{a_y}{a_x} = \frac{A_y}{A_x}$ and the phase difference ϕ.
One can now consider an arbitrary polarized optical plane wave propagating through an optical system. Here it is assumed that the system is linear and that the plane wave nature is conserved. As a result of linearity one can superposition the optical fields propagating through the system. As before we can describe our initial wave with a Jones vector $\begin{bmatrix} A_{1x} \\ A_{1y} \end{bmatrix}$. Then the output wave is generally related by weighted positions

$$A_{2x} = T_{11}A_{1x} + T_{12}A_{1y} \tag{F.8}$$
$$A_{2y} = T_{21}A_{1x} + T_{22}A_{1y}. \tag{F.9}$$

Here we have T_{ij} , which are constants describing the properties of the system. Rewriting this system in terms of a $2x2$ matrix with T_{ij} as elements we obtain

$$\begin{bmatrix} A_{2x} \\ A_{2y} \end{bmatrix} = \begin{bmatrix} T_{11}T_{12} \\ T_{21}T_{22} \end{bmatrix} \begin{bmatrix} A_{1x} \\ A_{1y} \end{bmatrix}. \tag{F.10}$$

F.2 Fresnels equation and Fabry-Perot Etalon

Starting with Maxwell's equation (equation 2.1 - 2.4) one can show that the boundary conditions in a boundary between two different media can be written as,

$$E_1^{\parallel} = E_2^{\parallel} \tag{F.11}$$
$$\epsilon_1 E_1^{\perp} = \epsilon_2 E_2^{\perp} \tag{F.12}$$
$$\frac{1}{\mu_1} B^{\parallel}{}_1 = \frac{1}{\mu_2} B_2^{\parallel} \tag{F.13}$$
$$B_1^{\perp} = B_2^{\perp}. \tag{F.14}$$

Here subscripts 1 and 2 refer to the different sides of a boundary, $\perp$ and $\parallel$ refer to the perpendicular and the parallel component of the field with respect to the orientation of the interface, respectively. In the study of plane wave, we define s-polarization and p-polarization for waves which have electric field perpendicular or parallel to the plane of

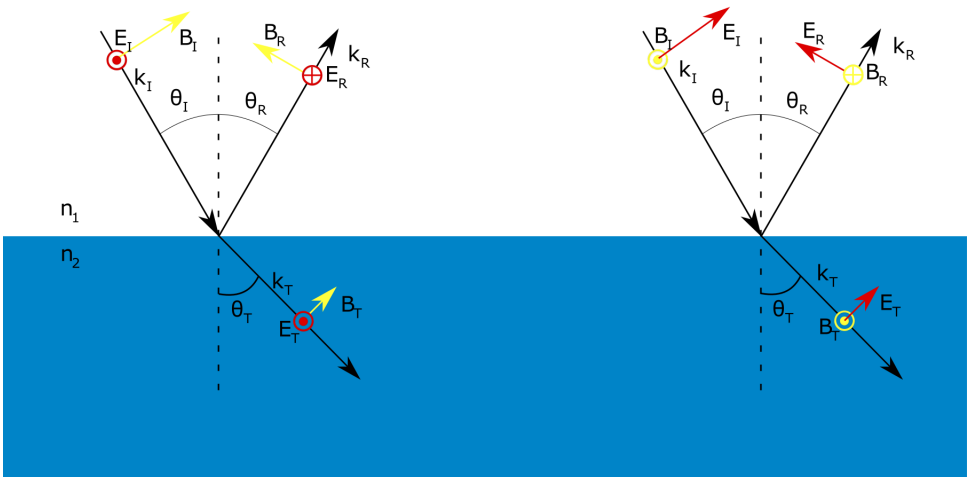

Figure F.1: The reflection and transmission, seen from the plane of incidence, between an interface of two materials with refractive index n_1 and n_2, for a p-polarized wave (left) and a s-polarized wave (right). The yellow vectors represent the magnetic field $\vec{B}$ and the red vectors represent the Electric field $\vec{E}$. The black arrows are the propagation vector $\vec{k}$

incident, respectively. The plane of incident is the plane including the surface normal and the wave-vector $\vec{k}$.

The subscripts I, R, T in Figure F.1 stands for incident,reflected and transmitted, respectively. The angles between the propagation vector and the surface normal are θ_I,θ_R and θ_T for incident,reflected and transmitted waves respectively. The relation between these angles can be expressed as

$$\theta_I = \theta_R \tag{F.15}$$

$$n_1 \sin\theta_I = n_2 \sin\theta_T, \tag{F.16}$$

where equation F.16 is known as Snell's law. Henceforth the boundary conditions for electromagnetic waves can be expressed as ratios between the transmitted or reflected electromagnetic wave amplitude to that of the incident wave. These are well known in optics, and are named Fresnel's equations, and is written as

$$r_s = \frac{E_{s,R}}{E_{s,I}} = \frac{n_1\cos\theta_I - n_2\cos\theta_T}{n_1\cos\theta_I + n_2\cos\theta_T} \tag{F.17}$$

$$t_s = \frac{E_{s,T}}{E_{s,I}} = \frac{2n_1\cos\theta_I}{n_1\cos\theta_I + n_2\cos\theta_T} \tag{F.18}$$

$$r_p = \frac{E_{p,R}}{E_{p,I}} = \frac{n_2\cos\theta_I - n_1\cos\theta_T}{n_2\cos\theta_I + n_1\cos\theta_T} \tag{F.19}$$

$$t_p = \frac{E_{p,T}}{E_{p,I}} = \frac{2n_1\cos\theta_I}{n_2\cos\theta_I + n_1\cos\theta_T}. \tag{F.20}$$

Followingly we define the transmitted and reflected power as,

$$T = \frac{n_2}{n_1} \mid t \mid^2 \tag{F.21}$$

$$R = \mid r \mid^2 . \tag{F.22}$$

F.2.1 Fabry-Perot Etalon

Based on the discussions about Fresnel's equations we see that when an electromagnetic wave is incident on a material, some of it is transmitted and some of it is reflected, this is of course true for both ends of the material. Hence the electromagnetic wave will be reflected back and forth inside the material, inducing what is known as a Fabry-Perot etalon [49]. The principle is shown in Figure F.2,here we see multiple reflections and refractions of the wave as it propagates through the material.

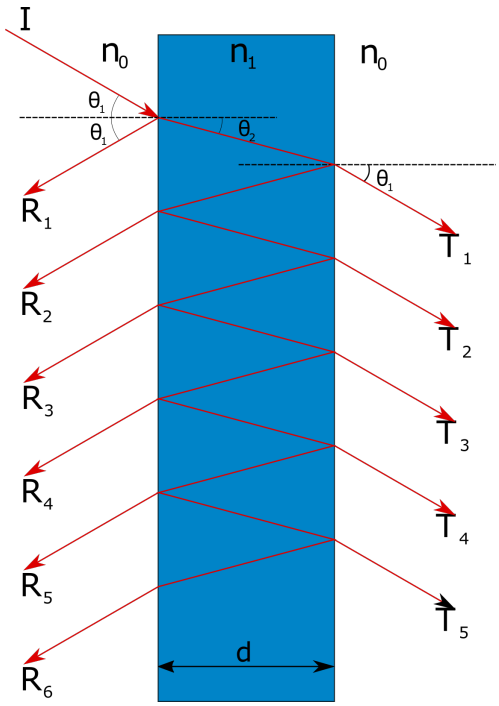

Figure F.2: Fabry-Perot Etalon, Incident beam I is refracted and reflected at the first interface, then the refracted beam is again reflected and refracted at the other end of the medium. From Snell's law we see the angle of the incident wave θ_1 w.r.t. surface normal is the same as the angle of the transmitted wave. This cycle of reflection/refraction repeats itself as shown in the figure.

Using a sum over all possible paths from A to B, or from A to A we achieve the

transmitted and reflected wave. From the figure we can write,

$$T_{total} = \sum_{n=1}^{\infty} T_n \tag{F.23}$$

$$R_{total} = \sum_{n=1}^{\infty} R_n. \tag{F.24}$$

Of course, these are related to the transmitted and reflected power, but keep in mind that equations (F.21) and (F.22), are for a single refraction/reflection. For the sake of argument we will now consider n_1 as a complex number, i.e. we have absorption in our material. We can then write the propagation of our wave through the medium as

$$\mathcal{E}(\omega, r) = I(\omega) e^{-i\frac{n_1 \omega r}{c}}, \tag{F.25}$$

where l is the distance it travels through the medium, and $I(\omega)$ is the amplitude of the incident wave. By Fresnel's equation (equations F.17 to F.20) we can relate each reflection and refraction incidents by t_{01}, r_{01} and t_{10} , r_{10} for incidence from n_0 to n_1 and conversely, respectively. We can then rewrite T_{total} (equation (F.23)) as

$$T_{total} = t_{01} I(\omega) e^{-i\frac{n_1 \omega l}{c}} t_{10} \sum_{n=0}^{\infty} (r_{10} e^{-i\frac{n_1 \omega l}{c}})^{2n}. \tag{F.26}$$

$$T_{total} = t_{01} I(\omega) e^{-i\frac{n_1 \omega l}{c}} t_{10} \frac{1}{1 - (r_{10} e^{-i\frac{n_1 \omega l}{c}})^2}, \tag{F.27}$$

where $l = \frac{d}{\cos\theta_2}$. Likewise we can write for the reflection power,

$$R_{total} = I(\omega)[\frac{t_{01} t_{10} r_{10} e^{-i\frac{n_1 \omega 2l}{c}}}{1 + (r_{10} e^{-i\frac{n_1 \omega l}{c}})^2} + r_{01}] \tag{F.28}$$

Something to note is that if one alter the thickness of the sample one can achieve resonant transmission, where the waves which are refracted by the first incidence will completely pass through. This happens for $e^{-i\frac{n_1 \omega l}{c}} = 1$, i.e. $l = \frac{\lambda n}{2}$ where $n \in \mathbf{Z}$.

F.3 Gaussian Beam propagation

Gaussian beams are named after its intensity profile, which can be written as

$$I(r, z) = \frac{P}{\pi w(z)/2} e^{-2\frac{r^2}{w(z)^2}}. \tag{F.29}$$

Where P is the power of the beam, $w(z)$ is the beam radius and r is the radial distance from the center axis of the beam. The beam radius $w(z)$ is defined as the distance from the beam axis where the intensity drops to $\frac{1}{e^2}$ or around $13,5\%$. For a monochromatic wave, propagating in z-direction with angular frequency ω we can write the electric field as

$$E(r, z) = E_0 \frac{W_0}{w(z)} e^{-\frac{r^2}{w(z)^2}} e^{-i(kz - \arctan(\frac{z}{z_r}) + \frac{kr^2}{2R(z)})}. \tag{F.30}$$

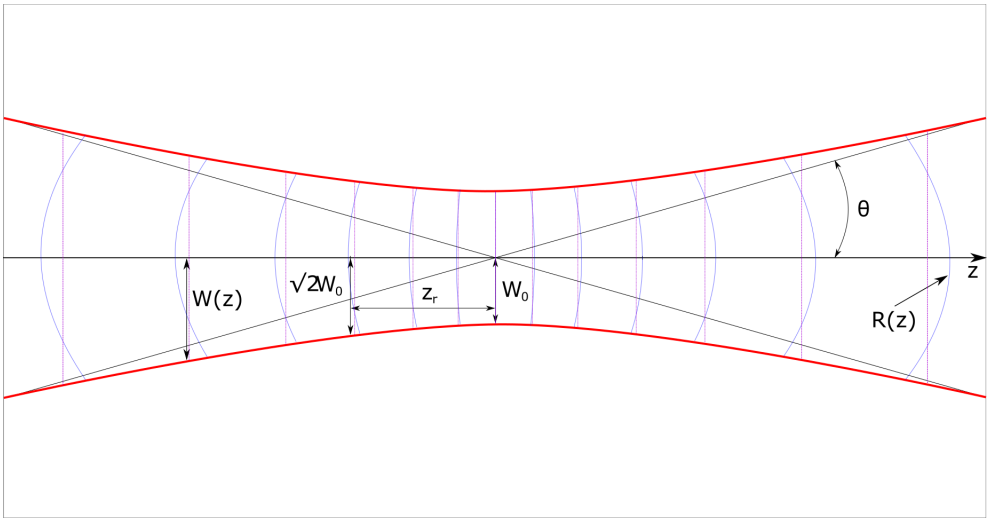

Figure F.3: Gaussian beam with wave fronts in blue. The curvature $R(z)$ decrease closer to the focus, conversely it increases further away. The beam radius $w(z)$ is equal to $\sqrt{2}W_0$ at the Rayleigh length. The purple dotted line represent wave fronts which have an integer number wavelength between each wavefront (plane wave), the relative shift between the Gaussian wavefront and the purple wave fronts represent the Gouy Shift.

Here E_0 is the peak amplitude, W_0 the beam radius at the beam waist, the wavenumber $k = \frac{\omega n}{c}$. The Rayleigh length

$$z_r = \frac{W_0^2 \omega}{2c}, \tag{F.31}$$

is the length for which the beam can propagate without diverging notably, the confocal length is $2z_r$. Furthermore the beam radius will vary along the propagation axis as

$$w(z) = W_0 \sqrt{1 + (\frac{z}{z_r})^2}. \tag{F.32}$$

Beams with relatively steady beam radius are called collimated beams, and these beams will have a large Rayleigh length compared with the propagation length of interest.

At $z = 0$ in Figure F.3 we are at the beam waist (in focus), here the beam radius is at its minimum. As we move away from the focus we see that the curvature R of the wavefronts evolve as

$$R(z) = z(1 + (\frac{z_r}{z})^2). \tag{F.33}$$

The term including $\arctan$ in equation (F.30) describes the Gouy phase shift, this arises as a term since the phase shift of a Gaussian beam is not the same as for a plane wave. By viewing the Gaussian beam as a superposition of plane waves with different propagation directions, we can show that the wave components propagating in directions different from the beam axis will experience smaller phase shifts in $z - direction$. The Gouy phase shift arises from the superposition of all of these components. As seen in Figure F.3 the Gouy

shift can be viewed as a increase in distance between each successive wavefront. Notably when propagation happen from one far field to another we have a total phase shift of

$$\arctan(\frac{z}{z_r}) - \arctan(\frac{-z}{z_r}) = 2\arctan(\frac{z}{z_r}) = \pi. \tag{F.34}$$

Here we have used that the Gouy phase shift changes sign as the wavefront intersect the focus point and $z \gg z_r$.

The beam divergence in the far field ($z \gg z_r$) is

$$\theta = \frac{c}{n\omega\pi W_0}, \tag{F.35}$$

that shows that the divergence of the beam far from the waist is inversely proportional to the refractive index n and the angular frequency ω.